Analysis of and learnings from the first four years of in-situ strain data in Zeerijp-3A

Shell and NAM BV

Pepijn Kole, Matt Cannon, Jelena Tomic, Stijn Bierman

General Introduction

Reservoir compaction is an important factor for subsidence and has therefore been studied since production from the Groningen field commenced. Most compaction monitoring relies on (indirect) measurements of subsidence through optical levelling surveys, GPS and/or InSAR. Compaction is then derived either through direct inversion or through compaction models calibrated to these subsidence measurements and compaction measurements on core samples.

In Groningen also in-situ measurements of compaction in the reservoir have been taken by logging the relative movement of gamma-ray markers placed in monitoring wells since 1982 (Ref. 1 and 2). In 2015 a fibre-optic cable was installed in well ZRP-3. This allows real-time continuous in-situ monitoring of compaction (Ref. 3).

As reservoir compaction is also important input into the seismological model, the studies into seismicity in the Groningen gas field have led to an intensified interest in compaction. In 2015, the existing methods as well as a newly developed method to analyse in-situ measurements of compaction in the monitoring wells were reviewed in detail (Ref. 1). This was followed by a more detailed review (Ref. 2) the in-situ compaction data via gamma ray marker surveys carried out since 2015. The review focussed on the uncertainties in the compaction measurements and whether it is sufficiently accurate to monitor reservoir compaction at the desired depth and time scales.

Compaction can also be measured with the new technology of fibre-optic cables. A glass-fibre cable was installed over the reservoir section of the Zeerijp-3 monitoring well. A year after taking this in-situ compaction measurement system into operation a report describing the first year of experience with this new technology was published (Ref. 3). The current report builds on this and describes the experience in the first four years of operation.

An almost continuous compaction data set has been acquired in the Zeerijp-3A well. In this report the data set is discussed with attention for a number of significant events taking place in these four year, a coiled tubing clean out (CTCO) of the monitoring well, an earthquake of magnitude 3.4 occurring less than 1.5km from the well, an upgrade of DSS interrogator module, and multiple periods of active geophone operation. This report supports the development of a surveillance plan for the Groningen field.

Reference

1. In-situ compaction measurements using gamma ray markers, NAM, Pepijn Kole, June 2015
2. Review of wireline depth precision and accuracy for the application of compaction monitoring, Pepijn Kole, NAM, Aug 2019.
3. The First Year of Distributed Strain Sensing (DSS) - Monitoring in the Groningen Gas Field, Shell and NAM BV, M. Cannon and P. Kole, June 2018.

Title	Analysis of and learnings from the first four years of in-situ strain data in Zeerijp-3A	Date	February 2020
		Initiator	NAM
Autor(s)	Pepijn Kole, Matt Cannon, Jelena Tomic, Stijn Bierman	Editors	Jan van Elk
			Dirk Doornhof
Organisation	NAM	Organisation	NAM
Place in the Study and Data Acquisition Plan	Study Theme: Reservoir Compaction Comment: Reservoir compaction is an important factor for subsidence and has therefore been studied since production from the Groningen field commenced. Most compaction monitoring relies on (indirect) measurements of subsidence through optical levelling surveys, GPS and/or InSAR. Compaction is then derived either through direct inversion or through compaction models calibrated to these subsidence measurements and compaction measurements on core samples. In Groningen also in-situ measurements of compaction in the reservoir have been taken by logging the relative movement of gamma-ray markers placed in monitoring wells since 1982. In 2015 a fibre-optic cable was installed in well ZRP-3. This allows real-time continuous in-situ monitoring of compaction. As reservoir compaction is also important input into the seismological model, the studies into seismicity in the Groningen gas field have led to an intensified interest in compaction. In 2015, the existing methods as well as a newly developed method to analyse in-situ measurements of compaction in the monitoring wells were reviewed in detail (Ref. 1). This was followed by a more detailed review the in-situ compaction data via gamma ray marker surveys carried out since 2015. The review focussed on the uncertainties in the compaction measurements and whether it is sufficiently accurate to monitor reservoir compaction at the desired depth and time scales. Compaction can also be measured with the new technology of fibre-optic cables. A glass-fibre cable was installed over the reservoir section of the Zeerijp-3 monitoring well. A year after taking this in-situ compaction measurement system into operation a report describing the first year of experience with this new technology was published. The current report builds on this and describes the experience in the first four years of operation. An almost continuous compaction data set has been acquired in the Zeerijp-3A well. In this report the data set is discussed with attention for a number of significant events

	taking place in these four year, a coiled tubing clean out (CTCO) of the monitoring well, an earthquake of magnitude 3.4 occurring less than 1.5km from the well, an upgrade of DSS interrogator module, and multiple periods of active geophone operation. This report supports the development of a surveillance plan for the Groningen field.
Associated research	(1) Development of compaction models based on core measurements. (2) Inversion of subsidence to derive compaction estimates. (3) Seismological modelling.
Used data	In-situ measurements of compaction by logging relative movement of gamma-ray markers installed in observations wells.
Associated organisations	Baker Hughes.
Assurance	Internal.

Analysis of and learnings from the first four years of in-situ strain data in Zeerijp-3A

Pepijn Kole, Matt Cannon, Jelena Tomic, Stijn Bierman

Table of Contents

Acknowledgements

1   Introduction

The distributed strain sensing (DSS) fibre optics installation in the Zeerijp-3A (ZRP-3A) well has been operational since 12 October 2015 and collected almost four years of in-situ strain data from the Groningen field at the time of writing. A report was written, detailing the first year of data [1]. There, it is shown how drilling induced processes manifest themselves in the first few months of data and demonstrated confidence that the cable is strain-locked to the formation and collecting strain data that is representative of the compacting reservoir.

Here, we summarise the data collected since then, spanning now nearly four years, with only a few data gaps across the monitoring period. Since the writing of the first-year report, a few significant events have occurred in the well that warranted more in-depth investigation of the strain data. These events were a coiled tubing clean out (CTCO) of the monitoring well, an earthquake of magnitude 3.4 occurring less than 1.5km from the well, an upgrade of DSS interrogator module, and multiple periods of active geophone operation.

A general update of the strain data is given in Section 2, including detailed strain profiles and build-up for different formations and depth intervals. Insights from the monitoring, including during some significant events, are presented in Section 3. The results of frequency analysis are presented in Section 4, where the presence/absence of spatial and temporal (e.g. tidal, or seasonal production fluctuations) frequencies is studied. A comparison and correlation of the data to log data and core data from the same well is presented in Section 5 and Section 6, respectively. Section 7 discusses the early results of a comparison between the measured strain and the measured energy released by earthquakes, where both data sets are acquired in the same well (Zeerijp-3A).

2 General data update

2.1 Processing summary

The DSS and DTS data is processed using Shell plugins in Techlog. These plugins are used to filter the data in time and depth, which effectively uses the data redundancy for analysis to reduce noise [1]. Blackman-Nuttall filters are used for these purposes with typically a 48hr window over time and 1m in depth. The temporal resolution of the output data is typically 12hrs but can be reduced to 1hr if high temporal resolution is required (e.g. the frequency analysis in Section 4).

The Zeerijp strain data is not corrected for temperature. Gradual changes in temperature will cause apparent strain signals on the DSS cable, however the noise of the DTS data (scatter on the order of $0.5\,^{\circ}C$) is believed to be larger than actual thermal fluctuations in the well, in which case the application of a thermal correction will only add noise to the strain data. With a thermal correction factor of 6.5micro-strain/$^{\circ}C$, the noise would add scatter of several micro-strain to the data. Additionally, the measured DTS signal is known to occasionally show jumps in temperature by sometimes more than $1\,^{\circ}C$, caused by sudden changes in the ambient temperature of the DTS interrogator (this can happen when the data cabin is opened, and no air temperature control is in place).

The initial settling period, as discussed in [1], is usually ignored in strain calculations unless stated otherwise. Data acquired during periods when geophones were operational, are also excluded from the analysis, using an exclusion filter in depth and time to remove all areas where geophones are believed to leave a thermal imprint on the strain data. The reason for excluding these intervals rather than correcting for them, as can be done for gradual changes in temperature, is that the spatial resolution of the DTS data in depth is not high enough to correct for the full profile of the thermal anomaly.

2.2   DSS and DTS data overview in Zeerijp-3A

The strain profile, accumulated from 1 March 2016 (excluding initial settling time) to 12 August 2019 (the day at which the data was downloaded and processing) is plotted as a function of depth in Figure 1 in blue. The black horizontal bars indicate the average strain for each interval as used in the dynamic reservoir model, and green shading indicates the uncertainty in the mean, while the pink shading indicates the variation of strain within each zone, using two standard deviations. The intervals of the main formations are listed in Table 1.

The highest average strains are within the upper Slochteren, reaching over 100μm/m for most of the zones. The intervals in the lower Slochteren remain around 70μm/m with some variation. Notably the intervals in the Carboniferous also show non-zero strain, which are discussed in more detail in Section 2.3.4. Even when the zone of high strain in the Ten Boer[1] is excluded, the strain in the Ten Boer is still non-zero and compressive. More detail on the strain in the Ten Boer is discussed in Section 2.3.3.

Assuming a depletion rate of 2.5bar/year in the Slochteren, the depletion rates in the reservoir range roughly from 10 to 20μm/m/bar. These rates are very comparable to the historic compaction data from nearby Stedum-1 well, see Figure 2, especially considering the uncertainty and scatter from the gamma ray marker data and the low pressure depletion window of less than 10bar over which the strain rates from DSS were derived.

More detail of the strain across different intervals is given in Section 2.3. The strain data is correlated to well log data in Section 5, and to core data in Section 6.
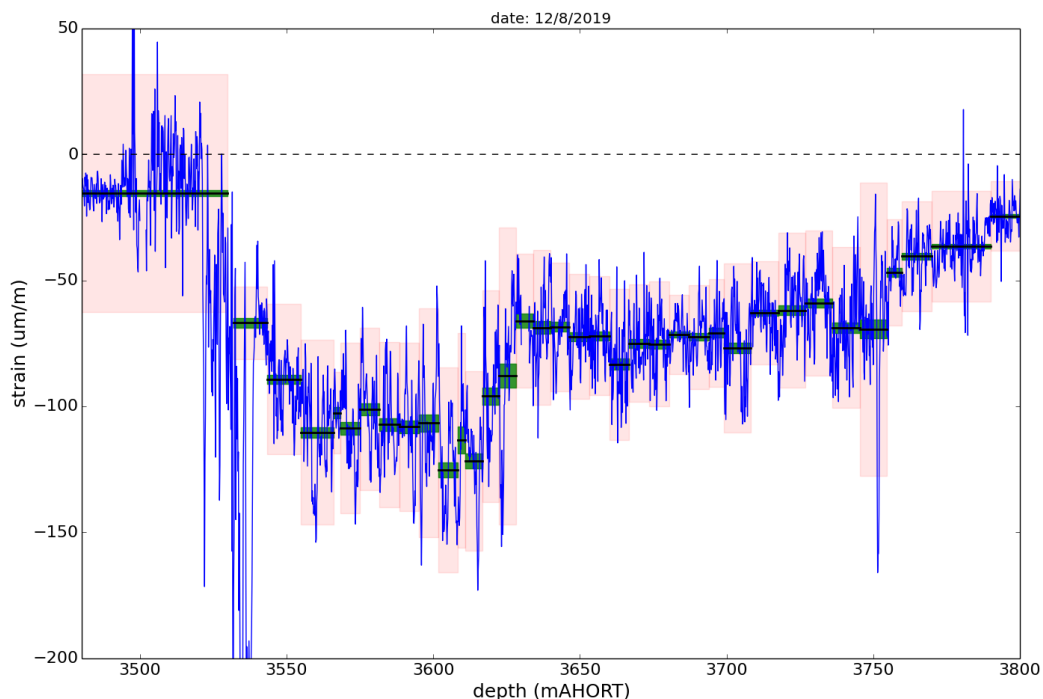

Figure 1: Strain profile vs depth for Zeerijp-3A, between 1 March 2016 and 12 August 2019.

---

[1] The strain in this zone was attributed to a drilling-induced local depletion of a sand pocket due to the sudden, very high strain rates that were not observed in surface data [1].

Table 1: Formation intervals along the DSS section of the Zeerijp-3A well

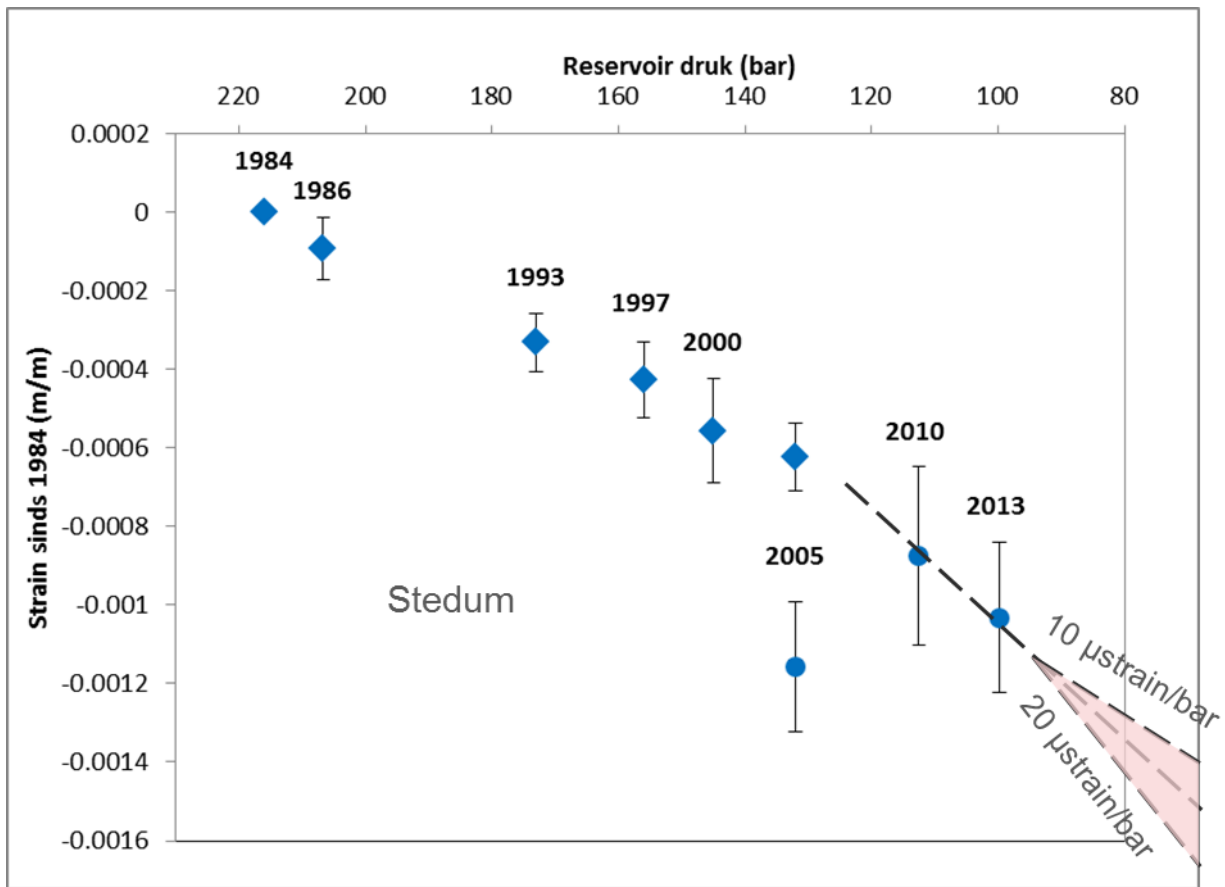| Zone name	Top (mAHORT)	Base (mAHORT)
ZEZ2H	2845	3428
ZEZ-(A-C-W-C-K)	3428	3475
ROCLT	3475	3539
ROSLU	3539	3639
ROSLL	3639	3755
DC	3755	3821

Figure 2: Strain in Stedum-1 well, measured using gamma ray marker surveys. The range of strain rates as derived from the DSS data, using only less than 10bar of depletion, are imposed in pink shaded area on the figure.

The average temperatures across the formations plotted in Figure 3 show signatures of some significant events, that have to be considered when analysing the data in greater detail. For example, the thermal impact of geophones are clearly visible on the DTS data, appearing as zones of 1-2m that are heating up by a few degrees during geophone activation, even when looking at the average over formations of several 10s of meters as is the case in Figure 3. Especially apparent is the heating from the lower most unit in the tool string during the first geophone period, which span from late 2015 to early 2016, and is clearly visible on the "*DC btm*" curve as a temperature increase of about 7°C. As mentioned above and discussed in [1], the low spatial resolution of the DTS data, giving a reading every 1m, makes it difficult for accurate thermal correction of the strain data for geophone events.

Also visible in the DTS data is a small spike in October 2017, raising the average temperatures across the DSS interval by almost 1 °C for a very small period of time. The temporal increase coincides with a coiled tubing clean out (CTCO), which is discussed in more detail in Section 3.3.

The last features worth pointing out in Figure 3 is the jitter and irregular steps in temperature readings, most apparent after the first geophone period and lasting throughout most of 2016. These correlate very well with the ambient temperature of the DTS interrogator, and are therefore believed to be an imprint of changes of the temperature in the data cabin at surface, and not actual downhole temperature fluctuations [1]. Once this became apparent, the temperature control in the data cabin has been improved to prevent continuous step changes in DTS signals.
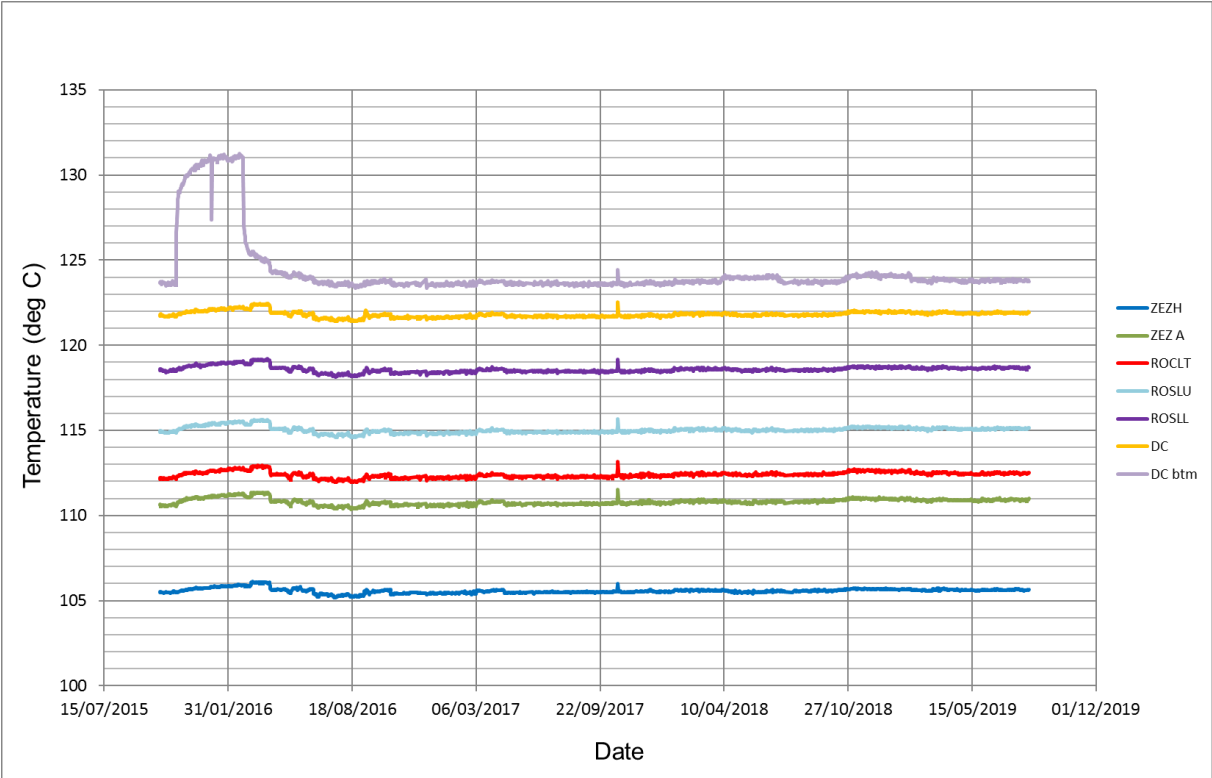

Figure 3: Formation average temperatures over time, as recorded by DTS in ZRP-3A.

2.3   Strain per zone

2.3.1   Formations

Here we show the analysis of the strain with averaging done for all formations, using the horizons as picked for the Zeerijp-3A well as the interval boundaries. Figure 4 shows the strain profile across the well with the average strains and uncertainties therein for each formation (from shallow to deep: Zechstein Halite, base Zechstein, Ten Boer, Upper Slochteren, Lower Slochteren, Carboniferous; see Table 1). Visible again here is that the Ten Boer, but also the Zechstein formations show some small but noticeable compressive strain.

The evolution of the average strain, including the uncertainty, are shown over time in Figure 5. The strain is set to zero in March 2016 to exclude the strain build up during the initial settling of the well and strain cable. The averaged strain during the settling period is included in Figure 5 for completeness. The strain rates over the ROSLL, ROSLU and DC remain fairly constant throughout the monitoring period.

The averaged strain in the Zechstein and Ten Boer intervals however, seem to have started to become visibly non-zero since about late 2017. The strain is visible in both the Channels of the DSS cable, so not likely due to some anomalous reflections. Also, it is not likely due to thermal effects, as the temperature recorded by the DTS seems to show near-constant temperatures, see Figure 3. For the temperature to explain the strain build-up of 10-20μm/m in the Zechstein and Ten Boer, a cooling of these zones of 2-4 °C should have taken place, with is not observed in the DTS data and would be well above the noise levels and detection thresholds of the DTS. The strain in the Zechstein is discussed in more detail in Section 2.3.2 and the Ten Boer in more detail in Section 2.3.3.
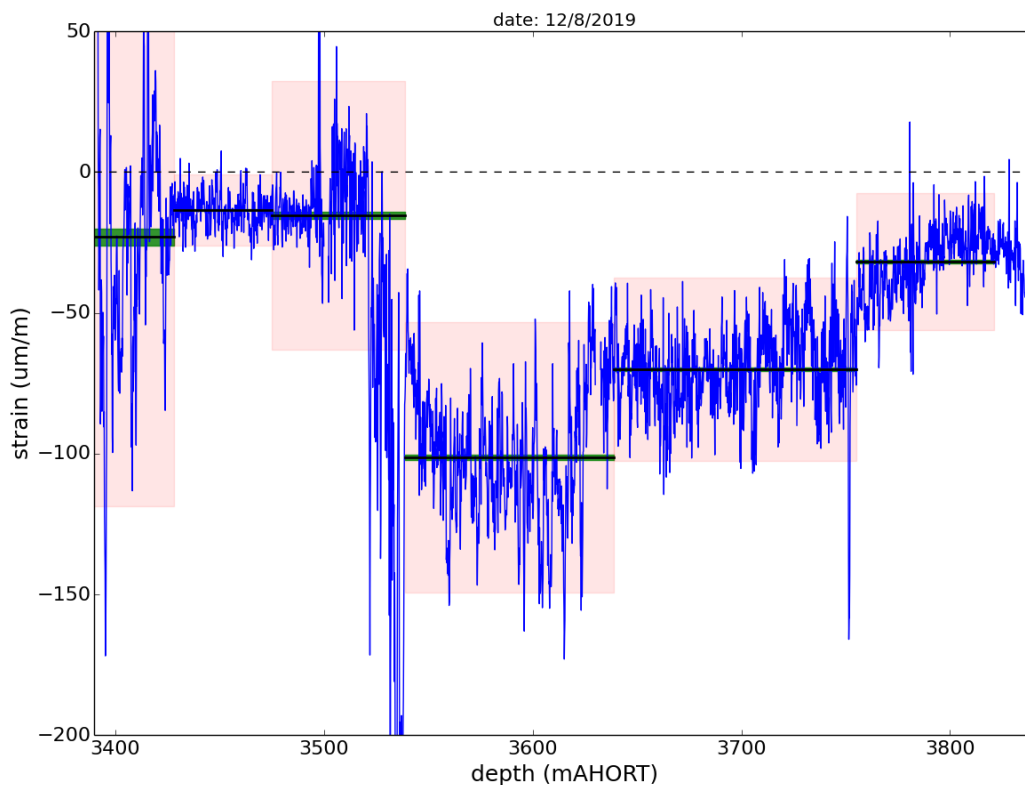

Figure 4: Strain accumulated between 1 March 2016 and 12 August 2019. Averages and uncertainties in the average are now shown for each formation.
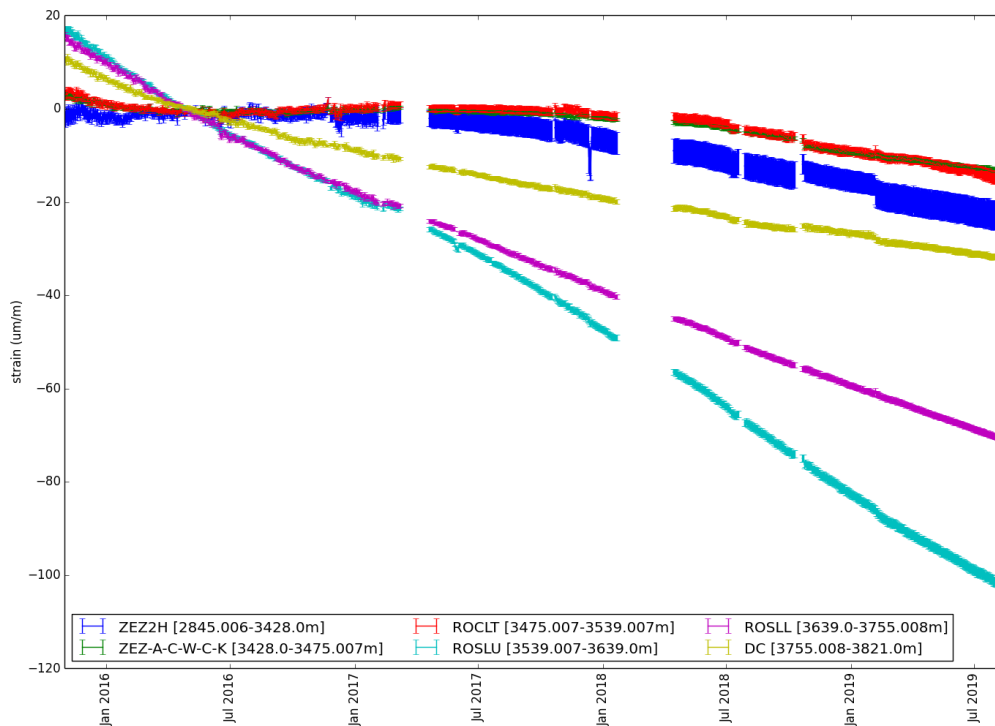
Figure 5: Formation average strain as a function of time.

2.3.2 Zechstein

The strain accumulated across the Zechstein is plotted in Figure 6, with an interval average shown for every 5m. The top of the Zechstein shows fluctuating amplitudes of strain, with parts of the interval showing extensional signals. The base of the Zechstein shows a more monotonic, non-zero compressional strain.

An explanation of the change in signal character can be the alignment of the change with a lithological boundary, seen on well logs as a change in the velocity [1]. It could also be a complex signature resulting from the salt slowly squeezing onto the casing, and the interplay of salt and cement. It has to be noted thought that the strain on both Channels across this interval appears comparable, which suggests that strain is mostly axial and not due to bending of the casing. The DSS cable is not sensitive to ovalisation of the casing due to the orientation of the fibre along the length of the casings.

The more detailed build-up of the strain over time is provided in Figure 7, showing the average strain over time for each of these 5m intervals across the Zechstein. The average strain in some of these intervals is initially seen to increase and become extensive, but in the latter phase of the monitoring, from late 2017 onwards, all intervals show a slow but noticeable compression.

The base of the Zechstein, though also shows compressive strain, very minimal but noticeable in Figure 5 and Figure 7, even in the very dense and therefore assumed tight and stiff anhydrites at the base of the Zechstein. Presence of carbonates in these zones could provide some depleting intervals but these are not expected to exist across the full monitored interval here.
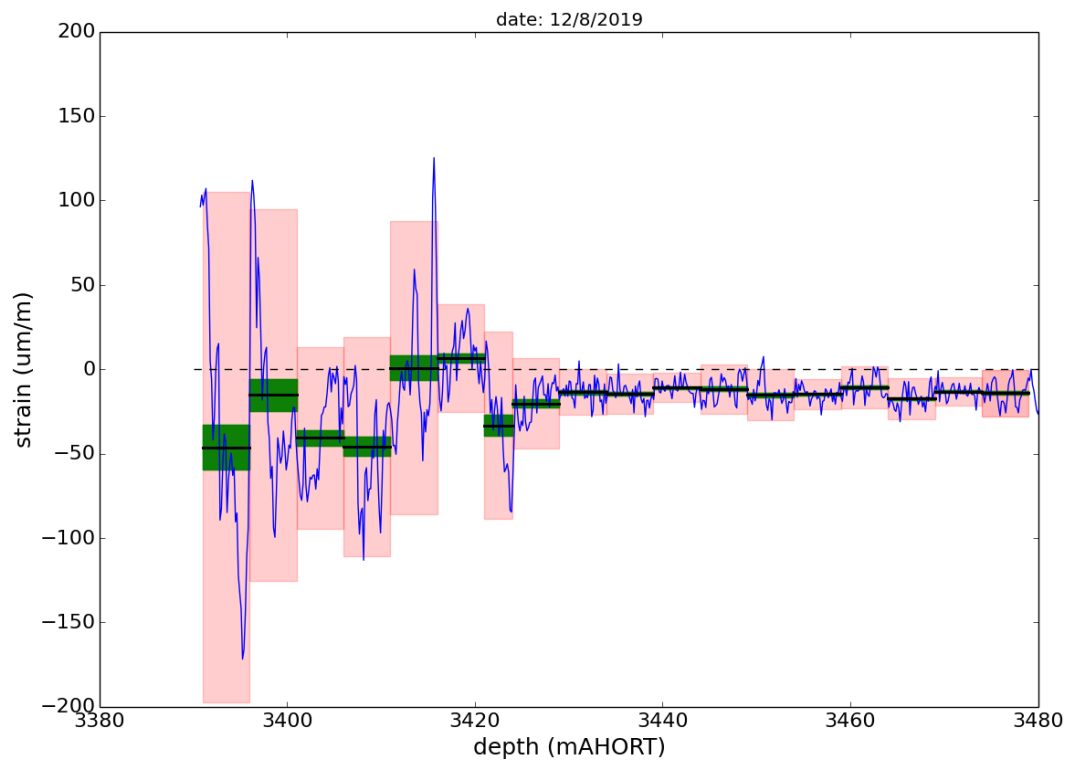
Figure 6: Strain accumulated between March 2016 and August 2019 over the Zechstein. Averages are plotted for each 5m interval.
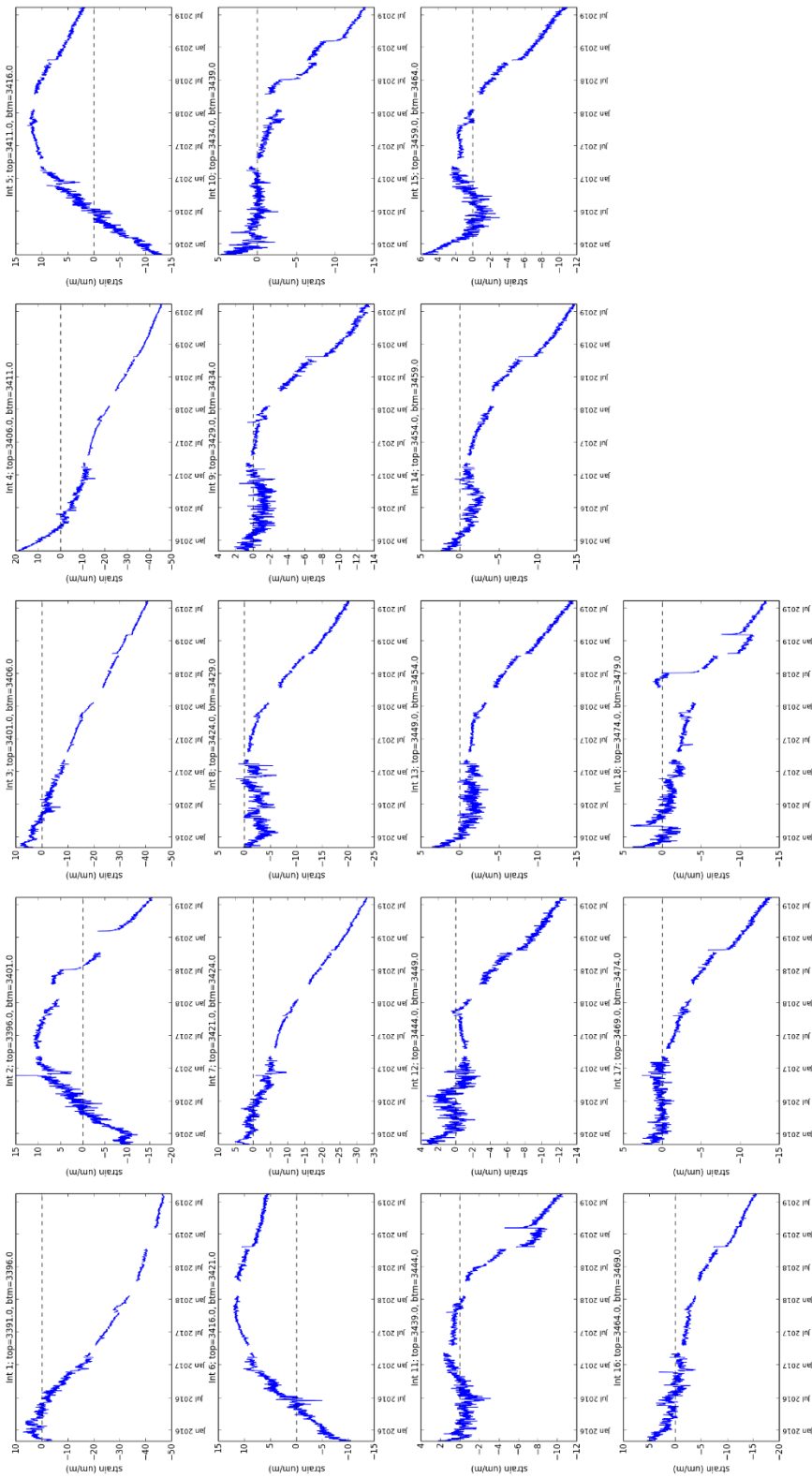
Figure 7: average strain for the 5m Zechstein intervals in Figure 6, as a function of time. Note that some features due to geophone operations are still visible in this plot, even though the geophone data is not included in the averages. The features appear as on the transition through these geophone epochs, the data from certain depth intervals (geophone locations) is excluded, to be included again after the geophone epoch, allowing for some jumps in the average.

2.3.3 Ten Boer

The strain accumulated between March 2016 and 12 August 2019 is plotted along the Ten Boer interval in Figure 8. The averaged strain is plotted for a range of sub-intervals, being the Ten Boer section above the casing shoe [3475-3497mAHORT], the Ten Boer interval of 5m around the casing shoe [3497-3502mAHORT], the central part of, and the larger extent of the zone of high strain rates in the Ten Boer [3533-3538mAHORT and 3530-3539mAHORT, respectively], and the mid and base of the Ten Boer [3502-3520mAHORT and 3520-3539mAHORT, respectively].

The zone of high strain rates is sometimes referred to as the 'Ten Boer event', and is discussed in the previous DSS report [1]. The event shows a sudden start of a compaction zone, initiated a few weeks after the DSS system came online, in late 2015. It is now believed to be compaction linked to a drilling related depletion (possibly cross flow), or otherwise a very localised depleting pocket, as no local acceleration of surface subsidence is observed. The compacting zone was seen to extend in depth over time, and has reached a constant strain rate over time, see Figure 9.

The intervals that show most significant strain in the Ten Boer are those that include the Ten Boer event. The mid and top of the Ten Boer show similarly low strain rates, as does the casing shoe, albeit with a bit more scatter and higher uncertainty in the latter interval. These lesser compacting zones reached up to about 10μm/m strain. From the evolution of the strain in these zones pictures in Figure 9, one could possibly see an oscillating behaviour in the strain of these zones, with a very low frequency of 3years. Ideally one would wait and collect data over a longer period (>>3 years) to make statements about the existence of such low frequencies in the data.
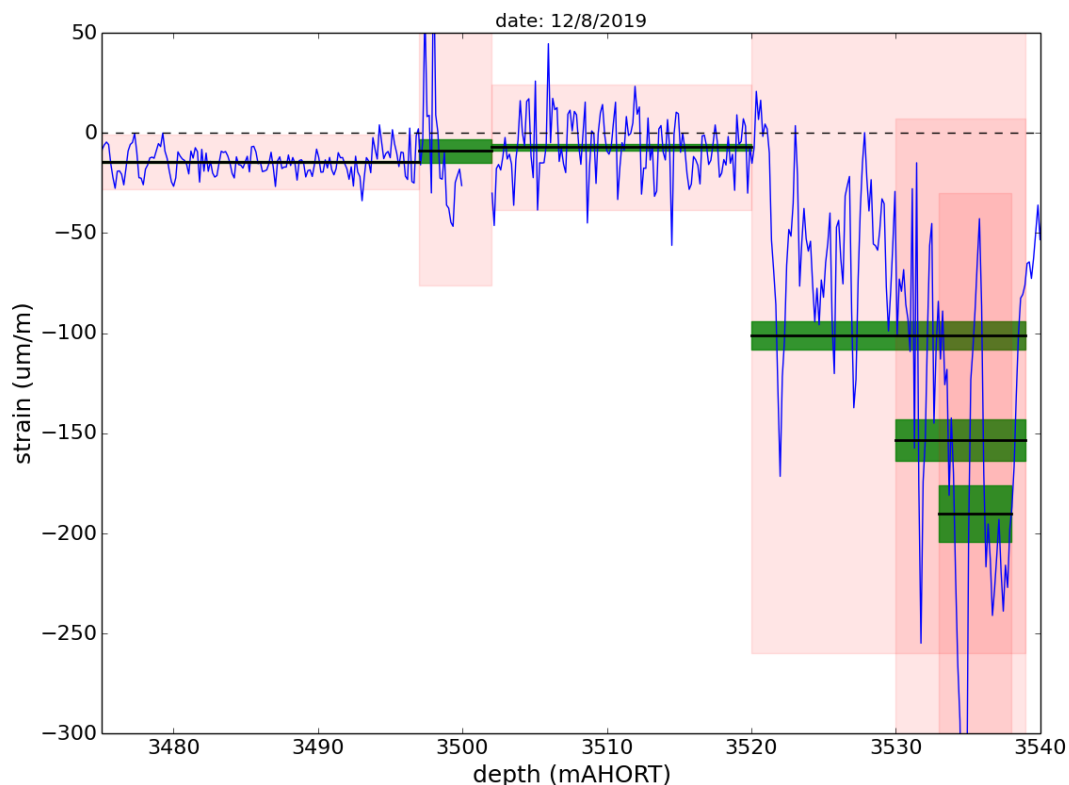

Figure 8: Accumulated strain between March 2016 and August 2019 across the Ten Boer (ROCLT). Indicated in black horizontal lines are the zonal averages, with green indicating the uncertainty in the average strain and pink shading indicating the two-standard deviation interval.
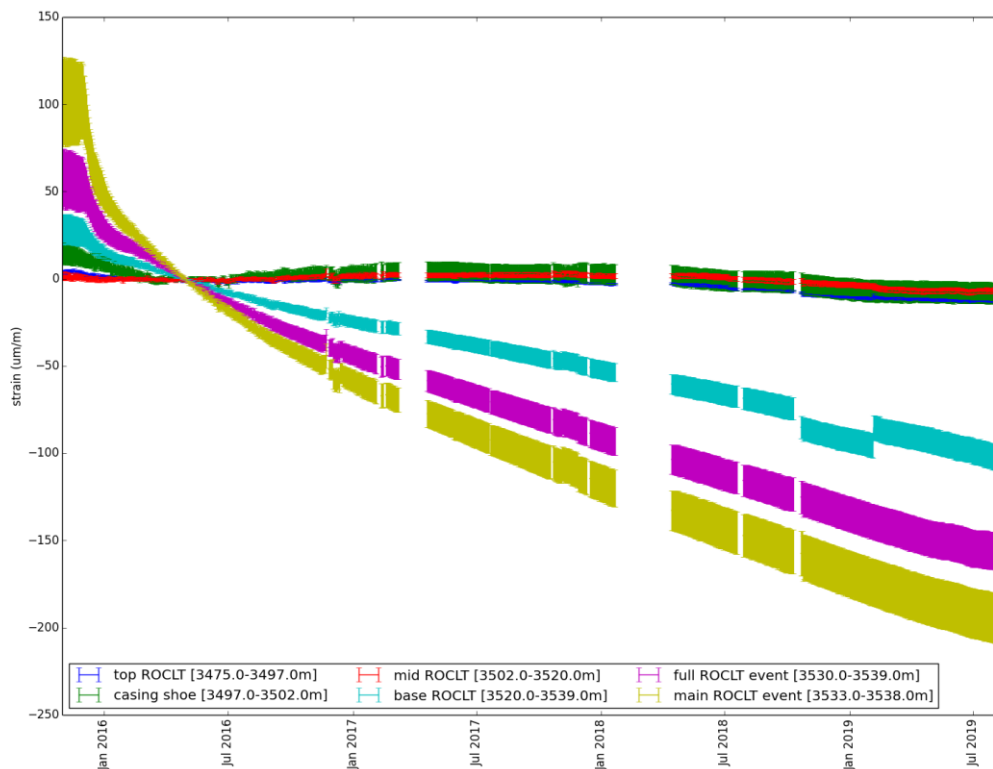
Figure 9: Average strain for different intervals within the Ten Boer, as a function of time. Note that some features due to geophone operations are still visible in this plot (e.g. base ROCLT around January 2019), even though the geophone data is not included in the averages. The features appear as on the transition through these geophone epochs, the data from certain depth intervals (geophone locations) is excluded, to be included again after the geophone epoch, allowing for some jumps in the average.

2.3.4 Carboniferous

The accumulated strain across the monitored interval of the Carboniferous is plotted in Figure 10, with the average strain over time for each interval shown in Figure 11.

The whole Carboniferous interval that is covered by the DSS cable shows a non-zero, compressive strain that gradually compacts further over time. The initial strain rates in the first six months or so after installation were significantly higher, some of which can be attributed to the settling of the well, and part of it, especially in the lower parts of the cable, to the initial geophone installation which significantly affected the temperature around the well bore (see Figure 3).

The strain rate later on, however, seems to be fairly gradual and constant, and cannot be explained by changes in temperature or anomalous signals in the DSS. The signals are also consistent between the two Channels that cover this part of the Carboniferous, ruling out any bending or channel related issues that cause these signals.

It is therefore believed that the Carboniferous, at least at the location of Zeerijp and over the interval that is covered by the DSS cable, is actually compacting and therefore likely also depleting.

The interface between the Slochteren and Carboniferous shows most strain, and the compressive strain gradually decays with depth, until it appears to increase again for some deeper intervals (Figure 10). The same is visible when plotting the strain over time (Figure 11). The strain across the deepest interval is initially strongly affected by the geophone operations, where the lowest module

of the geophone string was heating up the most. After some time, though, and well after the initial geophone period, the strain rate seems constant also for the deepest interval.

Note that some jumps associated with the geophone operations still persist in the data, especially visible in the average strain of the deepest part of the Carboniferous, even though the data directly affected by the geophones is excluded from the data set (both in depth and time). As Figure 11 shows the average strain taken over an interval, these averages can experience a sudden shift across the geophone interval when excluding or including parts of the interval again, when the strain pattern across the interval is very heterogeneous, as is the case here. To completely remove these artefactual jumps, one has to exclude the whole interval during geophone operations, and not just the geophone part itself. Here, we chose to include it still to visualise the trend of the strain during geophone operations. These jumps should not be included in trend analysis of the strain.

Being further away from the depleting Slochteren, one would expect to find the least depletion at deeper intervals, however as the dip angle of the Carboniferous is different from the bedding angles of the Slochteren, depletion paths between the two are not straight forward. Formation pressure tests have provided some evidence of depletion in the Carboniferous [2].

A comparison between strain and log data for the lower part of the monitored Carboniferous is shown in Figure 12. Note that the Carboniferous itself extends to further depths; only the monitoring interval is shown. The increase towards the bottom of the DSS cable coincides with changes in the local lithology or sedimentology, as evidenced on the logs and core photos in the figure: The interval has a higher reading on the density curve compared to surrounding rock, a higher slowness and seems to contain a higher number of high-density streaks seen on the core photos.

The increase in the density is likely due to the higher number of layers consisting of material with a higher density, and the decrease in velocity due to the layering. Based on log derived dynamic moduli, and compressibility, one would expect a stiffer material when looking at the density curve, but a softer material based on the sonic data. However, the presence of different materials and possibly their layering and structure plays a role in the behaviour, for both depletion and compaction.

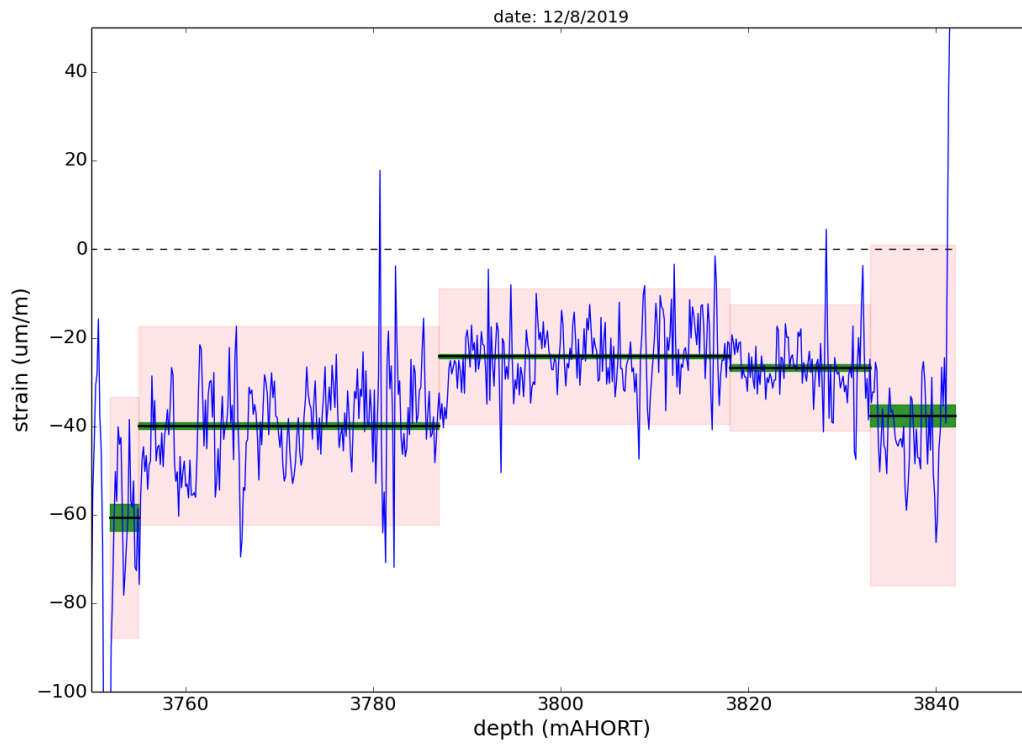Core analysis of the Carboniferous is currently still ongoing.

Figure 10: Accumulated strain between 1 March 2016 and 12 August 2019 across the Carboniferous.
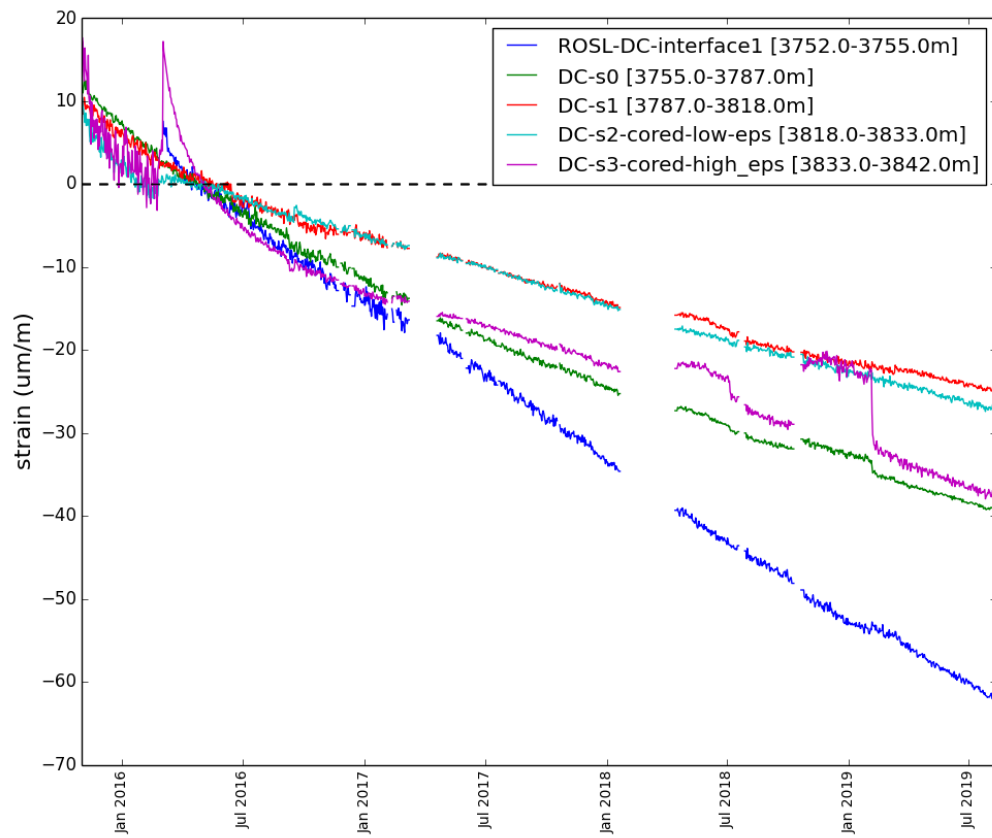
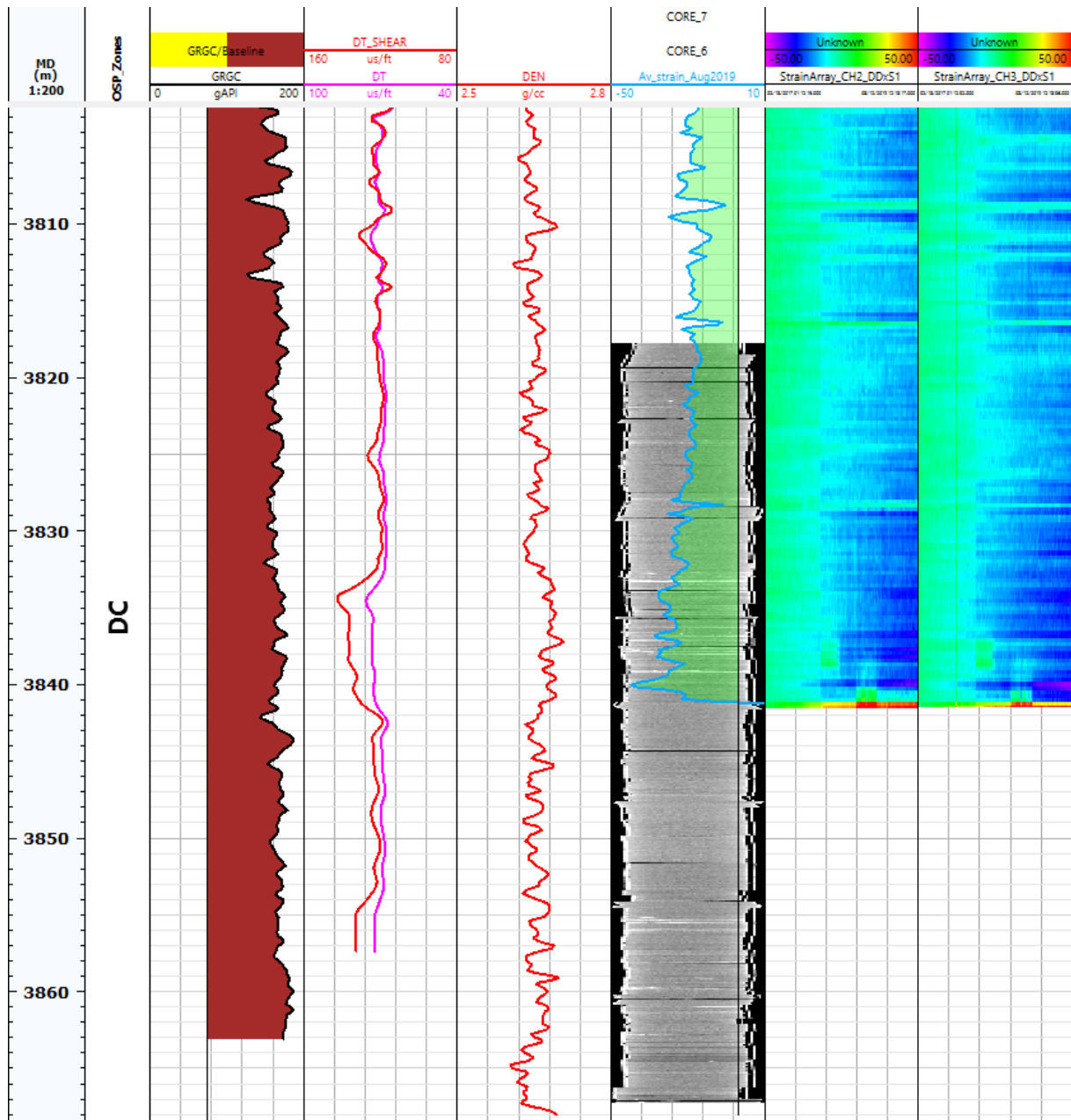*Figure 11: Average strain for the carboniferous intervals over time.*

Figure 12: Strain and log data across the Carboniferous.

3 Insights derived from Zeerijp fibre optics data

3.1 Zeerijp earthquake

On 8 January 2018, an M3.4 earthquake occurred at a distance of about 1.5km, relatively close to the Zeerijp-3A well. In general, if an earthquake occurs, it is implied that the fault(s) have moved. Depending on the amount of fault offset and the proximity of the earthquake, it could be possible to detect a sudden change in strain in the surroundings of the fault. If the strain extends far enough and has enough signal, it could be detected by the DSS.

Figure 13 shows the compaction across the reservoir (top figure) and the change in strain (bottom figure), over a period that spans a few weeks and includes the M3.4 earthquake, the timing of which is marked by the arrow. The signals before and after the earthquake appear highly similar, where no changes are visible in the trends above the noise levels. To verify if the strain resulting from the earthquake is localised, the averaged strain before and after the event is plotted in Figure 14, where the strain as a function of depth does not show any indications of sudden local movement that coincides with the earthquake.

From these comparisons, it appears that even the M3.4 event generates strains below the resolution of the DSS installation (order of 1μm/m) at a distance 1.5km from the monitoring well.
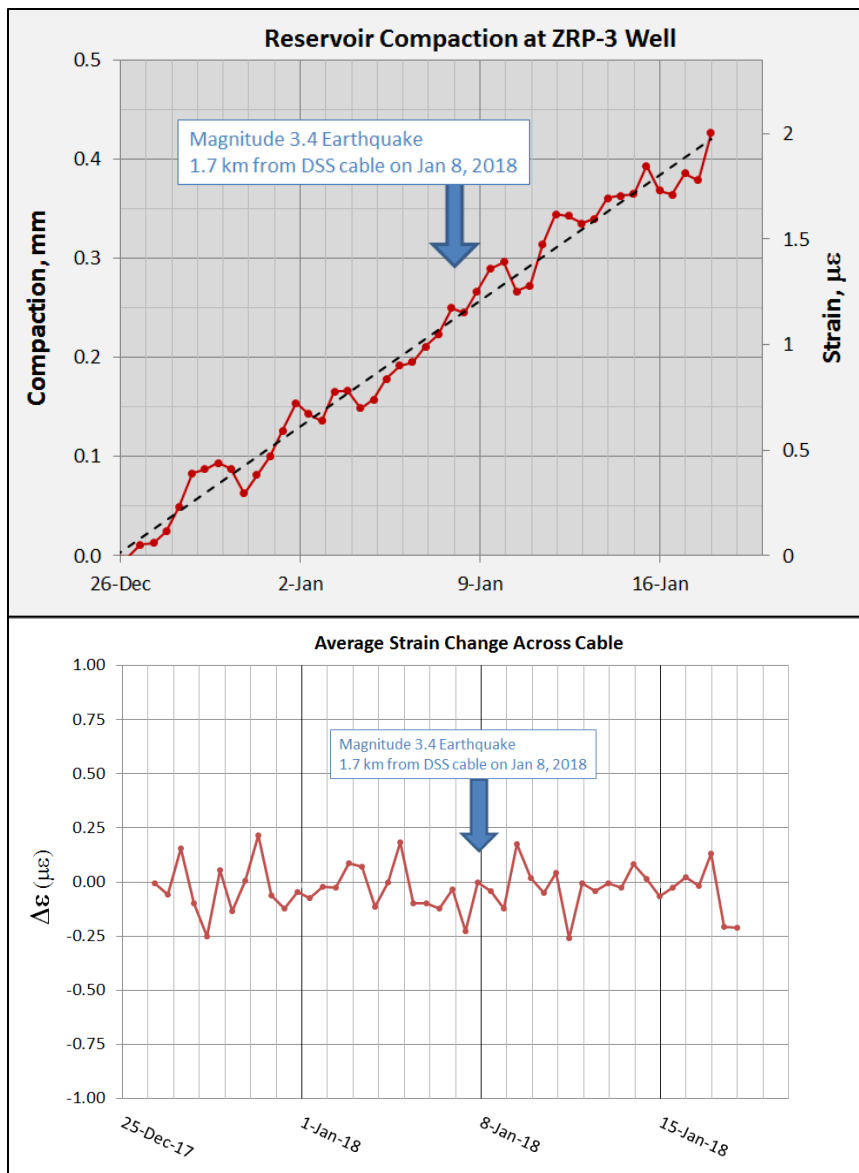
Figure 13: Reservoir compaction (top) and strain change (bottom) over a time period of a few weeks, that includes the M3.4 event nearby Zeerijp-3A.
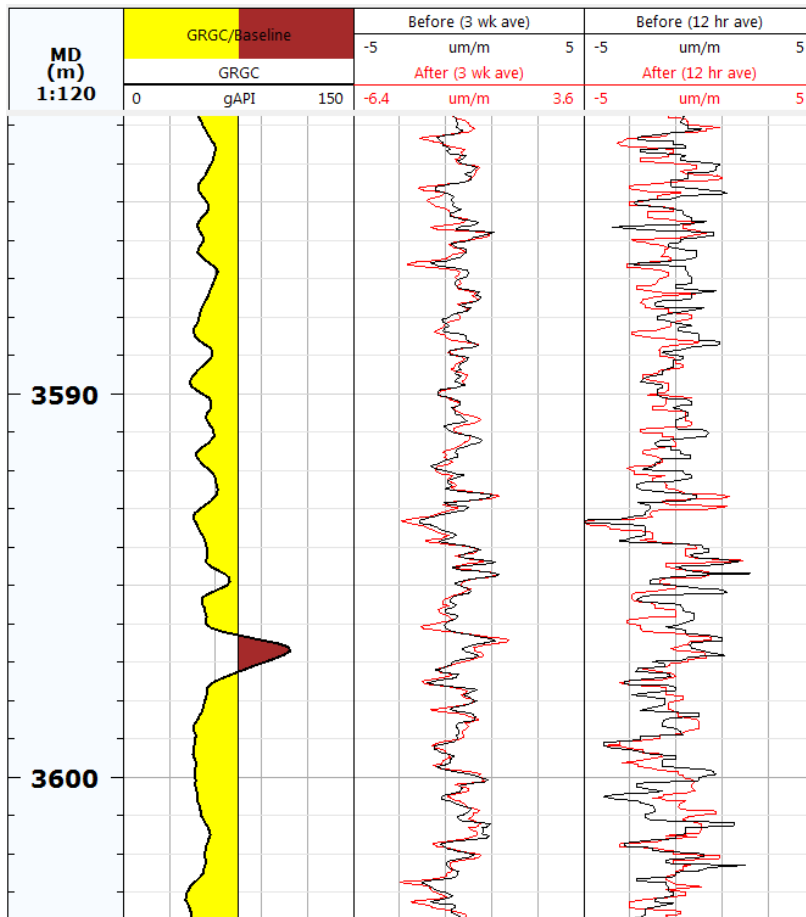
Figure 14: Averaged strain before and after the event, along the reservoir.

The earthquake magnitude depends on both the fault size and the amount of fault slip: a large fault size with small amount of movement will result in the same magnitude event as would a small fault size with a large displacement. The latter case would have the most potential to be observed by DSS.

A separate study looked into the data in more detail and simulated the strain expected for a M3.4 earthquake, to study the magnitude of strain signals that can be expected, and under which circumstances it might be detectable. They simulated the strain across the DSS cable for both these end members, using the true fault and well geometry. The two cases were 1) high stress drop (10MPa) combined with small fault size (400m) and 2) a low stress drop (0.1MPa) combined with a large fault size (1.6km).

The expected strain along the DSS cable for the two endmembers is shown in Figure 15 and Figure 16, respectively. Even the large fault case predicts a strain of only 0.1μm/m, which is below the noise levels of the DSS system, and therefore it is not expected that the M3.4 event would have been detected.

The recorded earthquakes in the Groningen field are plotted in Figure 17, showing their magnitude and proximity to the Zeerijp-3A well. Besides the event discussed above, there is an event of M2.1 at just over 160m away from the Zeerijp well. Here also, no sudden changes in strain were observed. As other events that occurred (during the time when the DSS was operational) occurred either further away or with lower magnitude than either of these two events, it is not expected that any other event has left a signature on the in-situ strain data as they are expected to cause less deformation.
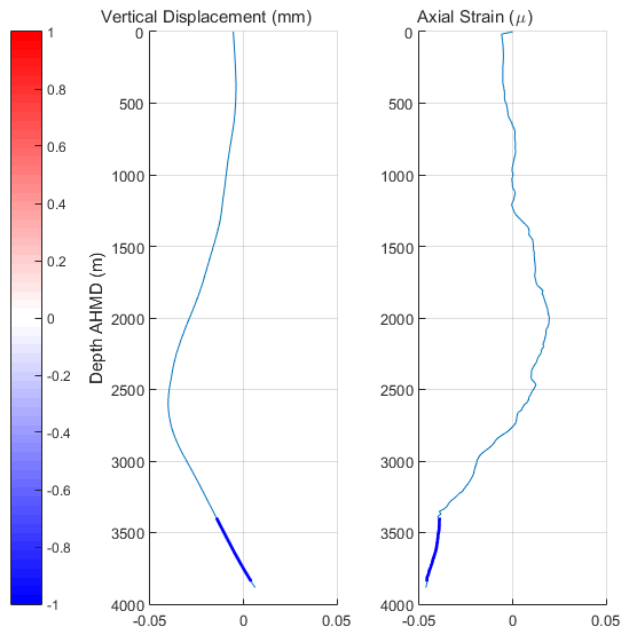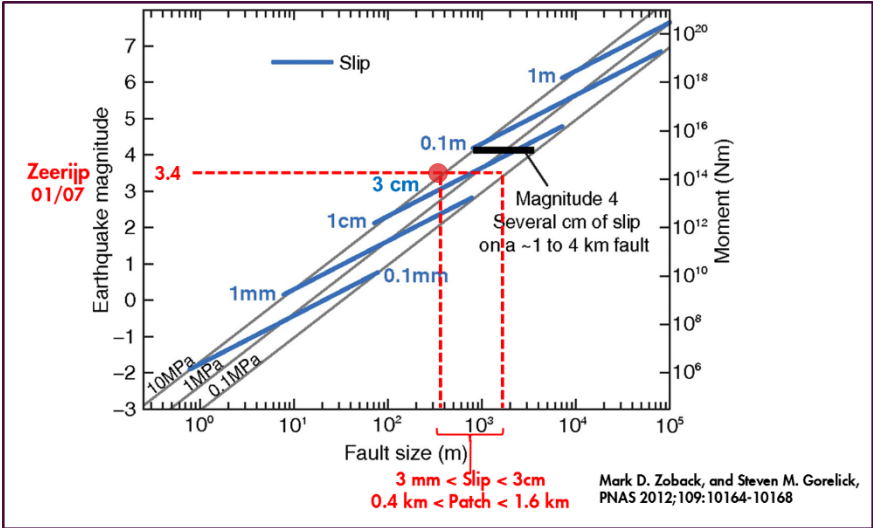
Figure 15: Simulated strain for a high stress drop with small fault size.
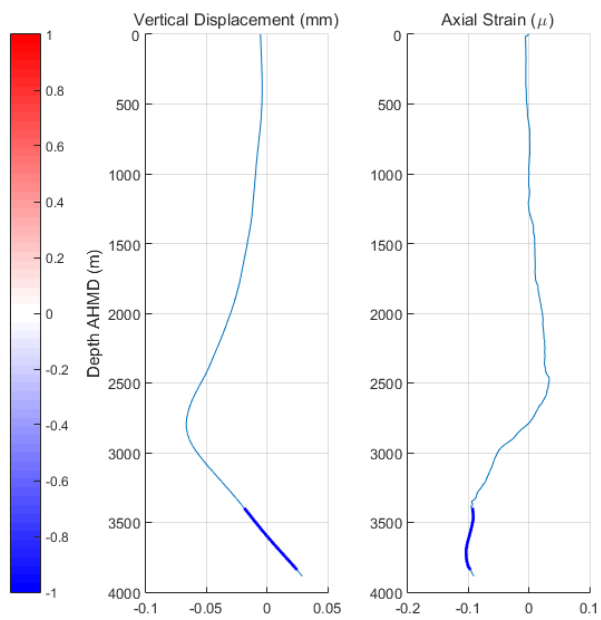
Figure 16: Simulated strain for a low stress drop with large fault size.

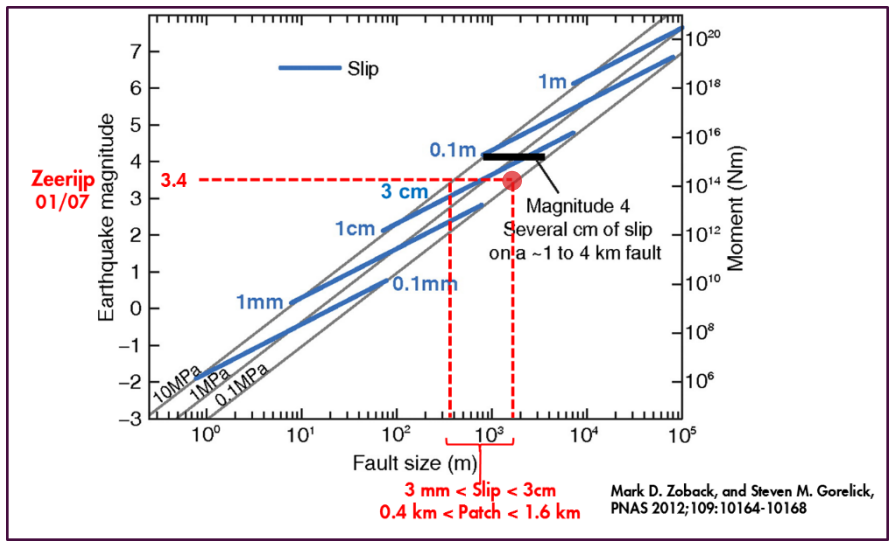*Figure 17: Recorded earthquakes in the Groningen field, and their distance to the Zeerijp-3A well. Events marked by orange squares are those that occurred after the installation of the DSS system. The labels indicate the date of the event.*

3.2 Estimates of static to dynamic moduli conversion factor

The data from Zeerijp provides a unique opportunity to compare the dynamic compressibility, derived from wireline log data, to the static compressibility, estimated from the strain data and depletion, using data for the static and dynamic estimates from the same well, and the same rock. The depletion is quite accurately known in the reservoir, based on reservoir models that are calibrated to (nearby) well data. More details of the analysis can be found in [3]; we give a brief overview here.

The uniaxial compressibility can be estimated from compressional sonic and density logs as:

$$C_{m,dyn} = \frac{1}{\rho V_p^2}$$

Where ρ is the density and V_p is the compressional velocity, both measured by wireline. Strain measured by DSS is related to the pressure drop and the static compressibility, assuming linear compaction, as:

$$C_{m,stat} = \frac{\varepsilon_{DSS}}{\Delta P}$$

Here, ε_{DSS} is the strain as measured by the DSS system and ΔP the pressure depletion from reservoir simulations. Both these properties are estimated over a fixed time interval, which here is from May 2016 till November 2017 (when the analysis was done). The annual pressure depletion is around 2.5bar/year, so for the time interval here we use a depletion of 4.5bar.

The used values are listed in Table 2 for the Upper Slochteren (ROSLU) and Lower Slochteren (ROSLL). Both result in an estimate of the conversion factor between static and dynamic compressibility (and other moduli) of 3, which is in agreement with other estimates for sandstone reservoirs in the Netherlands that was derived from surface subsidence [4].

Table 2: Static and dynamic compressibility factors for the upper and lower Slochteren.

Formation	ε_{DSS} (in μm/m, between May 2016 and Nov 2017)	ΔP (in bar, between May 2016 and Nov 2017)	$C_{m,stat}$ (μm/m/bar)	$C_{m,dyn}$ (μm/m/bar)	Conversion factor α ($C_{m,stat}$ / $C_{m,dyn}$)
ROSLU	45	4.5	10	3.5	3
ROSLL	35	4.5	8	2.5	3

There is no accurate estimate of the depletion in the Carboniferous, as at the moment it is not included in the dynamic reservoir models. Here, we can use the conversion factor derived for the Slochteren, and a range around it, to reverse engineer the problem and make estimates of the depletion, based on the observed strain. The values are listed in Table 3. When applying the same conversion factor for the Carboniferous as for the Slochteren, the estimated depletion is about 3bar, and fairly close to the depletion in the Slochteren. Using a one-to-one conversion results in a depletion estimate of 10bar, which is significantly more than the depletion in the Slochteren and therefore considered less realistic. A conversion factor of 1 is therefore probably too low. Increasing the conversion factor to 5, which is considered high and not observed in other data, reduces the estimated depletion to (only) 2 bar for the period May 2016 – November 2017. As conversion factors higher than 5 are not common, it can be concluded from the strain and dynamic compressibility here

that the depletion in the Carboniferous is indeed significant over the period May 2016 – November 2017, and a depletion of 2-3 bar over the monitored interval is not unlikely.

Table 3: Measured strain and estimated depletion across the Carboniferous (DC).

Formation	ε_{DSS} (in μm/m, between May 2016 and Nov 2017)	$C_{m,dyn}$ (μm/m/bar)	Conversion factor α ($C_{m,stat}$ / $C_{m,dyn}$)	Estimated $C_{m,stat}$ (μm/m/bar)	Estimated ΔP (in bar, between May 2016 and Nov 2017. Ranges shown between brackets)
DC	20	2	1	2	10 (5 - 15)
			3	6	3 (2 − 4)
			5	10	2 (1 − 3)

3.3   Learnings from fluid changeout

A coiled tubing clean out (CTCO) was performed around 19 October 2017, with the objective to change out the wellbore fluid from brine to DI water, in an attempt to increase the lifespan of the geophones. The short term thermal disruption provides an opportunity to assess the thermal strain correction factor that is used to correct strain data for changes in temperature. The correction factor has been determined in the laboratory, being a combination of a change in optical properties and thermal expansion of the DSS cable itself (which is a composite structure comprised of glass, metal, and polymers), amounting to about 25µm/m/°C change [5]. In a field installation in the US in an injection well with significant changes in temperature, it was found that the actual effective correction factor is closer to the optical component, being 6.5µm/m/°C [6]. The belief is that the amount of thermal expansion is reduced in the downhole environment, being in far higher confinement pressures than in the laboratory [5].

As the temperature in Zeerijp is assumed constant, or at least to within one °C, no temperature correction is applied to not introduce additional noise from the DTS. However, once noise levels on DTS systems can be reduced further in the future, and when it is found that temperatures do change in the reservoir, a reliable temperature correction of the strain is required. The small thermal perturbation introduced during the CTCO provides data that can be used for estimating the thermal correction factor for the Zeerijp setup.

The observed strain and temperature changes during the CTCO are plotted in Figure 18 for all four channels of the DSS. The data from the DTS is divided into the sections that coincide with the DSS channels. Figure 19 shows the same data, but highlights the location of the bottom of the CT assembly in magenta throughout the operations. The position clearly coincides with the increase in temperature and change in strain, indicating that these changes are indeed caused by the CTCO.

Figure 20 shows different visualisations to help assess the temperature correction factor. All point towards a factor of about 5-8µm/m/°C. These values are much lower than the laboratory estimates, but agree very well with the 6.5µm/m/°C as estimated from the injection wells [6], and typical temperature correction coefficients due to changes in optical properties of the fibre found in literature [7, 8, 9]. In both these downhole systems, the contribution from thermal expansion of the fibre seems negligible.

The effect of the thermal perturbation on the strain signal is analysed in a bit more detail below in Figure 21 and Figure 22 through the Fourier transforms of the strain signal over time and depth. The left column in Figure 21 shows the spatial transforms for the strain signal from the four DSS channels. The thermal disturbance from the CTCO occurs around 95hrs on the x-axis in these figures. Some structure in the spectrum can be observed along the y-axis in these transforms, which is an indication of some periodicity of the change in strain along the well axis during the CTCO.

The spectrum along the spatial frequency axis is shown at the time of highest signal disturbance (95hrs) in the left column of Figure 22, showing small peaks just under the 0.1/m frequency, coinciding with the casing length and average inter-clamp spacing. It is believed that the best thermal contact between the casing and the fibres are made at the clamp location, which is then also the location where the highest effect of thermal changes such as from the CTCO will occur on the strain signal.

The average change in the signal (offset signal at spatial frequency of zero) is shown over time in the right column of Figure 22. These show the average effective change across the measured interval over time, and give a clear indication of the duration of the disturbance of the CTCO on the strain

signal: the effect on the strain signals peaks rapidly during the CTCO, but then decays exponentially, with a decay time of several hours. The remaining strain signal is negligible after 10hrs or so. A similar analysis on the DTS signal shows that the measured temperature decays away at a similar rate as the measured strain, see Figure 23.

From this, we learn that the strain is only very temporarily affected by significant well interventions such as a CTCO. Well interventions like wireline operations are expected to cause much less of a thermal disturbance, and therefore would leave an even smaller (and possibly shorter) imprint on the strain data. One would still have to take care in analysing fibre optic data during periods of well interventions, however the data here suggests that the impact might be minimal.
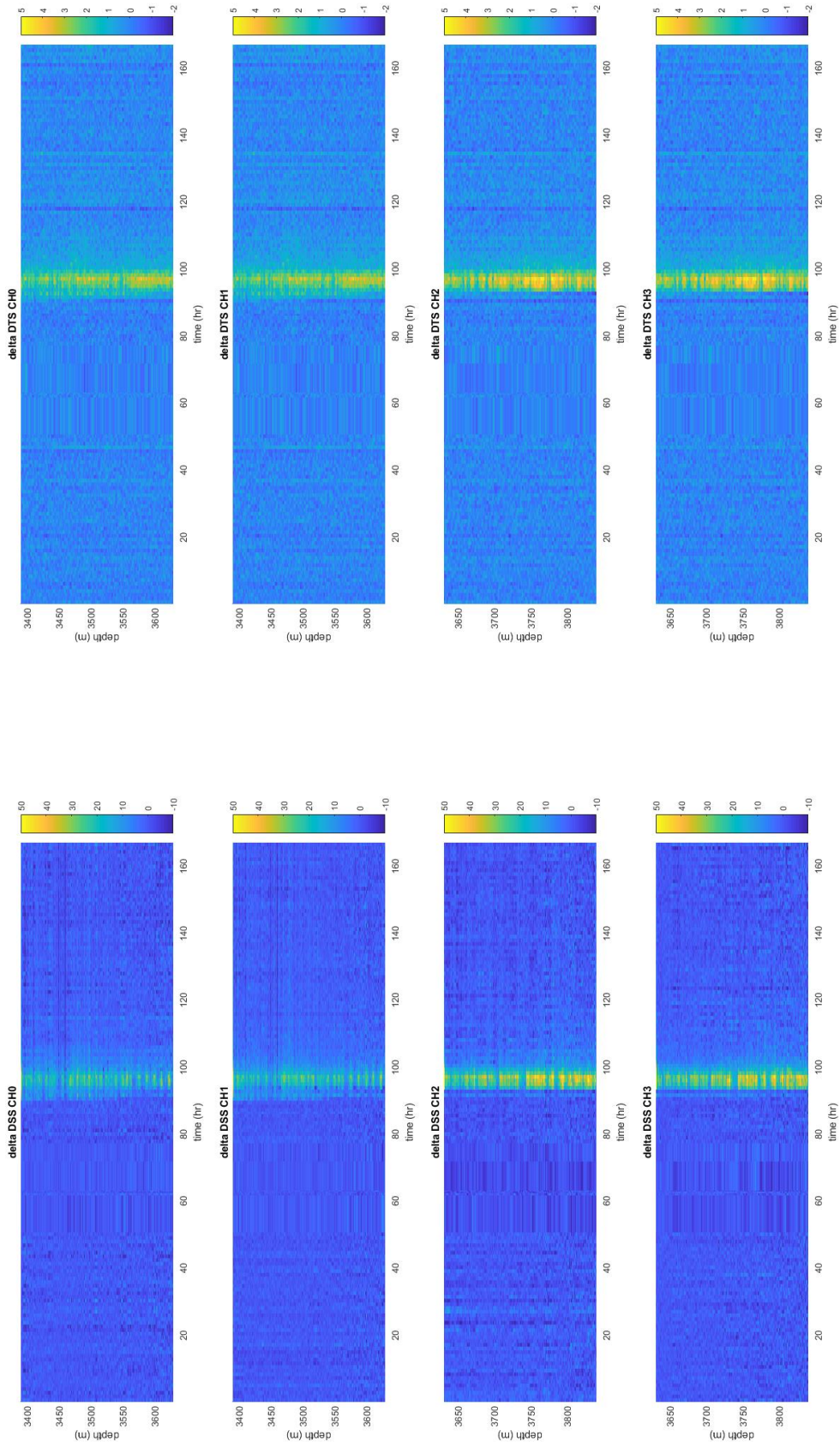
Figure 18: Data showing the temperature increase across the reservoir section by DTS, and the apparent strain as recorded by the four channels of the DSS cable.
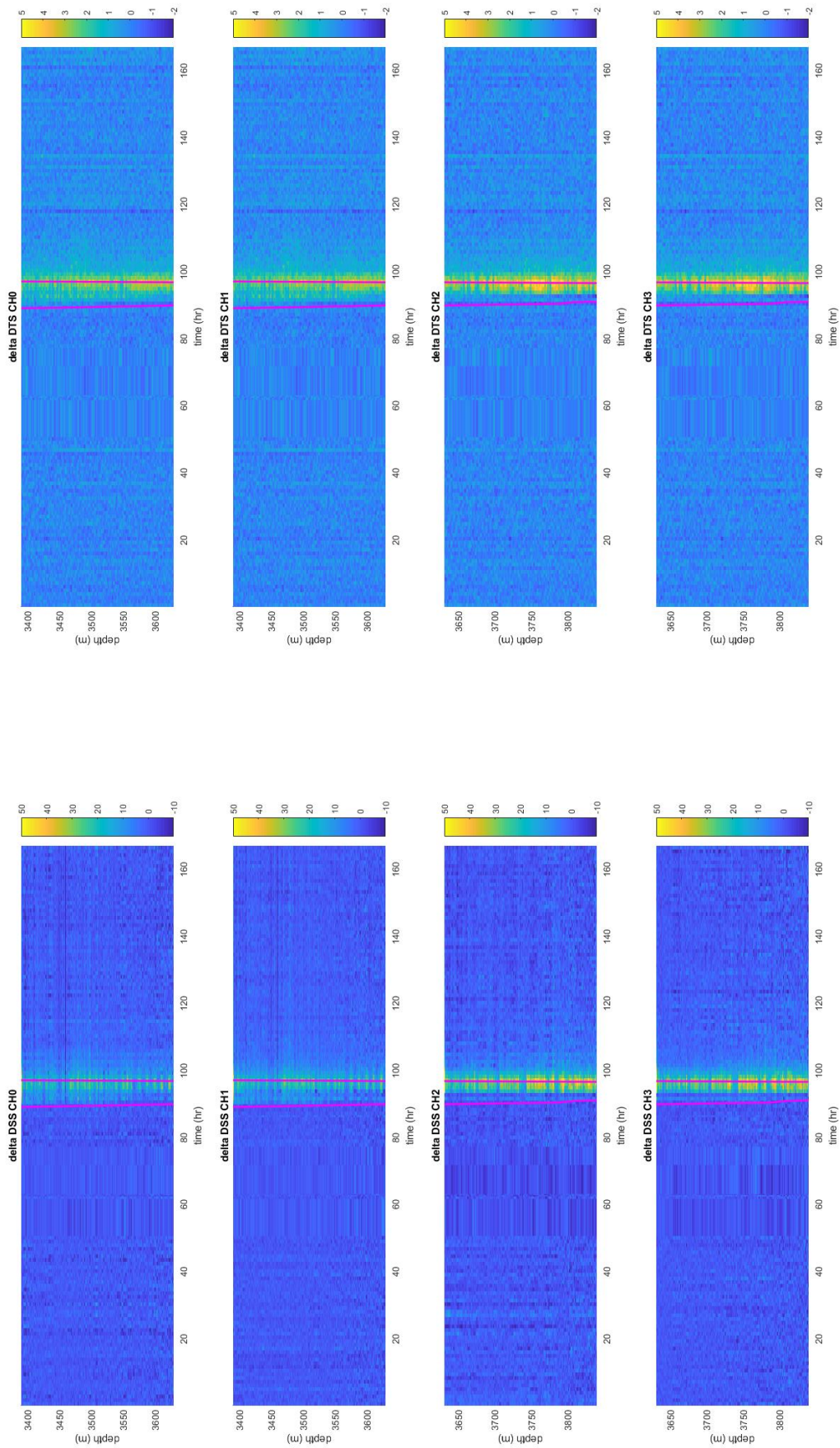
Figure 19: Same as Figure 18, but now also including the position of the bottom of the coiled tubing unit during run in and run out of the hole, over time, clearly coinciding with the observed change in temperature and strain.
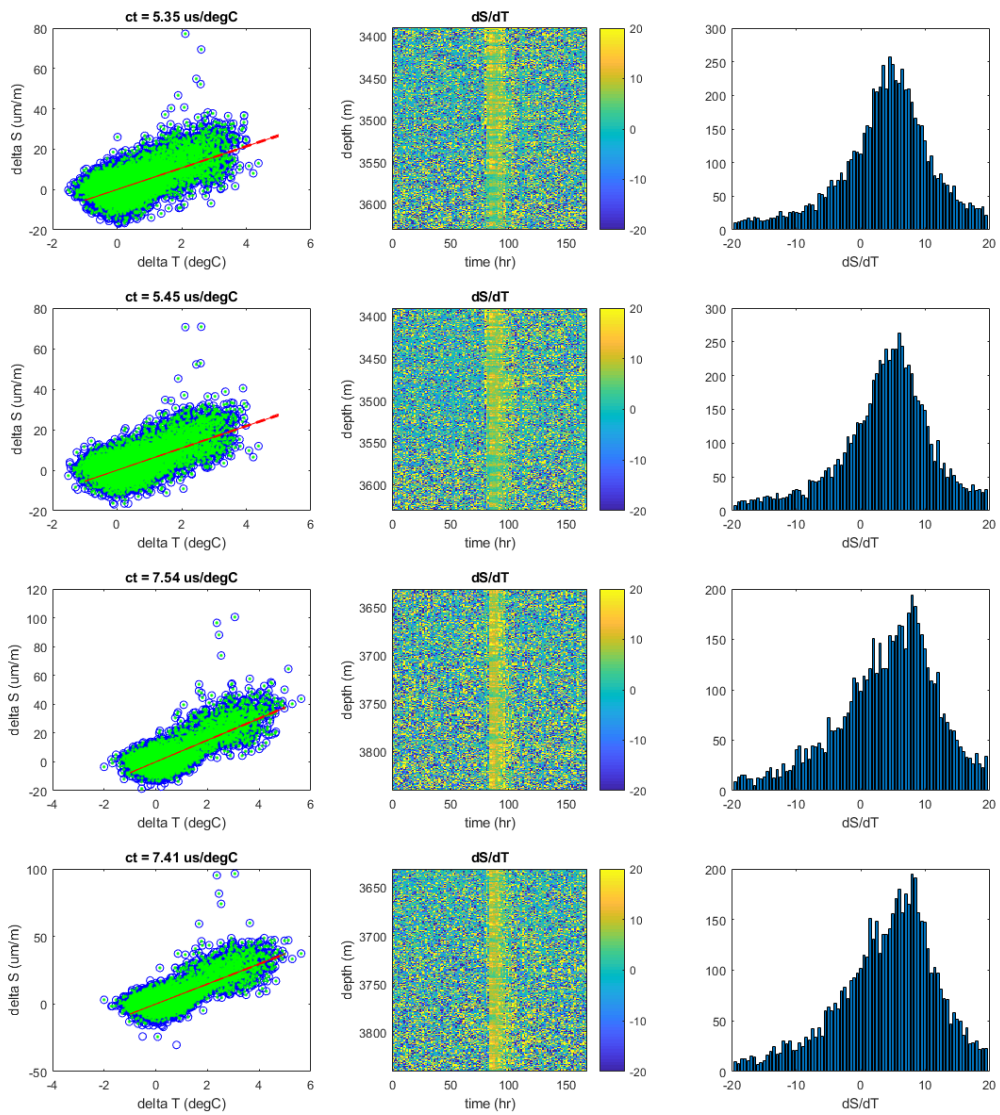
Figure 20: Different visualisations of the temperature and strain change during CTCO. Left column: temperature change (x-axis) and strain change (y-axis) data from all DSS channels. Middle colum: strain change divided by temperature change, as a function of time and depth, during the CTCO. The ratio increases to 5-8μm/m/°C. Right column: histograms of delta strain divided by delta temperature.
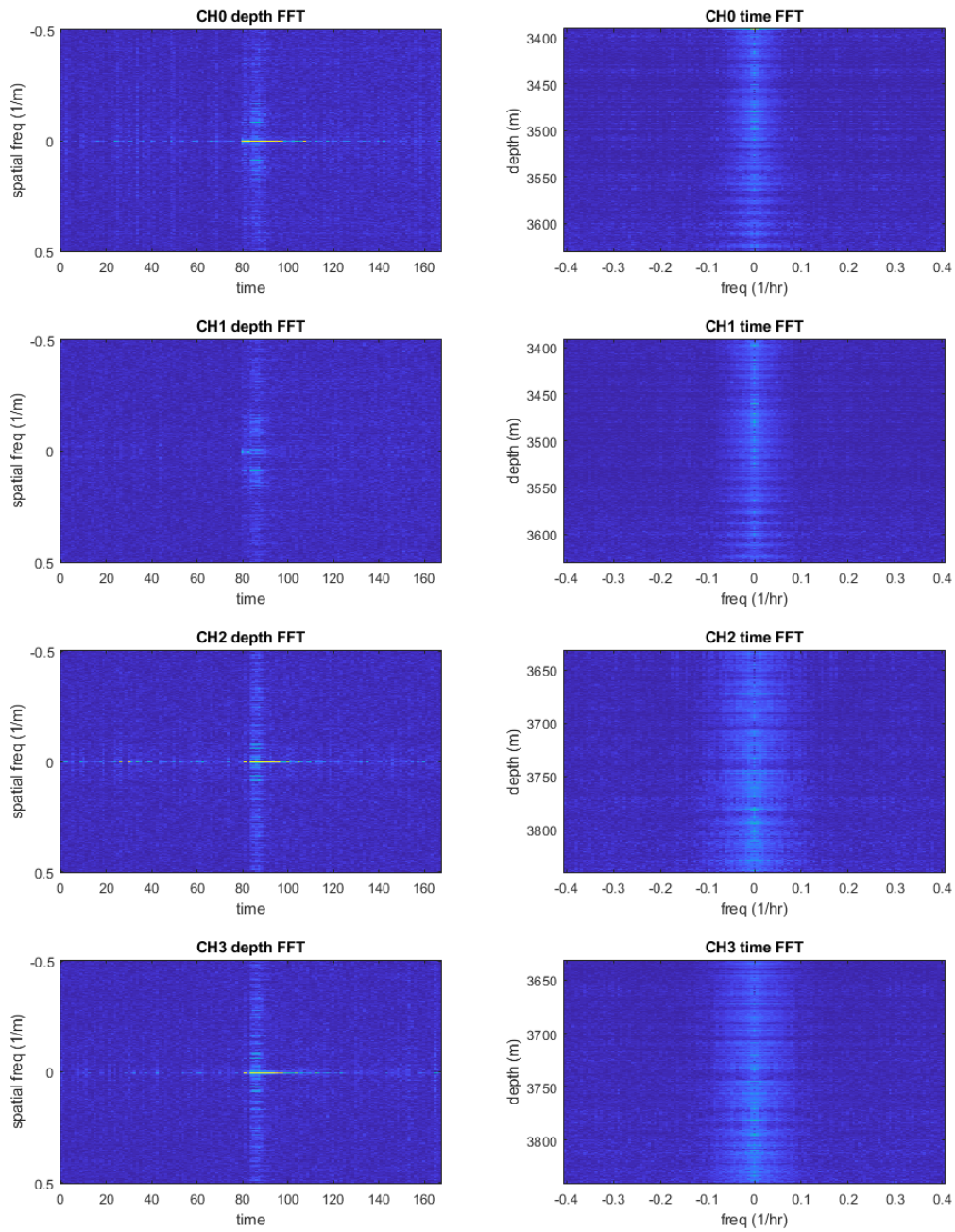
Figure 21: Fourier transforms of the strain data in space (left column) and in time (right column) for all four DSS channels.
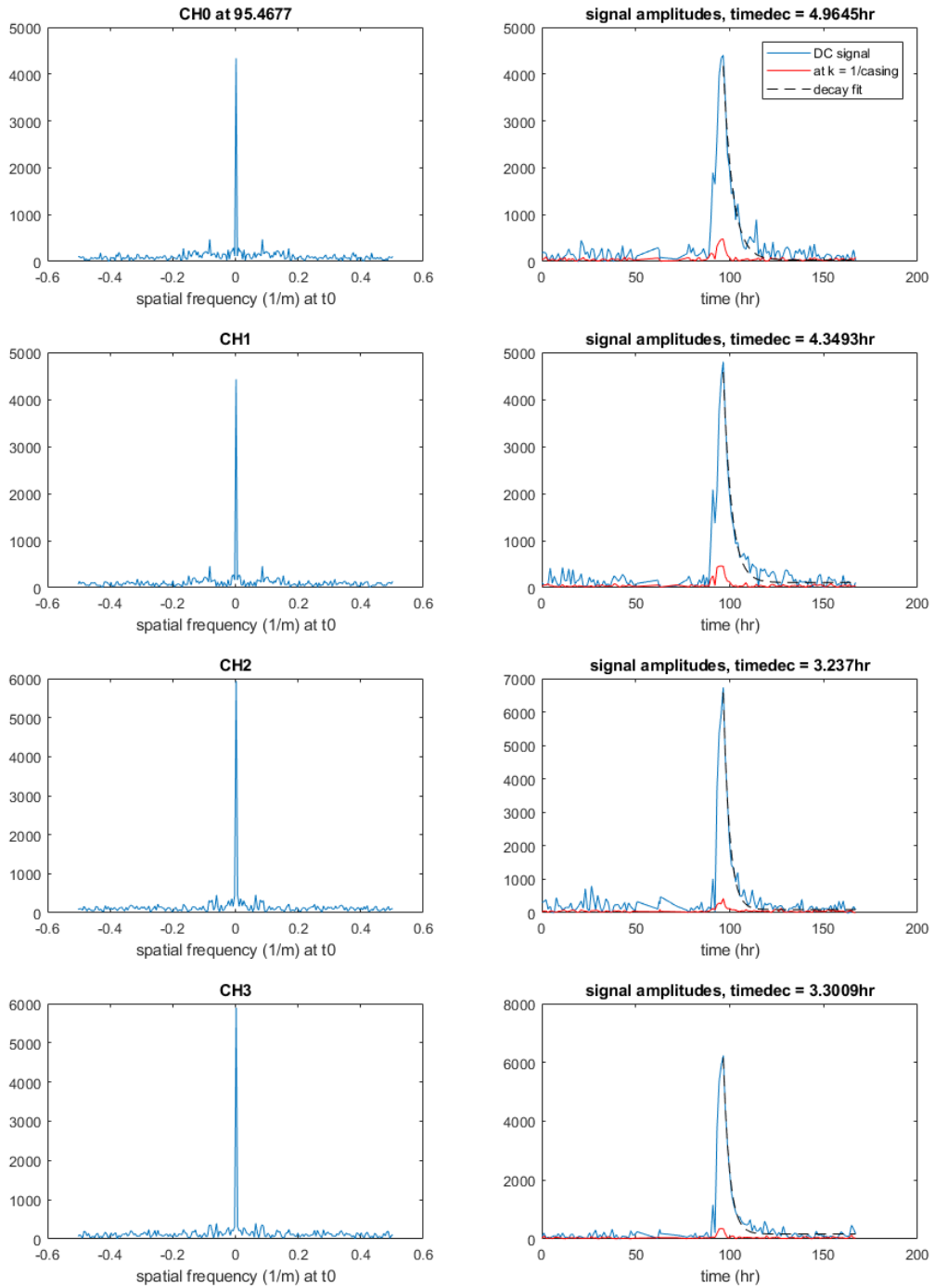
Figure 22: Signal amplitudes from the Fourier transform in space (left column in Figure 21), taken along the spatial frequancy spectrum at the time of maximum signal at 95.5hrs after the start of the particular data set (left column) and taken along the time axis at spatial frequency of 0 (right column). The left column shows the presence of certain spatial frequencies, just under 0.1/m, associated with casing lengths and inter-clamp distance. The right column shows the average decay of the thermal perturbation on the strain signal over time, decaying away in a matter of hours for all DSS channels.
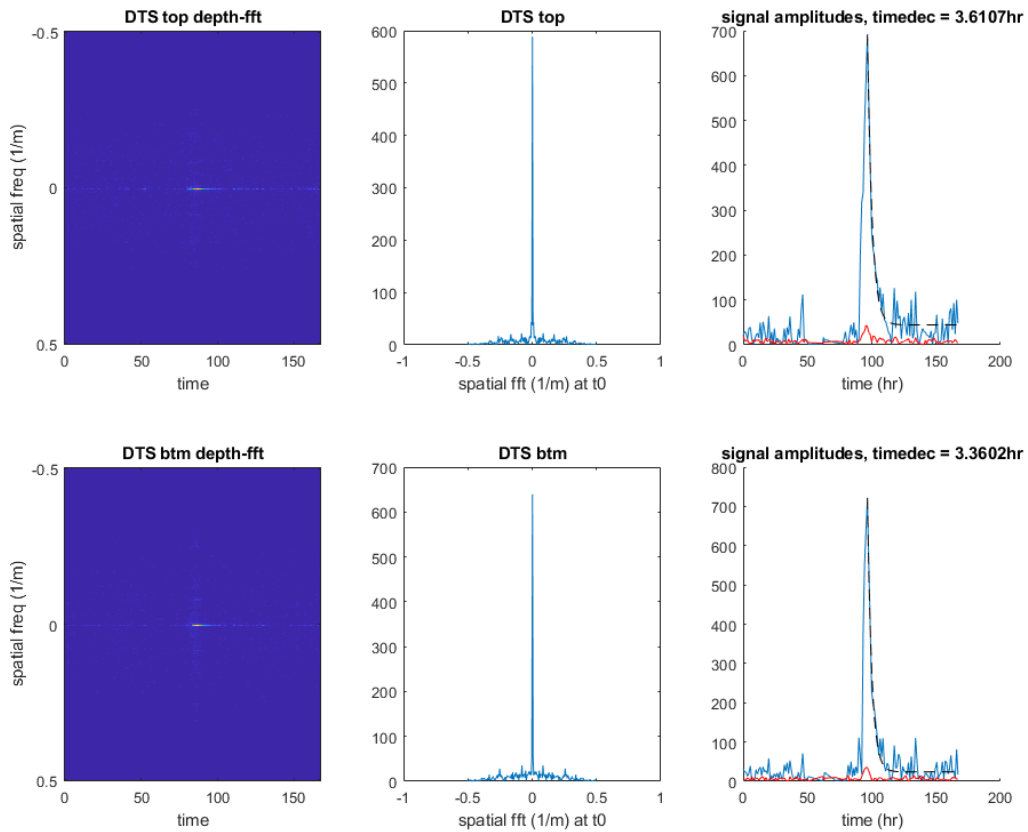
Figure 23: Spatial Fourier transforms of the DTS signal and spectra, similar to those for the strain data from DSS in Figure 21 and Figure 22.

3.4   Thermal analysis from DTS data

The DTS interrogator has been recording temperature data from the Zeerijp well since October 2015, with very little data gaps. Where the DSS only covers an interval of about 500m around the Groningen reservoir, the DTS cable covers the full well, from the well head to well TD. As the DSS cable is sensitive to temperature changes, it is important to understand the sensitivity and stability of the DTS signals.

Figure 24 shows the standard deviation in measured temperatures for each depth in the DTS installation in the Zeerijp-3A well. The standard deviation is shown for two different time intervals; June-July 2017, which was a normal recording period, and September-November 2017, which includes thermal disturbance from the CTCO operations.

One can see that across the well, the temperature recordings have similar stability apart from the shallowest part of the well, down to about 800m, where the impact of the CTCO is most apparent. The standard deviation goes up in this case, measured over a long time interval, to about 1 $^{\circ}$C (obviously the standard deviation will be higher when determined over shorter time periods around the CTCO operations).

There is a gradual increase in the standard deviation from about 800m to the reservoir section. The increase is not due to an increase in noise but is a result of the increasing temperatures with depth. This is visible when normalising the standard deviations by the average temperature at each depth,

as done in the two traces on the right in Figure 24. The standard deviation increases slightly from the near-overburden to the reservoir (DSS section) due to the splices of the fibres at that point.

The standard deviation, measured over 1000s of DTS traces, is about 0.4 °C in the reservoir section. The thermal correction factor for the DSS cable is about 6micro-strain/°C, meaning that the added noise on the strain would be on the order of 2.5micro-strain when the temperature corrections are applied. As the additional noise from corrections is of the same magnitude of even higher than the noise from the DSS measurement itself (see Section 3.5), combined with the belief that the real downhole temperatures are stable to less than 0.4 °C, the thermal corrections are not applied to the DSS data for the Zeerijp-3A well. The corrections will be left out until, of course, there is reason to believe that there are significant thermal fluctuations in the well.

The temperature curves from DTS, averaged over the same time intervals of June-July 2017 and September-November 2017 have been converted to a thermal gradient in Figure 25. Spikes at regular intervals of around 10m can be seen at the shallower depths, around 500m, suggesting that the conductivity of the casing plays a dominant role here in the temperature of the well. Similar features show up on the standard deviations in Figure 24.

A good correlation between the gradient and the gamma ray is observed in some parts, especially the shallow sections of the Zechstein, where high gamma ray values coincide with high thermal gradients (low conductive formations). The Zechstein halite salts (ZEZ2H) have the lowest thermal gradient (highest thermal conductivity). Interesting to see is a slow reduction of the thermal gradient with depth throughout the Slochteren reservoir. The highest thermal gradient in the Slochteren is in the gas bearing part, with the highest porosity sandstones.

These data can be refined and used in the future for more detailed quantification of thermal properties of the different rocks that are intersected by the Zeerijp-3A well.

The continuous monitoring of the temperatures allows for an estimate of thermal gradients and, if heat flux is known, estimates of the thermal conductivity of the different rock formations. Unlike temperature data acquired by wireline, these fibres have been in the ground for years and had more than sufficient time to reach thermal equilibrium with the well bore and the formation, resulting in a better representation of the actual downhole temperatures. Data from wireline operations shows differences of several to 10s of °C between up and down passes. An example of how the temperature measurements from different wireline runs compare to one another and to the DTS measurement is shown in Figure 26. Differences of 1 – 2 °C are quite common between different runs in the same open hole section, and as much as a 15 °C difference can be seen in the overlap between open hole and cased hole runs in the same section, and similar offsets between open hole logs acquired in different open hole segments (e.g. the joint between 8.5in and 12in section). Note that especially the sonic runs in Zeerijp were logged at relatively slow logging speeds (around 1m/min) as full wavelength and azimuthal sonic data was being acquired. Much lower logging speed (to allow for a longer thermal equilibration throughout the logging) are not common and often not possible with the wireline equipment.

Also, important to note is the more or less constant thermal gradient as observed by the wireline data. The thermal gradient there appears dominated by the well fluid as it does not show any correlation to other formation logs, unlike the DTS data.
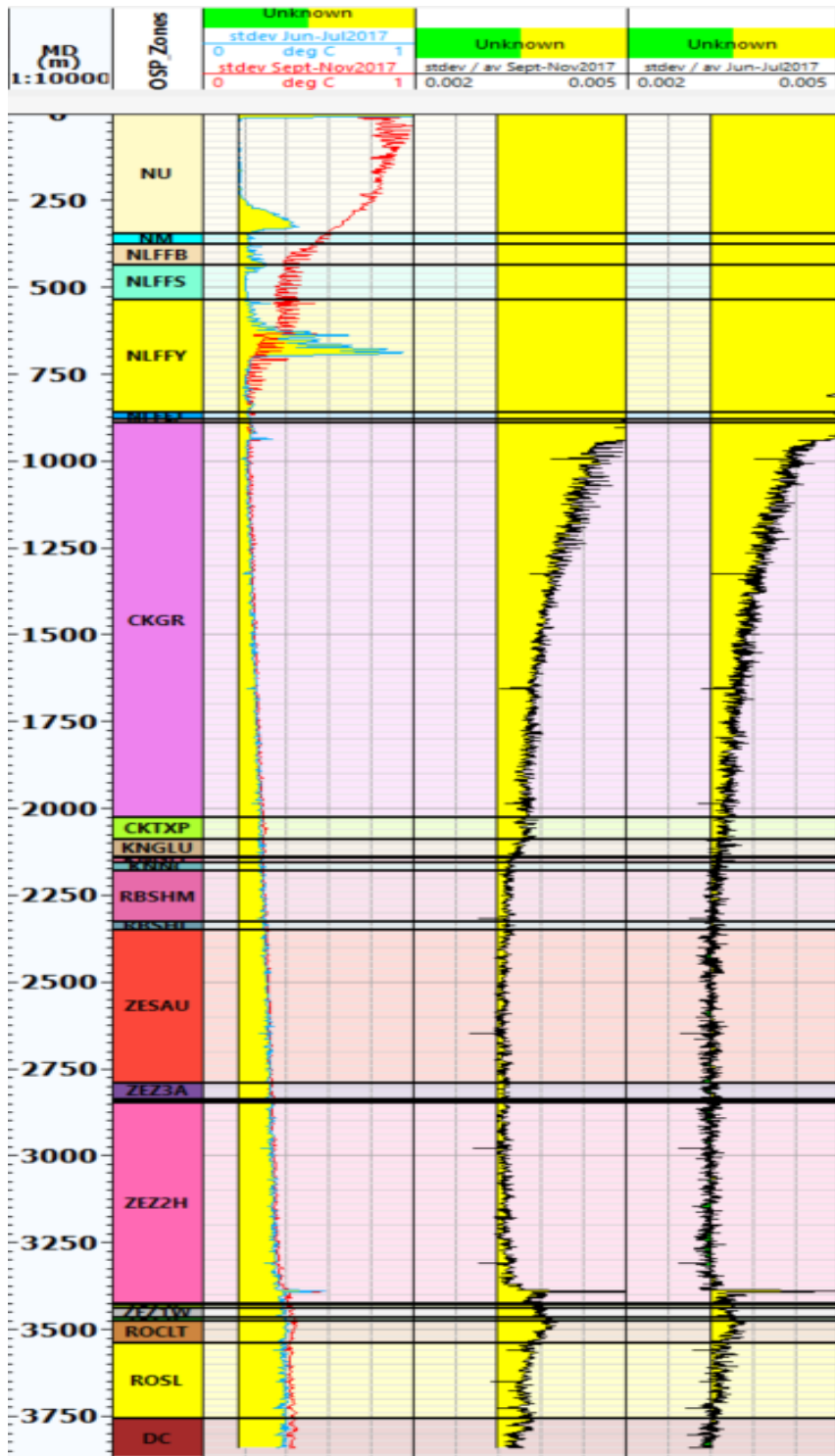
Figure 24: Spread in recored temperatures, through the standard deviation, across the full well interval. The left track shows the standard deviation for two time intervals. These standard deviations have been normalised to the mean temperature for each depth at the two traks on the right.
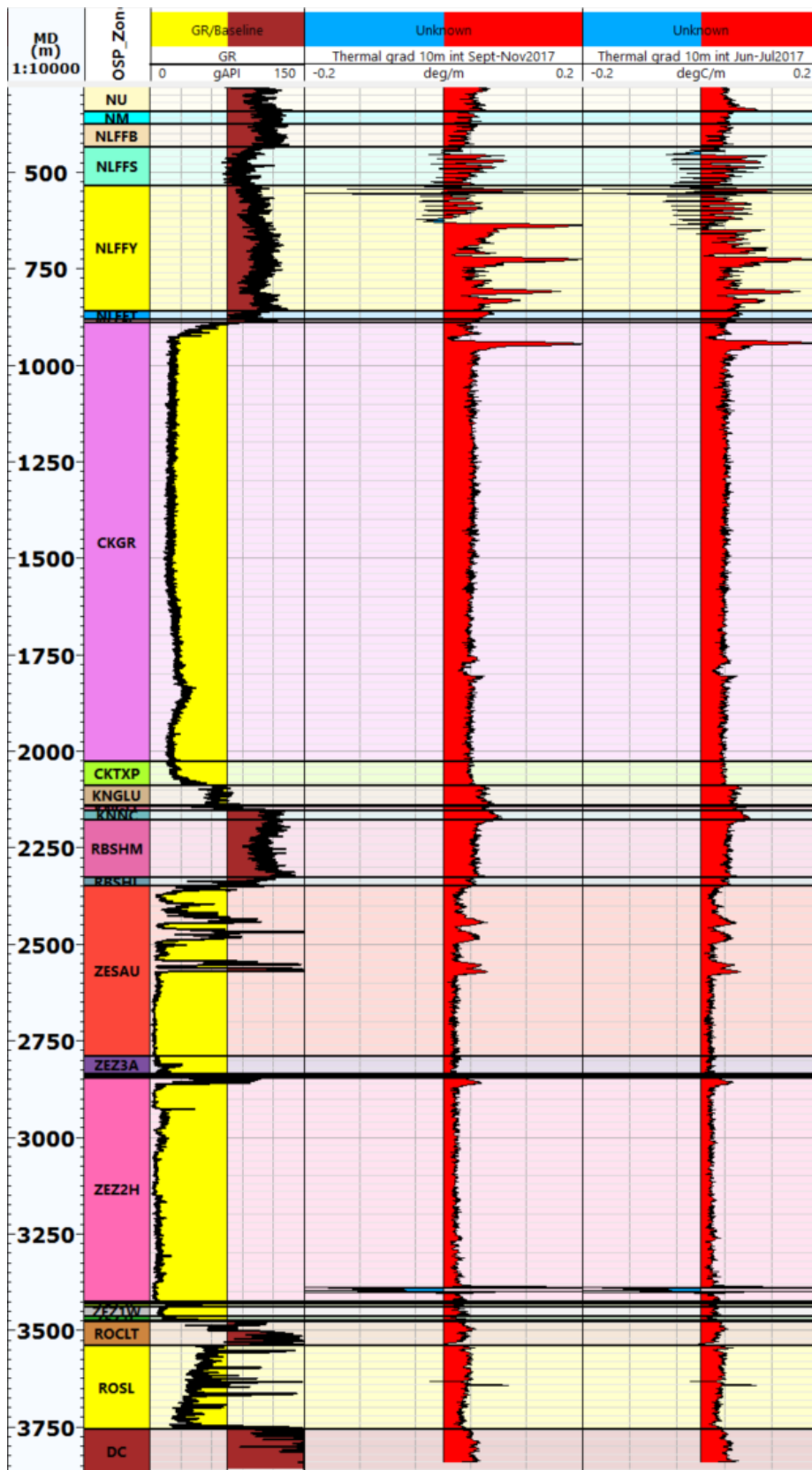
Figure 25: Thermal gradients, determined over 10m intervals from the DTS data. Thermal gradient has been determined for two separate time intervals; September-November 2017 and June-July 2017.
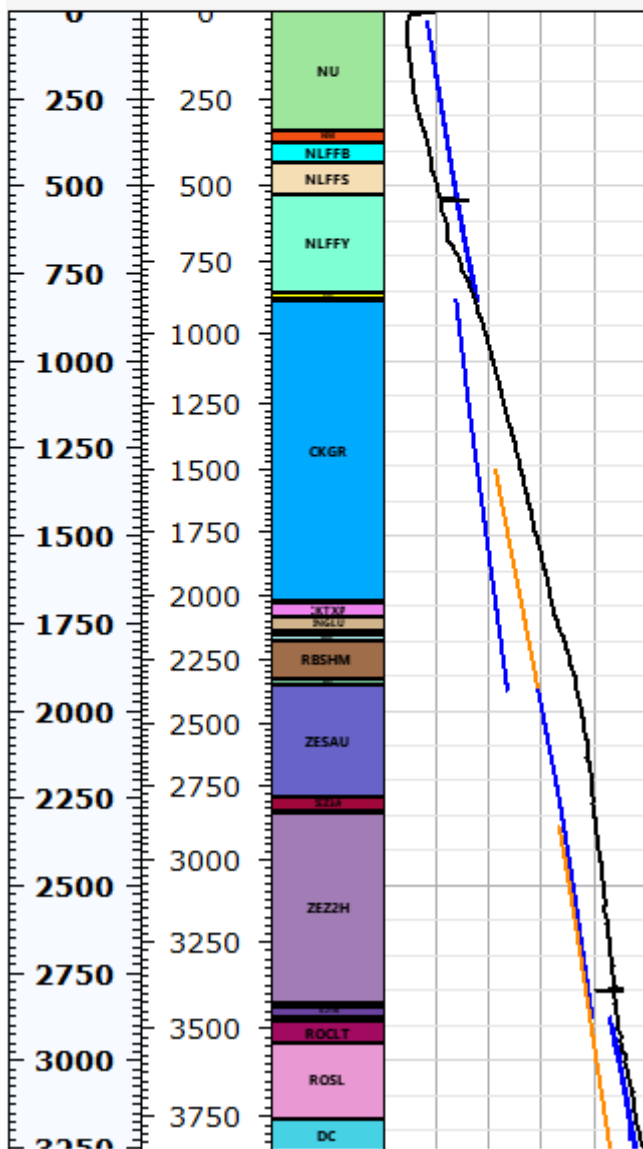
Figure 26: Temperature measurements from DTS (black) and from several wireline passes, both open hole (orange) and cased hole (blue) data are shown. Hole sizes are indicated in the curve names.

3.5   Strain uncertainty for different interrogator units

In February 2017, the beta-unit interrogator for the DSS (labelled DDxS0) was replaced by a production unit (labelled DDxS1). Data recordings from DDxS0 stopped on 15 February 2017, data recordings from DDxS1 started on 18 February 2017. The changeout was relatively quick, leaving a data gap of only 2 days. Assuming the actual strain build-up over this time is negligible, the readings of the two interrogators should theoretically be identical, giving an opportunity to compare the two units in terms of their consistency of strain data.
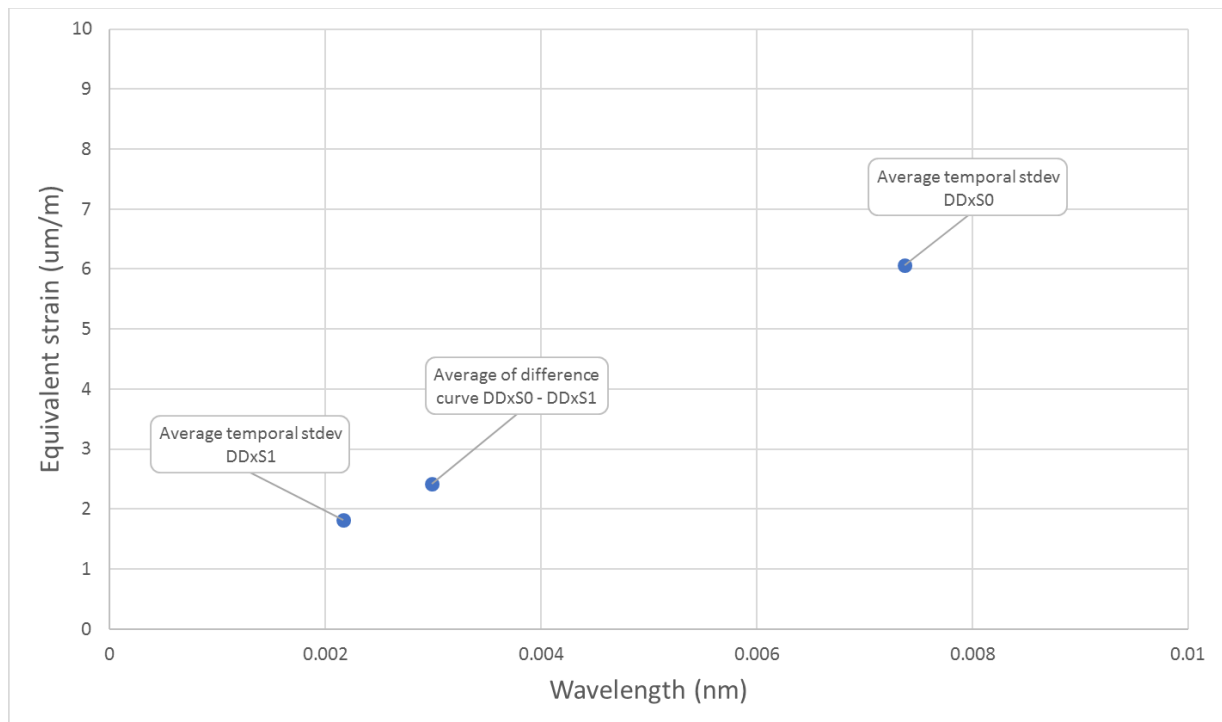

Figure 27: Measurement uncertainty for the two DSS interrogators (beta unit; DDxS0, and production unit; DDxS1), and the average difference of recorded wavelength per grating. All data plotted in terms of wavelength as well as equivalent strain.

The production unit (DDxS1) has lower scatter in the measured wavelengths than the beta unit (DDxS0), reducing the average uncertainty (using the standard deviation here as a measure of uncertainty) from 6μm/m to 2μm/m, as an average per grating taken over 10 traces, see Figure 27.

There is some difference in the interpretation of the absolute wavelength of each grating by the two interrogators. This can occasionally give high apparent strains when comparing readings from one interrogator with the other (when using a common baseline reading), in excess of 30μm/m occasionally for individual gratings. On average, however, the difference is small as evidenced in the figure above: the value labelled 'average of difference curve' shows that the average apparent strain, resulting from switching from one interrogator to the other, is less than 3μm/m.

4 Frequency analysis

The high resolution in both space and time of the strain and temperature data from the fibre optics installation in Zeerijp-3A allows for analysis of the existence of certain frequencies within the data. A temporal frequency analysis could reveal the existence of seasonal fluctuations (either direct from seasonal changes in the environment, or indirect from seasonal fluctuations in the production from the Groningen field) or tidal frequencies, while a spatial frequency analysis can reveal sensitivity of the measurement system to certain length scales, for example correlations of the strain data to casing lengths.

Here, we first present the frequency analysis of the temperature data (obtained by DTS) and the observed features, followed by a similar discussion of the strain data (obtained by DSS).

4.1 Temperature

The frequency analysis of the temperature data is split into the overburden section, there were thermal fluctuations that are most obvious in the data, and the reservoir section, where the existence of any frequencies in temperature changes would be of interest for the strain analysis.

4.1.1 Overburden (shallowest section)

The recorded temperatures for the first 120m of the Zeerijp-3A well are shown in Figure 28. A few features are worth noting here:

A gradual decrease in temperature across this interval from time-zero is also visible, which is the restabilisation of the temperature after it had heated up during the drilling process. After the first 400 days or so, the temperature appears to have settled.

A bright line appears around 750days after the start of measurement. The line is not a printing error but is the increase of temperature caused by the CTCO operations. As discussed in Section 3.3, the effect of the operations on the temperature lasted only several hours.

Most striking is the fluctuation in temperatures for the shallowest 10m or so in the data. As these have a periodicity of somewhere between 300 and 400 days, these would likely be the seasonal fluctuation in temperature.

These seasonal effects are studied in more detail by looking at the Fourier transforms of these temperatures. Some of the resulting frequency spectra are shown in Figure 30. The top graph here shows the temperature change at several different depths over time, while their frequency spectra (absolute values) are shown in the bottom two graphs. Not only a clear amplitude is visible at the 1/year frequency, but also at the 1/day for these shallowest recordings. When looking at deeper depths, both the 1/year and 1/day frequencies disappear. Because of the clear coincidence with the daily and annual cycles in ambient temperatures, these fluctuations of the temperature in the DTS data are caused by these daily/seasonal temperature changes.

The amplitude of these 1/day and 1/year frequencies are plotted together with their phase in Figure 31, to reveal the decay of these signals with depth. The daily temperature fluctuations penetrate down to a depth of about 10m, while the annual changes in temperature reach a little deeper to about 15m, after which all signal seems to have disappeared. This means that thermal fluctuations caused by daily changes in temperature are not expected to have any effect at the reservoir level. If any frequencies should be visible on the strain data, then these would most likely be real periodic strain signals rather than be anomalies caused by diurnal or seasonal thermal fluctuations.

Interesting to note as well is the gradual phase change with depth seen in Figure 31, indicating that there is a gradual time lag in temperature response building up with depth. These shifts arise from the temperature perturbation taking time to penetrate through the shallow soil. The time shifts are also visible in the temperature data of Figure 28 for the annual frequency. Figure 32 shows the temperature data for several depth across a shorter time frame, where the phase change (time lag) with depth is also apparent on the daily temperature fluctuation.

A phase delay of up to 70deg is seen on the annual thermal disturbance at 15m depth, which corresponds to a delay of about two months. At a depth of 4m, the daily thermal disturbance has a delay of 70deg, or about 1/5 of a day, also visible in a zoom-in of the temperature fluctuations at a few depths in Figure 32. The phase analysis suggests the delay of the daily temperature fluctuations goes even as far as a full day of delay at a depth of 15m, however there is very little signal there.
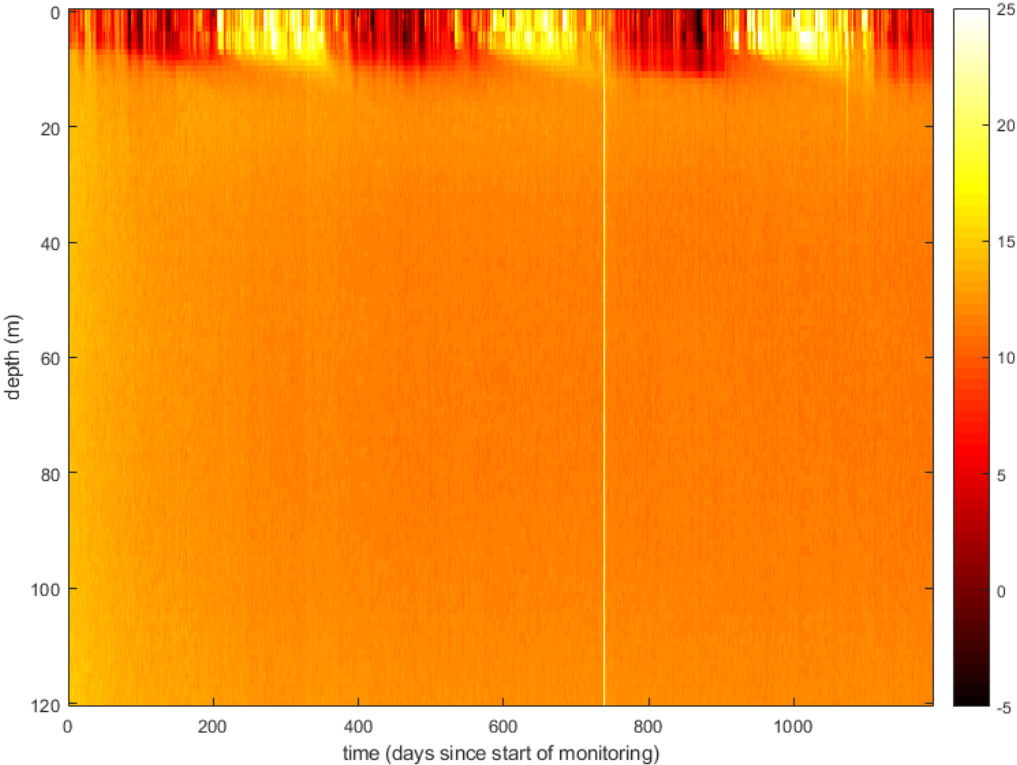

Figure 28: Change in temperature for the first 120m of the Zeerijp-3A well, over the first (approximately) 1200 days of monitoring.
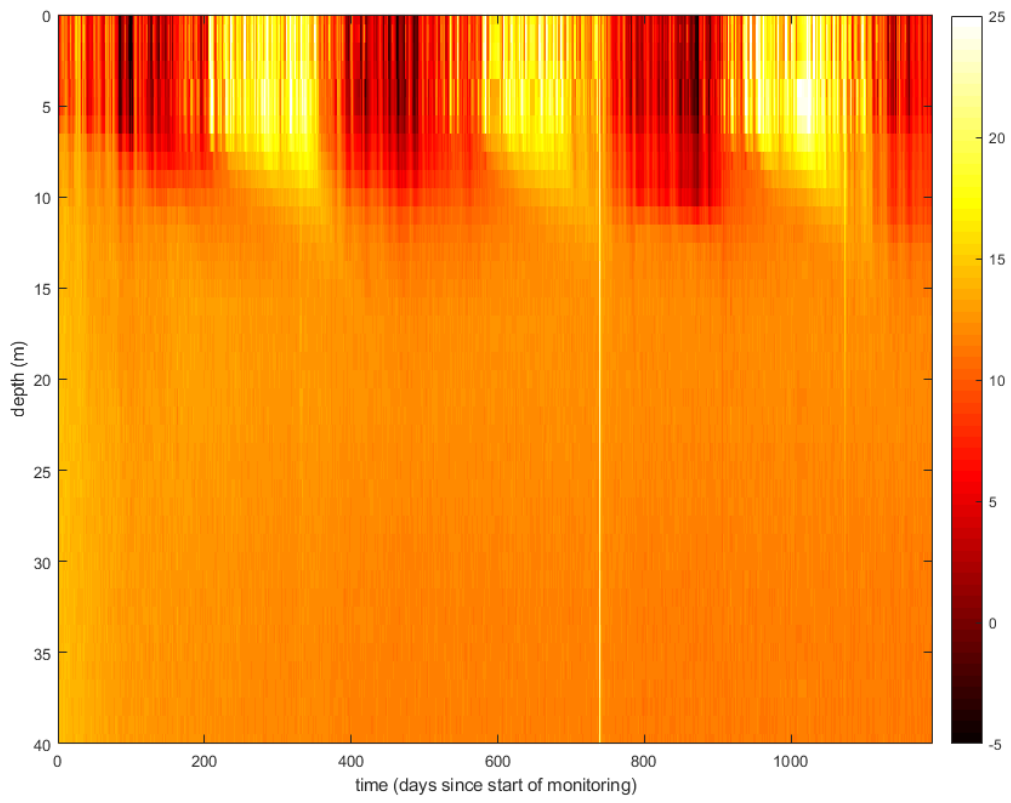
Figure 29: Change in temperature for the first 40m of the Zeerijp-3A well, over the first (approximately) 1200 days of monitoring.
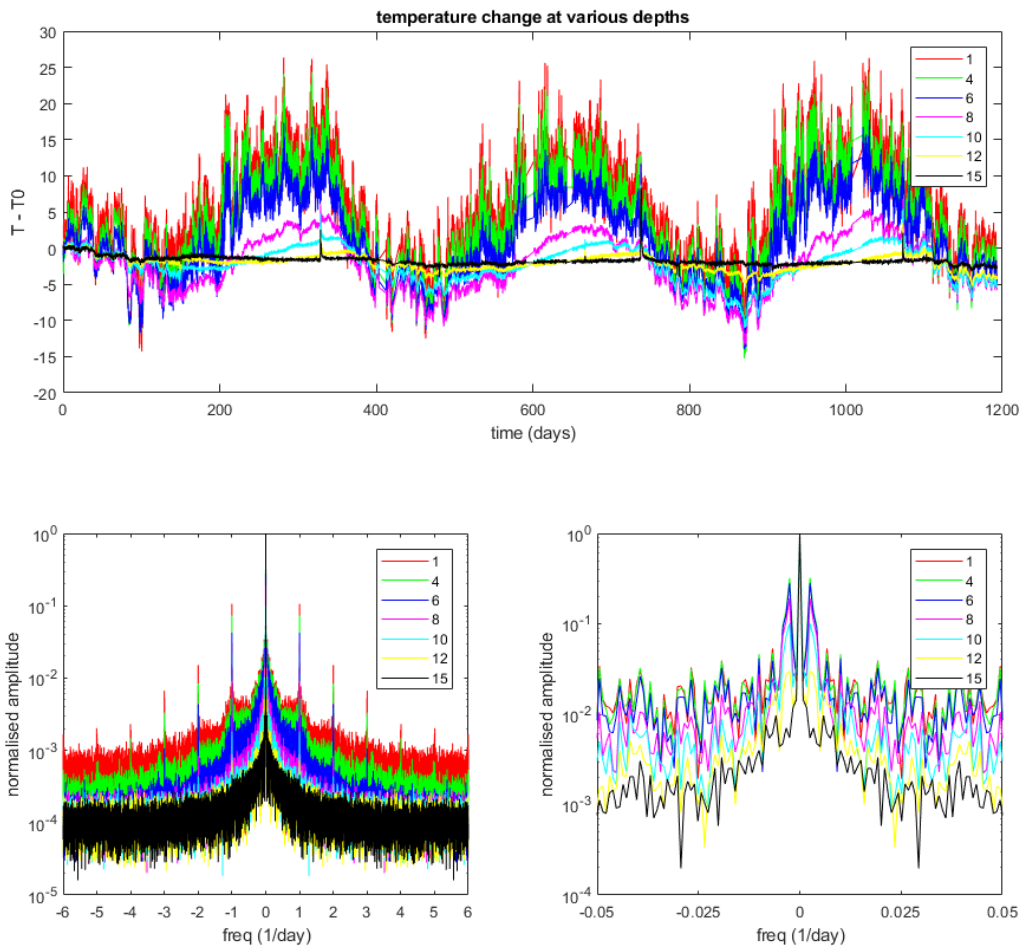
Figure 30: Figure on the top shows the change in temperature (in ^oC) at seven different depths (see legend for the depth in mAHORT) over time (top). Bottom figures show the (absolute value of) the Fourier transform of these temperature curves, for a wider frequency range on the left and a zoom-in on the right.
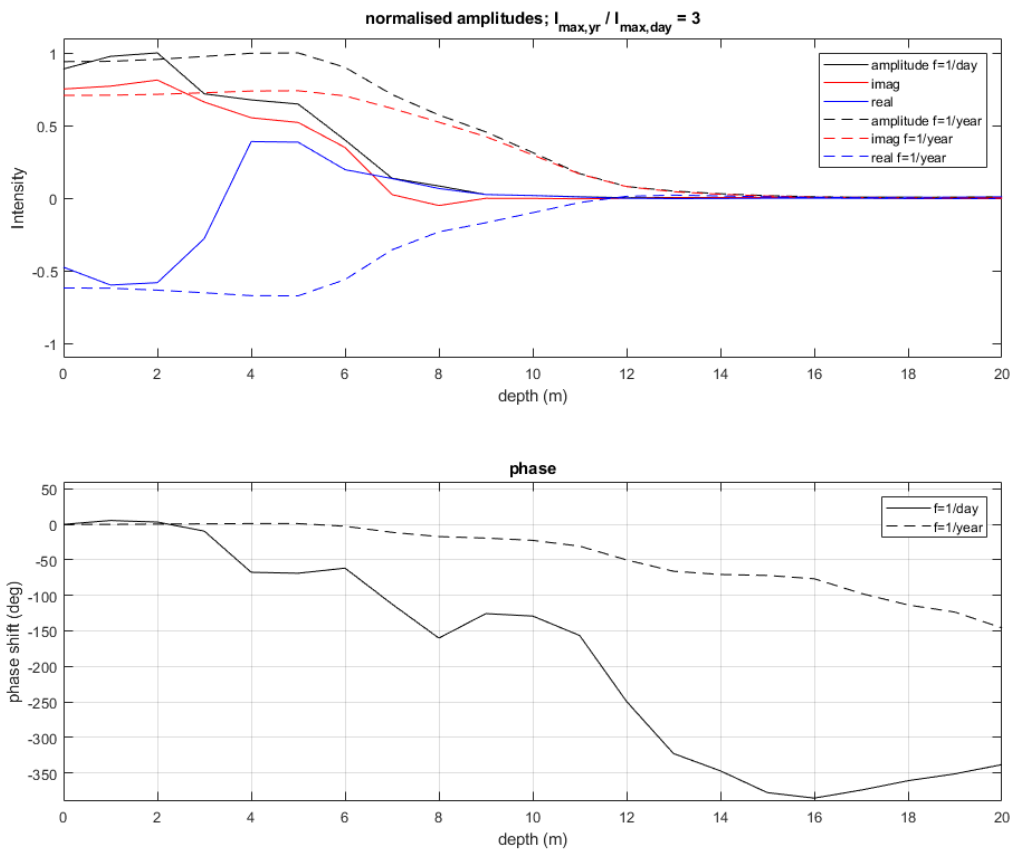
Figure 31: Fourier intensities (absolute, real and imaginary components) for a frequency of 1/day and 1/year, as a function of depth along the well (top). The phase change (change in phase between real and imaginary component) of the two components is also shown as a function of depth (bottom).
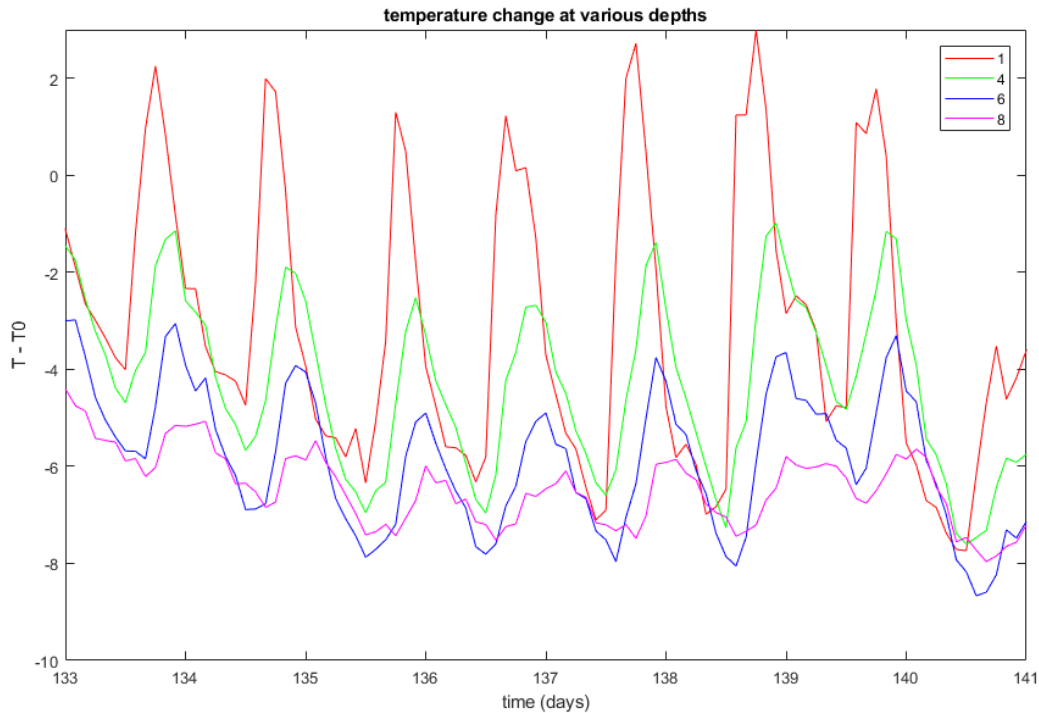
Figure 32: Detailed view of the change in temperature at various depths (depths indicated in the legend in mAHORT), showing the change in phase (time delay in temperature response to the ambient) with increasing depth.

Zoom in at one part of the time scale, also displaying a small but noticeable time delay of the daily thermal fluctuations with depth; about 1/5 of a day in the first 4m, and 2/5 of a day (10hrs) at 8m depth.

4.1.2   Reservoir section

The temperature change across the DSS interval is shown in Figure 33. The first trace is 12 October 2015, last trace is 17 Jan 2019. Unlike the shallow data, no clear annual fluctuations are visible. The geophones are visible during times when they are operational, at a regular spatial frequency (spaced 40m apart).

The temporal frequency spectrum of the (average) temperature change across the reservoir is plotted in Figure 34. The change in temperature (top graph of Figure 34) shows the initial jitter in temperatures during the first 200-300 days or so, caused by instability in the temperature in the data room [1]. The spike in temperature around 750 days is caused by the CTCO. The spectrum (bottom of Figure 34) does not show any significant amplitude at frequencies of 1/day, 1/year above the background.
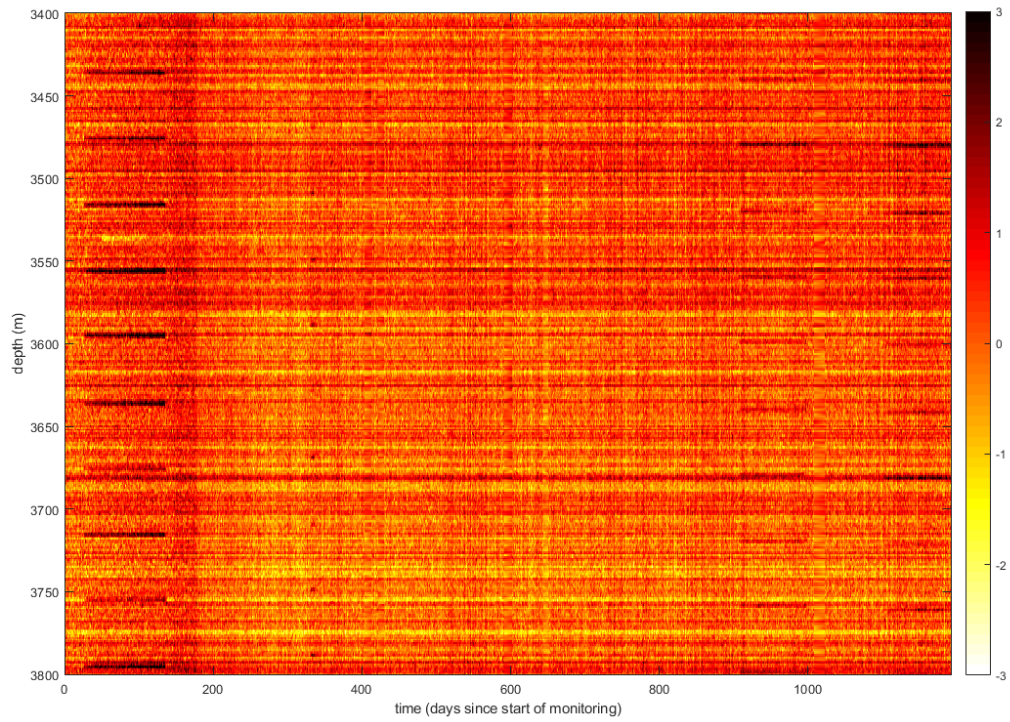
Figure 33: Change in temperature across the reservoir section, for the same time interval as Figure 28. The imprint of geophones is visible during certain time intervals as features with typically >3 °C temperature increase. No clear seasonal fluctuations visible.
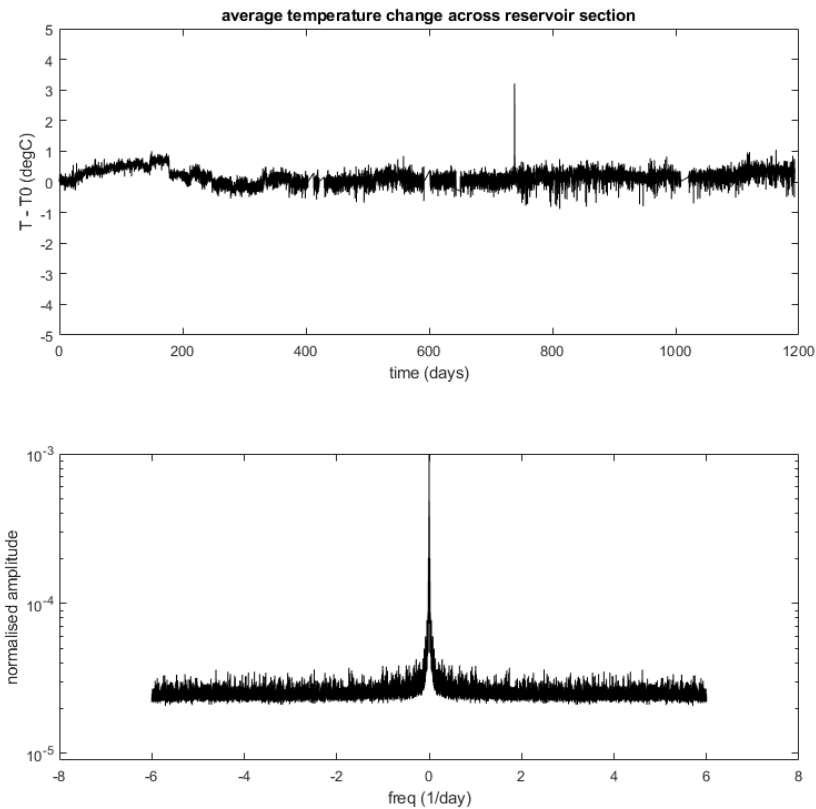
Figure 34: Average temperature change across the reservoir section (top) and its Fourier transform (bottom). No significant intensity is observed around the 1/day or 1/year frequencies, unlike the temperature response for the shallow section of the well.

The spatial spectra of the temperature data over the reservoir section are shown in Figure 35, for data during times when the geophones were not operational and for times when they were operational. When geophones are off, there is no significant frequency amplitude observed above the background; temperature readings are likely not affected by the casing or clamps or any other repetitive components in the well. When the geophones are turned on, a clear comb structure appears on the spectrum, having a peak to peak separation of 0.025/m, corresponding to the 40m offset between the geophones.

Figure 36 shows amplitudes above (or below) local background signal and phase shift at three different spatial frequencies (0.025/m, 0.050/m, 0.075/m). During periods when geophones are operational, these frequencies gain distinct amplitude features that disappear almost immediately once switched off, apart from probably the first geophone epoch that shows a decay over a number of days, and do not leave a permanent imprint on the DTS data. The differences in phase shifts between the different epochs is related to the difference in placement depth of the geophones, which was not always the same. Theoretically, one should be able to derive a shift in units of depth from these phase shifts, however as the actual shift is multiple phases this takes some work in aligning the phases from all different frequency spikes.

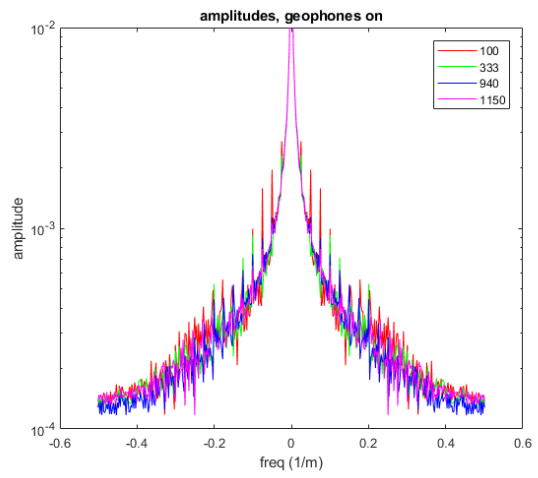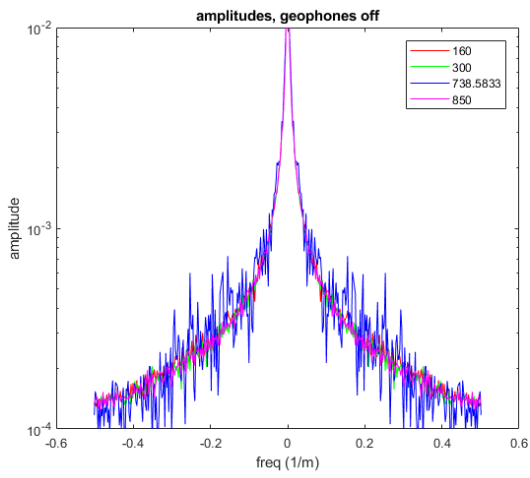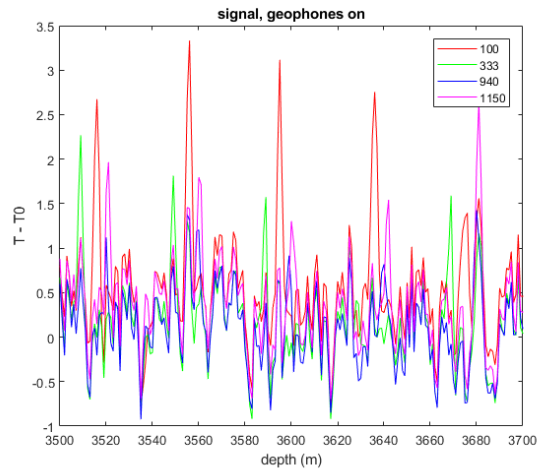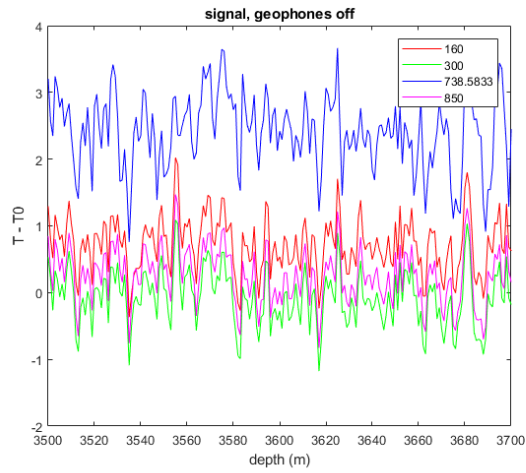*Figure 35: Spatial frequency transforms during periods when geophones were active and inactive. During times when geophones are active, clear comb features appear on the frequency spectrum (bottom right) that are absent in the frequency spectrum for signals when geophones are off (bottom left). Separation between peaks is 0.025/m, corresponding to a 40m interval, which is the separation between the geophones.*
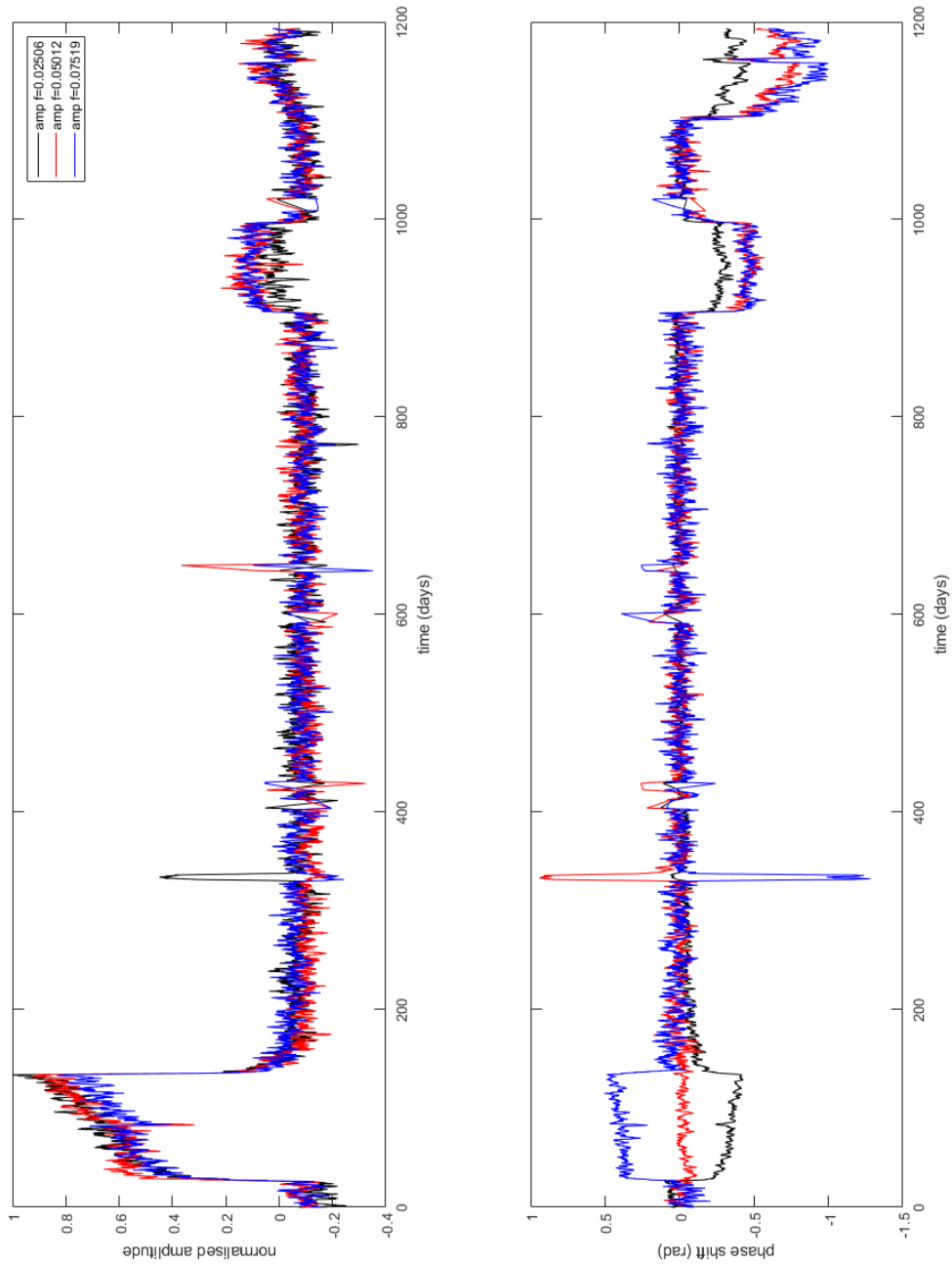
Figure 36: Amplitude and phase over time for three separate spatial frequencies that gain intensity during geophone operations.

4.2 Strain

The reservoir compaction is shown together with its temporal frequency spectrum in Figure 37. Note that the change in the amount of variation of measured values after about 500 days is due to the change in DSS interrogator, resulting in reduced noise levels (see Section 3.5). Fluctuations in strain could arise from the seasonal patterns in production. As the DTS signal did not show any periodic signals (1/day, 1/year) across the reservoir section, it is expected that periodic thermal effects do not influence the strain measurement.

The data was analysed at a 1/day, 1/year but also at lunar frequencies to look for presence of tidal effects on the strain, but none of these have been observed above the background. As there is no periodicity observed at all, it can be concluded that, on the order of microstrains, there is no fluctuation in the strain at the Zeerijp location.

Had the Groningen field (or the Zeerijp location) been in a tidal area, the sensitivity of the DSS system could have allowed for measuring cyclic loading of the reservoir. The cyclic gravitational loading has been observed in the past and used for estimating reservoir properties [10, 11]. With rock compressibility on the order of 10microstrain/bar, a loading gradient of water by 1bar/10m, and a sensitivity on the order of 1microstrain, a tidal change of 1m could already be enough to observe a periodic strain signal.

A discussion of the spatial frequencies in the strain data was presented in Section 3.3, where the frequency component corresponding to a casing length gains intensity during the CTCO operations. These are believed to be induced by the thermal disturbance, which has a larger effect on the strain at the locations of the clamps (of which there is one placed at each casing stand). The intensity at these specific locations in the frequency spectrum is not present during periods of thermal stability (the majority of the data set), suggesting that the strain measurement in general is not sensitive to (and not affected by) the clamps or casing joints, and is measured throughout the cable.
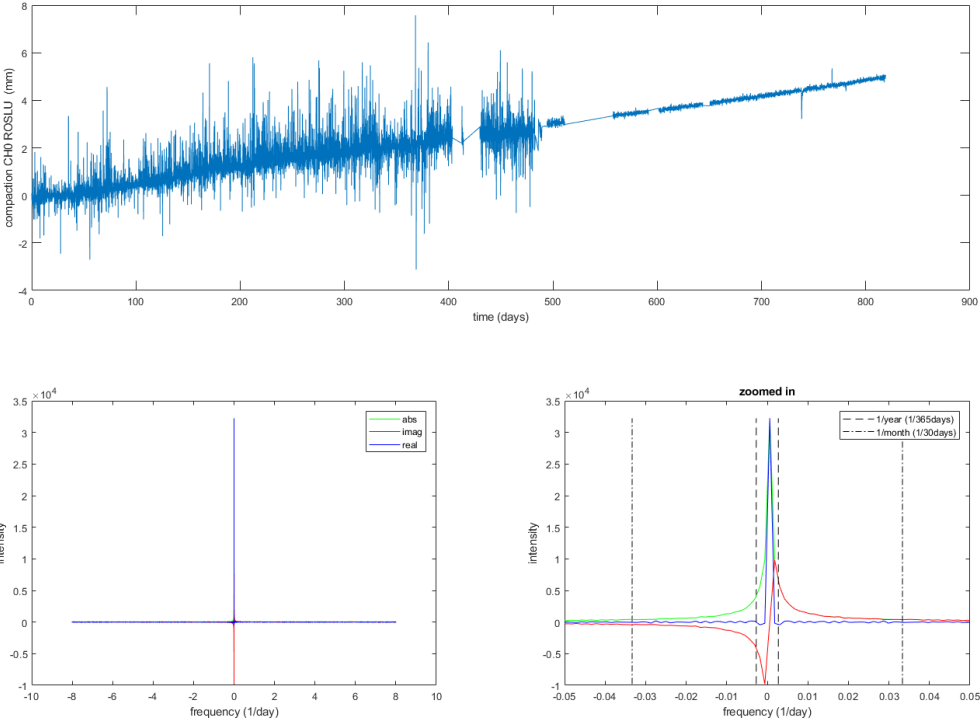

Figure 37: Measured compaction signal across the reservoir (top) and its temporal frequency transforms (bottom figures). No clear intensity peaks observed at frequencies of 1/day, 1/month or 1/year.

5 Correlation of strain data with well logs

The purpose of correlating the strain data with other well log data is two-fold: on one hand, we want to test if any of the other data sources (which are more commonly available across the reservoir compared to the strain data) can be used as a proxy for the strain (or compressibility), and on the other hand we want to see to what extend the strain data is affected by well-specific properties like the well inclination and the cement bond index. A stronger correlation of the strain data with well-specific properties than with reservoir properties might be an indication that the recorded signals are more related to the well itself than to the (far field) reservoir compaction.

The available standard log data are displayed together with the strain data (strain till August 2019) in Figure 38. Just from eye-balling, some logs show correlations with the strain data, for example the sonic and density data both show higher slowness – lower density – higher strain above 3640mAHORT compared to the zone below, thin streaks of lower slowness – higher density – lower strain around the interval 3600mAHORT – 3650mAHORT, and a thicker zone from 3729mAHORT – 3737mAHORT with lower slowness – higher density – lower strain. A more detailed comparison of the data, including core CT scans, in Figure 39 shows the correlation on a smaller scale, where some correlation could be seen in that higher density (lighter values on core CT) show less compressive strain. The qualitative correlations here do not always hold though, as not necessarily every lighter spot or higher density area coincides with lower strain values.
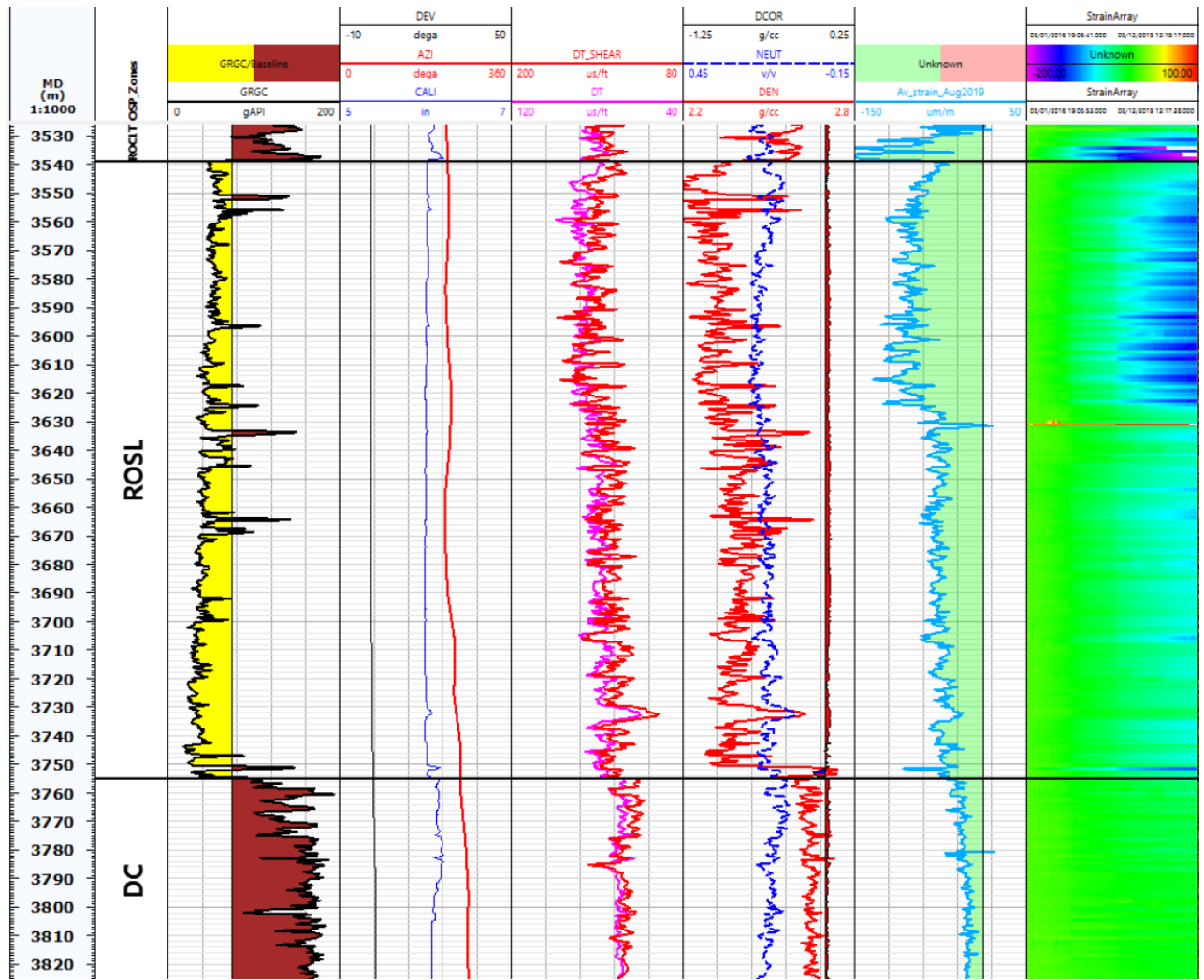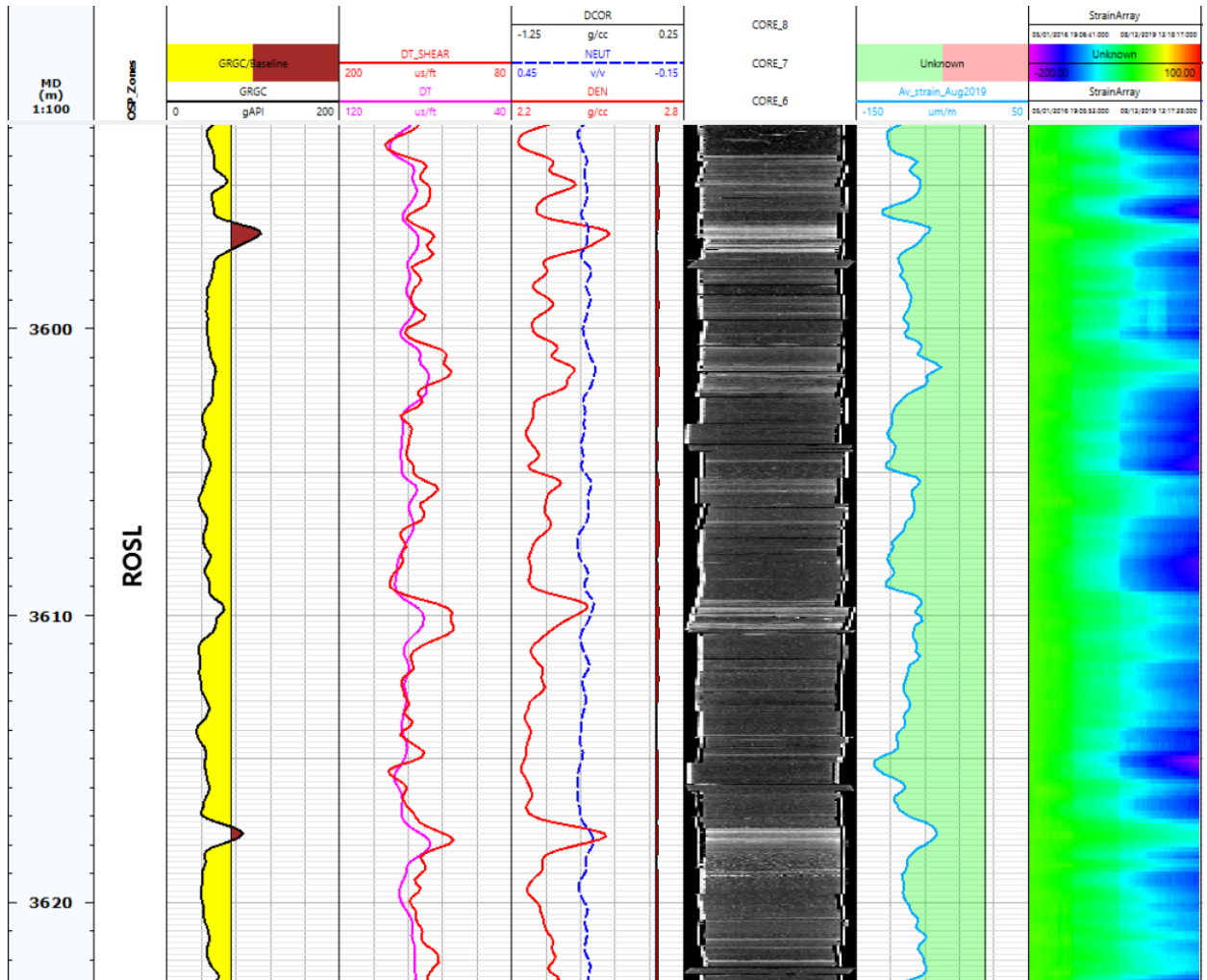
Figure 38: Log data and strain data for Zeerijp-3A.

Figure 39: Log data, core photos and strain data for Zeerijp-3A.

5.1   Linear regression model

To get a more quantitative comparison, we use linear regression analysis to test how well the strain data can be described with other log data. Prior to the testing the strain data was smoothed to remove high spatial frequency components that are not present in any of the log data, i.e. parts of the signal that can never be explained by any of the data from wireline logs.

The Zeerijp-3A wireline logs included in the comparison are:

- Measured depth (and True vertical depth)
- Well azimuth
- Well deviation
- Borehole calliper
- Cement bond index (inferred from CBL data)
- Gamma ray
- Density
- Density correction
- Compressional sonic
- Shear sonic
- Neutron
- Resistivity (deep, medium and shallow curves were included separately)
- Porosity (as interpreted from the wireline logs)
- Dynamic compressibility (as interpreted from the wireline logs)

The logarithm of the three resistivity curves was used since these data typically span several decades. Future additions could be the grey scale values from the core CT scans, which are a measure of density and mineralogy, scratch test data from the core, and borehole image derived properties.

What is missing in the list is a parameter that is sensitive to the pressure depletion. As a result, the strain is only compared to static properties taken at one moment in time, and any effects of varying depletion cannot be captured or explained by any of the input data used here.

We test the goodness of fit for a linear regression model for each of the log data:

$$\begin{bmatrix} y_1 \\ \dots \\ y_n \end{bmatrix} = \begin{bmatrix} 1 & x_1 \\ \dots & \dots \\ 1 & x_n \end{bmatrix} \begin{bmatrix} a \\ b \end{bmatrix}$$

Here, y_1 to y_n represent the n-data points along the well interval in the strain data set, while x_1 to x_n are the measured values at the corresponding depths for the tested property. The equation is solved for a and b; the offset and slope of the linear regression.

As a goodness of fit and correlation, the residual standard error and the R2 values are calculated for each parameter individually, and for the full combination of all 16 data sources. These are listed in Table 4. These values are when testing the strain measured between March 2016 and August 2017 over the depth interval 3540mAHORT to 3750mAHORT. The test was repeated for strain data acquired over a 4-year time period. The obtained offset and slope are listed for each parameter in Table 5, which can be used to generate the estimate for the strain, as observed during 4 years of surveying in Zeerijp-3A, from the respective logs.

The high residual standard error and low R^2 values for well-related properties (azimuth, deviation, calliper, cement bond index, density correction) when comparing to the reservoir rock related

properties, indicates that the well bore and equipment itself have little impact on the measured strain data, and that the measured strain is primarily governed by the reservoir itself.

What is interesting to note is that the measured depth can describe the strain data using a linear translation to a comparable level as a linear transform of the density or neutron data, and better than what can be achieved by the gamma ray.

The sonic slowness, both compressional and shear, are best at describing the strain data by a linear function. Surprisingly, a linear function of the sonic data can describe the measured strain better than a linear function of the (log-derived) porosity and even the dynamic compressibility can; the former is often used as a proxy for reservoir compressibility and the latter is a theoretical representation of the compressibility, and both use more input data (use more information) than a single sonic curve does.

These observations remain valid when testing the linear regression to the strain data that is acquired over a longer (4-year) time period.

Table 4: Residual standard error and R^2 values for linear regression of available log data with the strain data, for two time periods (18 months of strain data and 4 years of strain data).

Parameter	Residual standard error (μm/m) (18 months of strain data)	R^2 (18 months of strain data)	Residual standard error (μm/m) (4 years of strain data)	R^2 (4 years of strain data)
Measured depth	9.19	0.23	14.49	0.48
Well azimuth	9.87	0.12	18.55	0.15
Well deviation	9.76	0.14	17.83	0.22
Borehole calliper	10.32	0.03	19.10	0.10
Cement bond index	10.49	0.00	20.14	0.00
Gamma ray	10.36	0.03	19.10	0.10
Density	9.10	0.25	16.48	0.33
Density correction	10.50	0.00	20.15	0.00
Compressional slowness	7.33	0.51	10.70	0.72
Shear slowness	7.06	0.55	10.86	0.71
Neutron	9.20	0.23	17.13	0.28
Deep resistivity	10.46	0.01	20.14	0.00
Medium resistivity	10.44	0.01	20.15	0.00
Shallow resistivity	10.45	0.01	20.14	0.00
Dynamic compressibility	7.57	0.48	11.55	0.67
Porosity	8.11	0.40	14.67	0.47
Linear combination of all parameters	6.50	0.62	8.49	0.82

Table 5: Estimated offset and slope for linear regression models based on a single variable.

Parameter	a (μm/m)	b (varying units)
Measured depth (mAHORT)	-903.23	0.23
Well azimuth (deg)	-281.22	0.94
Well deviation (deg)	-118.98	53.59
Borehole calliper (in)	2971.80	-505.60
Cement bond index (a/a)	-49.09	-18.86
Gamma ray (gAPI)	-48.43	-0.35
Density (g/cc)	-405.64	143.98
Density correction (g/cc)	-66.58	57.62
Compressional slowness (us/ft)	170.33	-2.92
Shear slowness (us/ft)	133.50	-1.45
Neutron (v/v)	-3.72	-378.82
Log of deep resistivity (ohm m)	-65.35	-2.30
Log of medium resistivity (ohm m)	-65.20	-1.38
Log of shallow resistivity (ohm m)	-65.07	-1.55
Dynamic compressibility (μm/m/bar)	30.92	-30.89
Porosity (v/v)	1.63	-382.76

The residuals for each linear regression model (all based on one input parameter) are plotted as a function of depth in Figure 40. The residuals clearly display correlation at various length scales, and model performance can be improved somewhat if a separate intercept and slope are assigned per depth interval (e.g. gas column, where certain log readings change significantly compared to water bearing intervals, and different formations like separating Upper and Lower Slochteren, and Carboniferous). A downside of such downscaling is a more difficult implementation to compaction models.

The resulting linear regression model from the DTC (compressional slowness) model is compared to the data in Figure 41, showing a linear regression obtained over the full interval and when subdividing the data into four separate depth intervals. The model gives overall a reasonable fit, and the subdivision into smaller depth intervals improves the fit somewhat, especially in the Upper Slochteren (e.g. interval around 3570mAHORt to 3630mAHORT), and captures some of the short-range fluctuations in the deeper end of the data better. Both models, however, still are not able to explain some of the steep gradients in strain rates over short distances, which are consistently over- or under-predicted in certain depth segments.

Nevertheless, a linear model based on the DTC data obtained by wireline can explain a reasonable amount of the strain behaviour. The residuals for the DTC model are plotted against all other variables in Figure 42, and residuals for the DTC model with a different intercept and slope for each zone are plotted in the same way in Figure 43. The impact of having varying parameters for different zones is apparent when comparing the residuals as a function of measured depth between both figures; the longer-range correlation of the residuals is significantly reduced when moving from Figure 42 to Figure 43.

No obvious residual patterns are observed against any other parameter, suggesting that the model cannot be significantly improved by the addition of further linear terms based on additional parameters. We still test the impact of multiple linear parameter models later on, to verify the potential improvements.

The relation between the compressional slowness and the compressibility, Cm, as estimated from the strain when assuming a uniform depletion, found through these linear regression is:

$$C_m = 0.42 * DTC - 24.33$$

Where DTC is the compressional slowness, measured in us/ft, and Cm is given in µm/m/bar. A comparison between Cm values measured on core [12], Cm as estimated from the DSS strain and the Cm as obtained using the above linear conversion from the compressional sonic for Zeerijp-3A are all compared in Figure 44.

The fortunate coincidence of the sonic data appearing to be the best linear proxy for the compressibility is that it is the sonic data that has a field-wide coverage from the sonic model from seismic data. A recommendation for future work on the compaction and subsidence modelling is to look into the possibility of using the field's velocity model maps as a proxy for compressibility, and compare the results to the currently used compressibility maps based on the porosity.
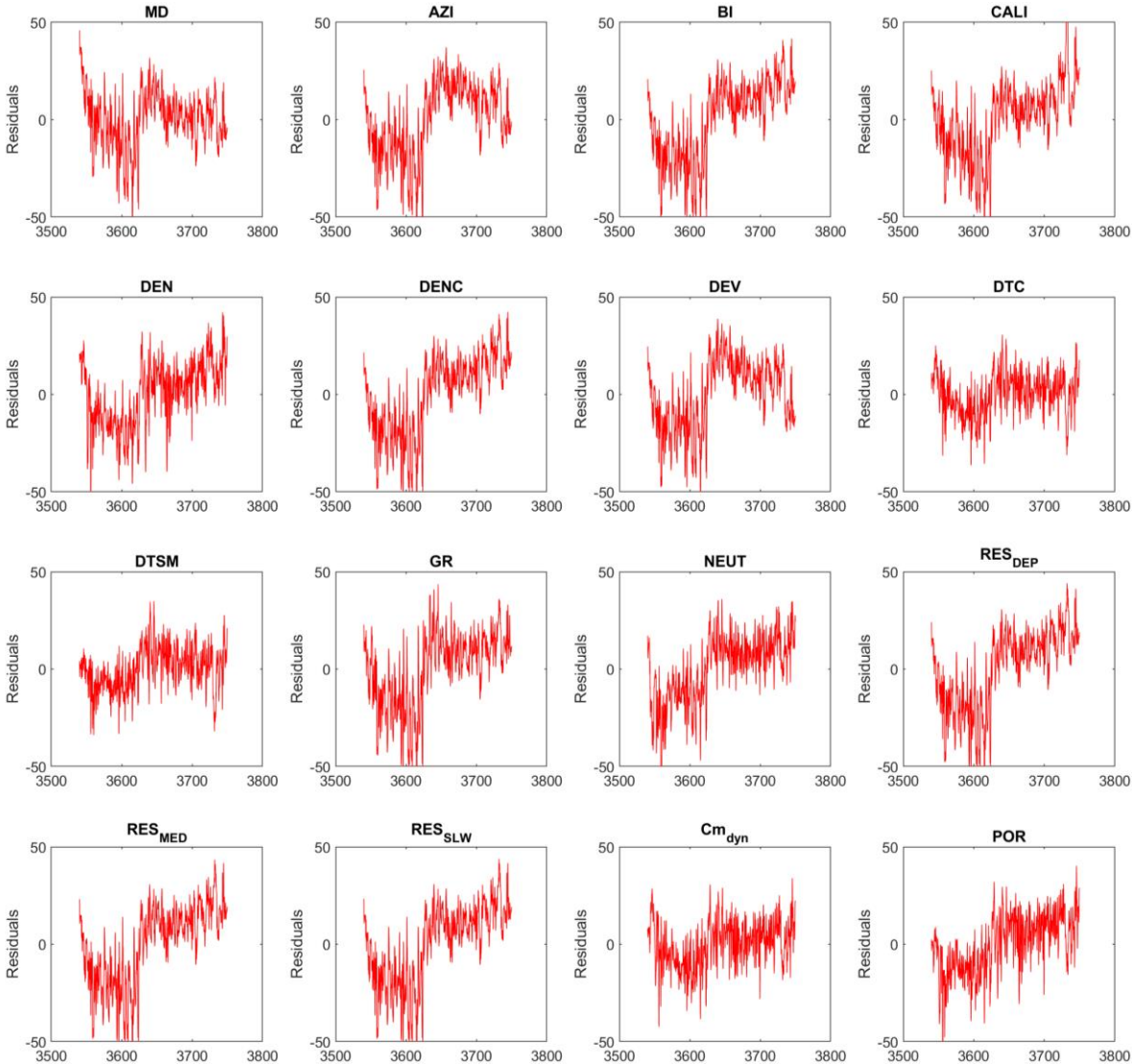

Figure 40: Residuals (in µm/m) for all linear regression models based on different input data (specified in each subplot's title), plotted as a function of depth (in mAHORT).

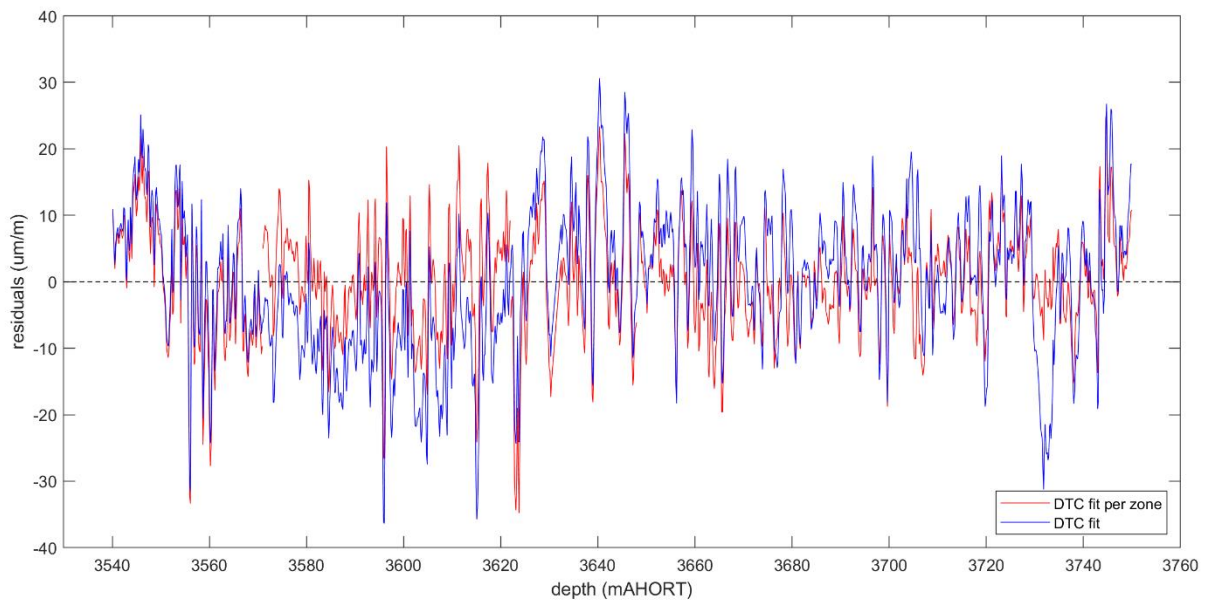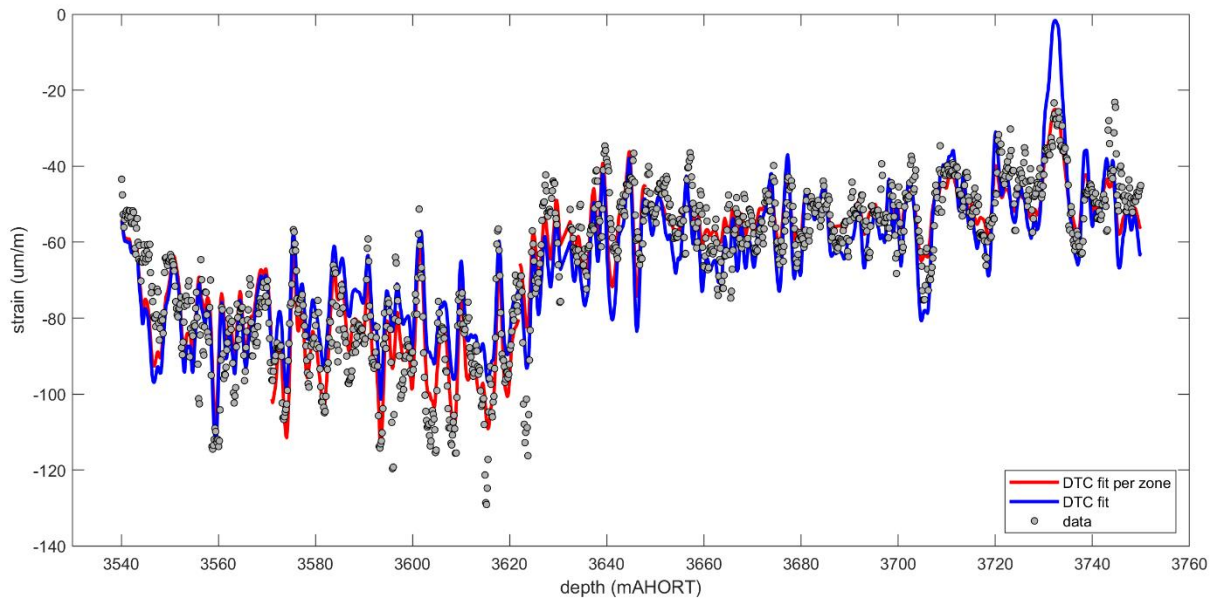*Figure 41: Linear regression model for strain as a function of DTC, when applying one function to the full data (blue), or separate functions for four different depth intervals (red).*
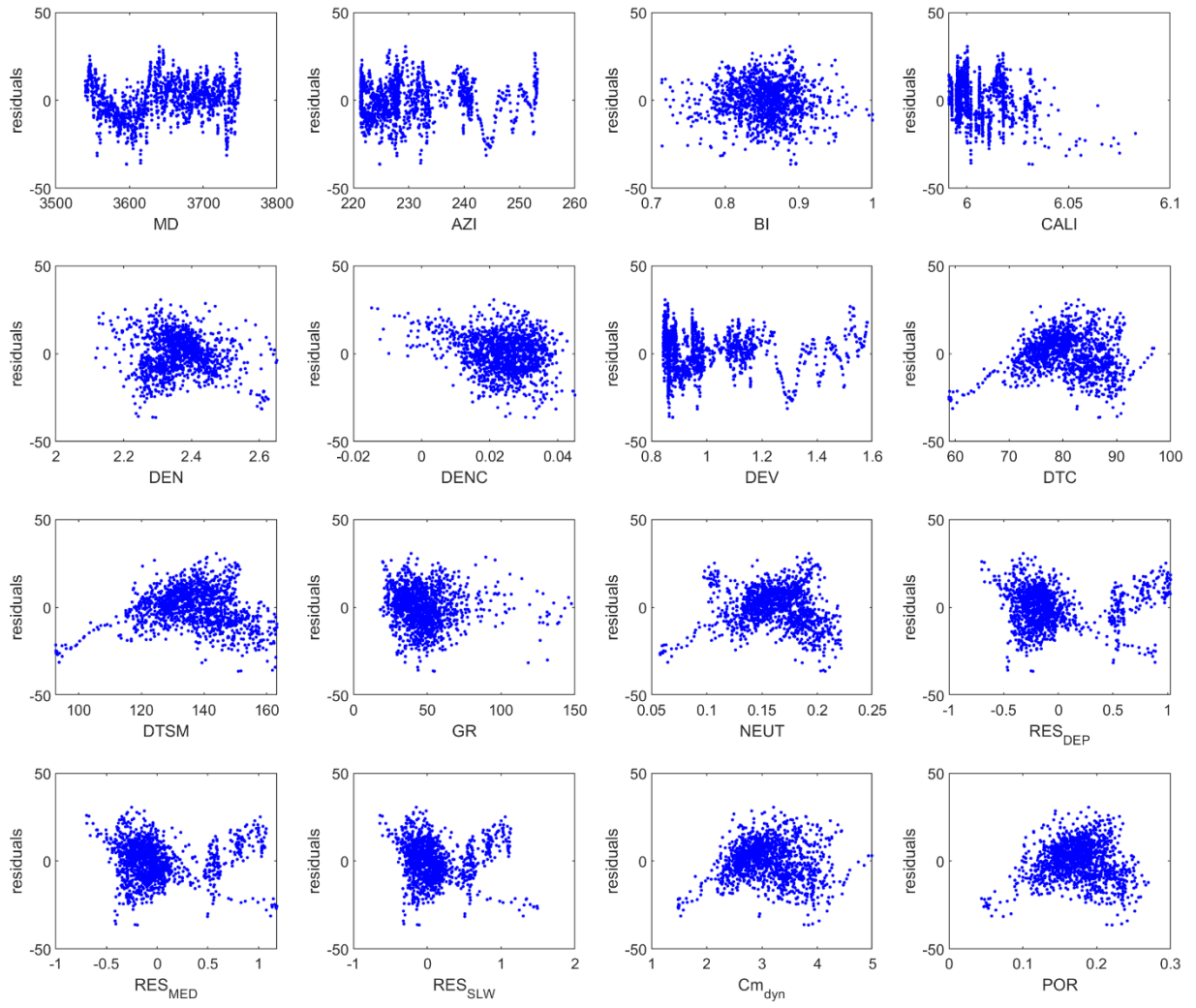
Figure 42: Residuals of the linear DTC model (blue line in Figure 41), plotted against other parameters.

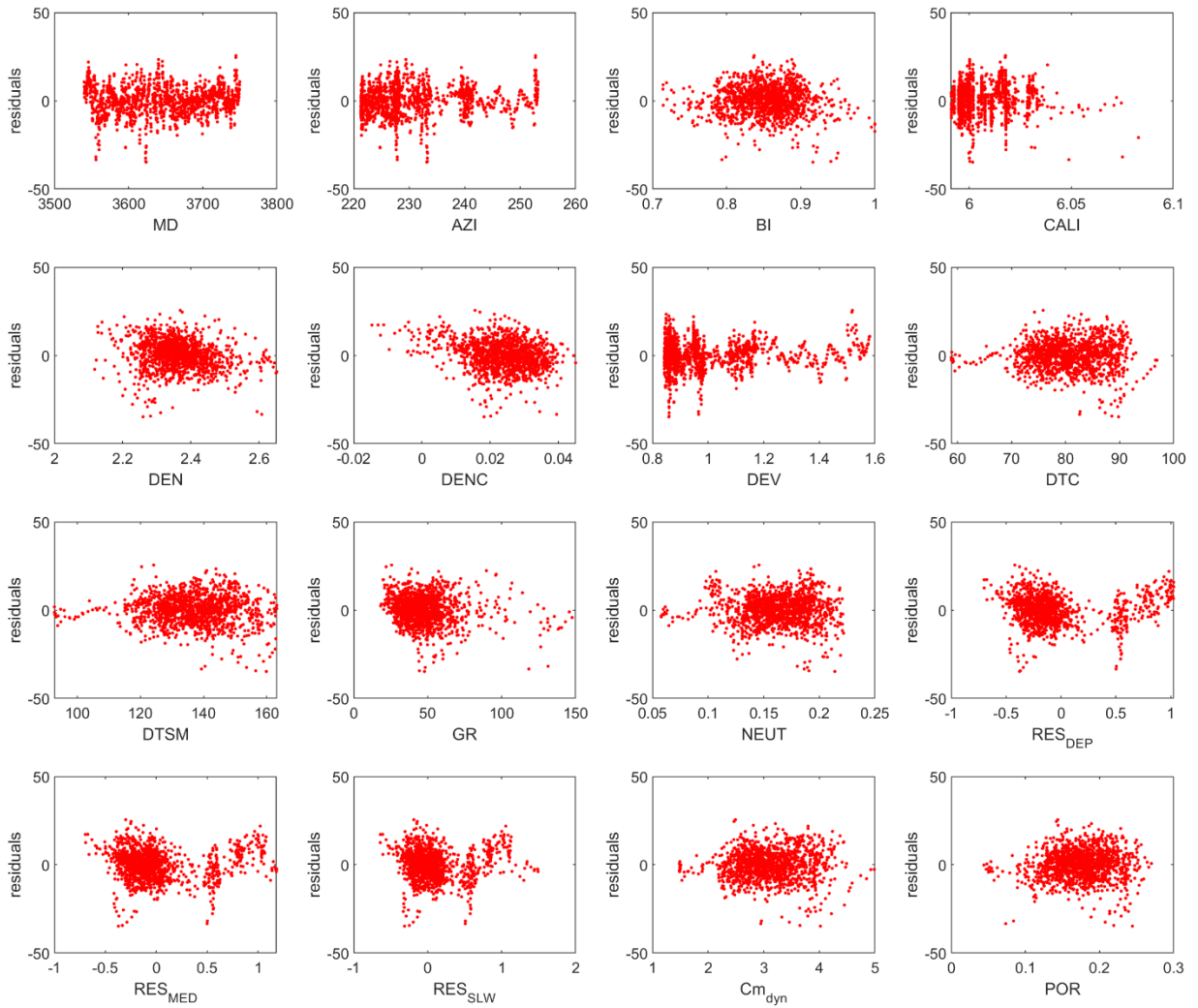*Figure 43: Residuals of the linear zonal DTC model (red line in Figure 41), plotted against other parameters.*
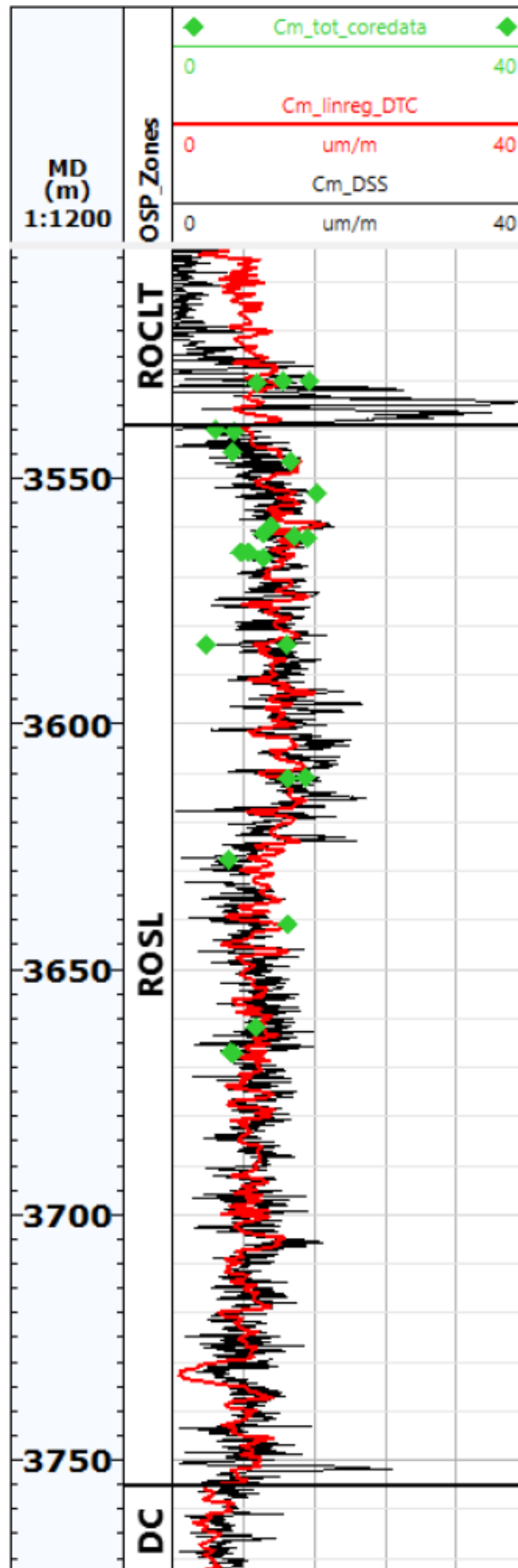
Figure 44: Comparison of Cm values from core data [12] (green markers), Cm values estimated from DSS (black), and derived from the compressional sonic, using the suggested linear regression (red line). Units used for Cm are μm/m/bar for all three data sets.

5.2   Multi-variable model

The combination of multiple parameters can be tested in a similar way as for one parameter by expanding the linear equations by the number of measured parameters, j, as:

$$\begin{bmatrix} y_1 \\ \dots \\ y_n \end{bmatrix} = \begin{bmatrix} 1 & x_{1,1} & \dots & x_{j,1} \\ \dots & \dots & \dots & \dots \\ 1 & x_{1,n} & \dots & x_{j,n} \end{bmatrix} \begin{bmatrix} a \\ b_1 \\ \dots \\ b_n \end{bmatrix}$$

These can be solved for the offset a, and a slope for each tested parameter (b_1 to b_j), for a combination of two, three, or even all 16 available parameters in one go. The improvement is not significant, as expected from the lack of clear correlations of the residuals against other parameters in Figure 42 and Figure 43. The residual standard error (when using 4-year of strain data) is reduced from 10.70μm/m when only using the compressional sonic to 9.84μm/m when using two parameters, down to 9.58μm/m when using a three-variable combination. The best combinations always include either a compressional or shear slowness. Ultimately, the residual standard error can be brought down to 8.49μm/m when using a linear combination of all available parameters (16 in total). See Table 4 for the residual standard errors and R^2 values for the linear combination of all parameters. The resulting match and residuals are shown in Figure 45. Some improvement can be seen, but a short-range correlation of the residuals still remains, where the multi-variable model cannot fully explain the short-range changes in the observed strain.

As this multivariate model only gives a minor improvement to the match, and it being completely impossible (and therefore useless) to implement in any of the modelling, these are not investigated further.
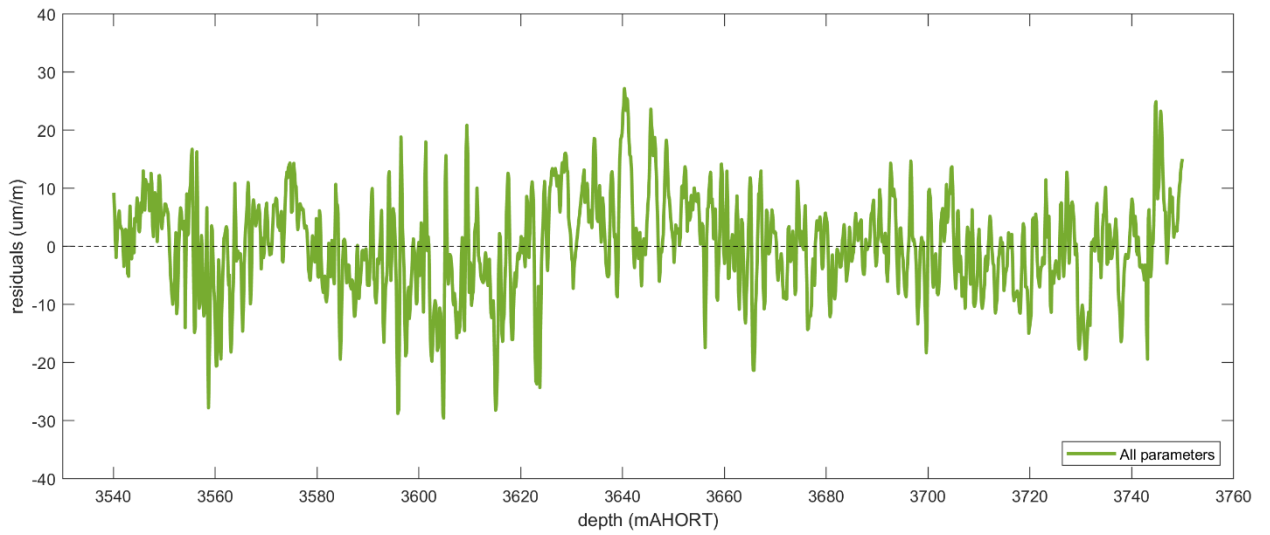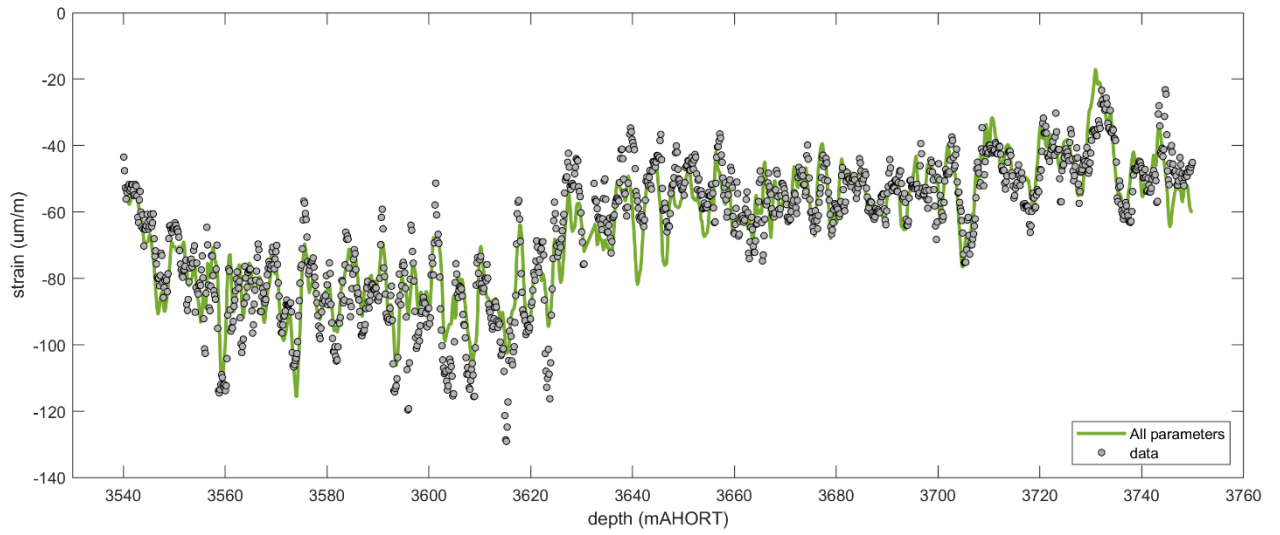
Figure 45: Multi-variable linear regression model for strain, using all the parameters (16 data sources in total).

6 Comparison of in-situ strain and core data

The DSS data in Zeerijp-3A allows for a unique comparison of the strain measured on core plugs with the strain measured in the well at the same locations of these core samples, where both measurements are also performed on very similar length scales (both on a few centimetres).

The core data used for the comparison here are described in detail in [12]. The data from these cores is also released and available at [12].

Instead of looking at the deformation over similar depletion levels, we here focus on the derived uniaxial compressibility, C_m. The C_m is accurately derived for the core data thanks to the well-known and well controlled measurement environment. The environment of the in-well data is less well known, as the pore pressures (and principal stresses) are not directly measured in the well itself. The strain as measured by the DSS system is converted to a compressibility by assuming uniform depletion during the monitoring phase, as predicted at the well's location by the dynamic reservoir model. The predicted depletion rate is about 2.5bar/year. For an 18month period (first year and a half of monitoring), this would be 4bar depletion, and 8bar for 41months (full monitoring period during the write up of this report).

The resulting estimated C_m values from the DSS are plotted together with those derived from the core plugs (obtained from the same well, so both methods looking at the same material) in Figure 46, for the strain accumulated over the first 18months of the DSS monitoring. The C_m values are plotted against porosity; an often-used proxy for the compressibility. The core data is plotted for both the core-derived porosity (at start of measurement, at in-situ stress conditions) and wireline derived porosity (at the depth where the core plug was taken), to not obscure the data clouds too much by the uncertainty (and differences in porosity from using different methods).

Very good agreement in the range of C_m values is observed (agreement in the range of porosity values reaffirms that core samples were taken to represent the range of different porosity values occurring in the reservoir). The range of C_m values from the DSS data is narrowed when using the data over the full monitoring period (Figure 47). At least part of the reduction is due to increased signal to noise of the system (higher strain signal accumulated over the increased monitoring time), but differences between the two figures can also arise from non-linear effects and non-uniform depletion that are not considered in estimating the C_m value from the in-well measured strain.

The reservoir compressibility is for most fields derived from surface subsidence data (through inversion), due to the lack of (core) compaction data. Reservoir compressibility derived through inversion does not always agree with the compressibility measured on core. Differences can originate from assumptions made in the inversion (e.g. conversion of compaction to surface subsidence, upscaling of reservoir properties), or from non-representative core experiments (e.g. differences in applied stress path, experimental setup, selection of representative samples, core damage). Here, we see good agreement between in-situ compaction data and compaction data from the laboratory, making it likely that both data sets do represent the actual reservoir behaviour in terms of compaction, and affirming that the experimental standards followed for the core experiments in [12] do provide reliable compaction data.

The static to dynamic conversion estimates made in Section 3.2 used the strain data from the fibre optics measurements in combination with an assumed pressure depletion to derive the static compressibility. The agreement between the static values inferred from the in-well strain and the (static) core compressibility values further demonstrates the validity of the conversion factors derived in Section 3.2.
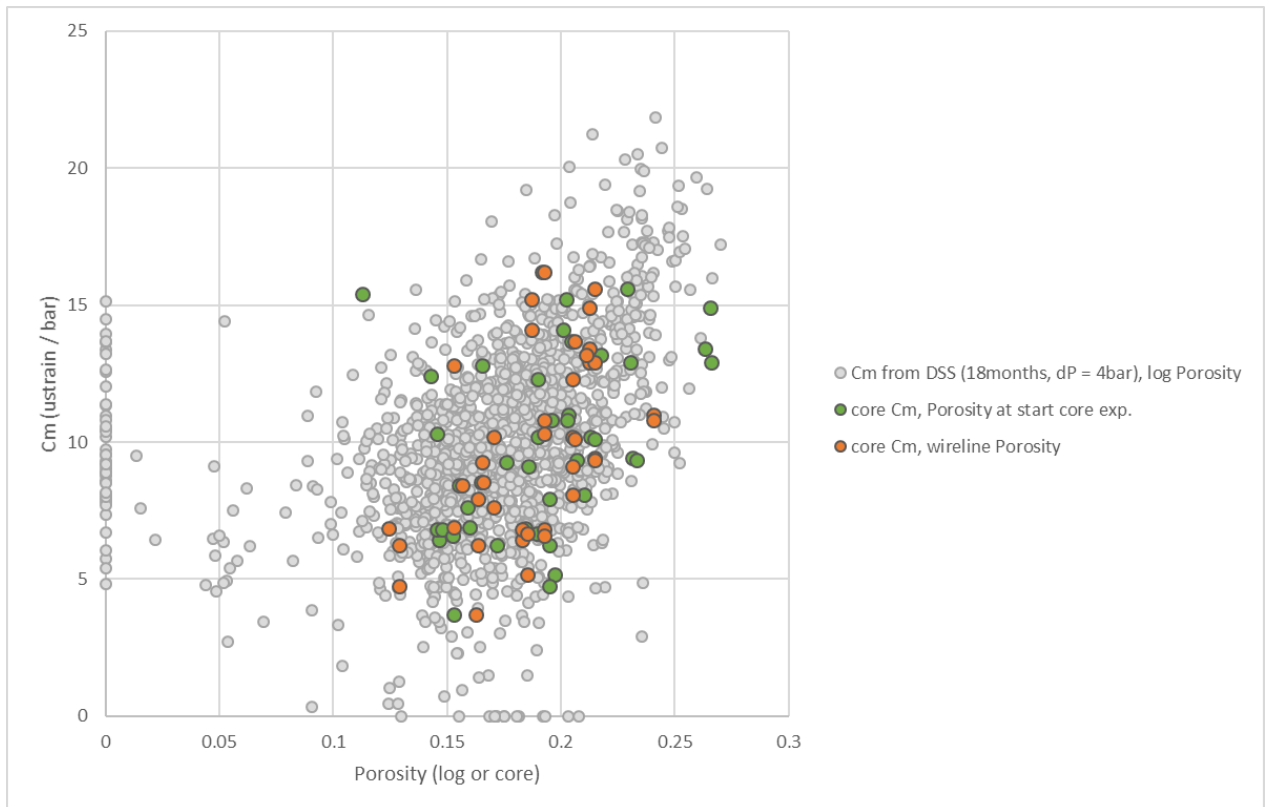
Figure 46: Comparing Cm values as estimated from the strain with those measured on core samples from the Zeerijp-3A well. The Cm values from DSS are derived from the strain, as measured by DSS over an 18 months period (March 2016 to November 2017), assuming a depletion of 4bar during that period (depletion rate of 2.5bar/year). The DSS derived Cm values are plotted against porosity derived form wireline logs in Zeerijp-3A. The core measurements are from [12]. To show the scatter in data due to differences in porosity, the core data have been plotted against core measurements of porosity; mercury at in-situ (start of experiments), and the wireline porosity at the depth of each plug in Zeerijp-3A.

Figure 47: Same as figure above, but now after acquiring strain data in Zeerijp-3A over a 41-month period.
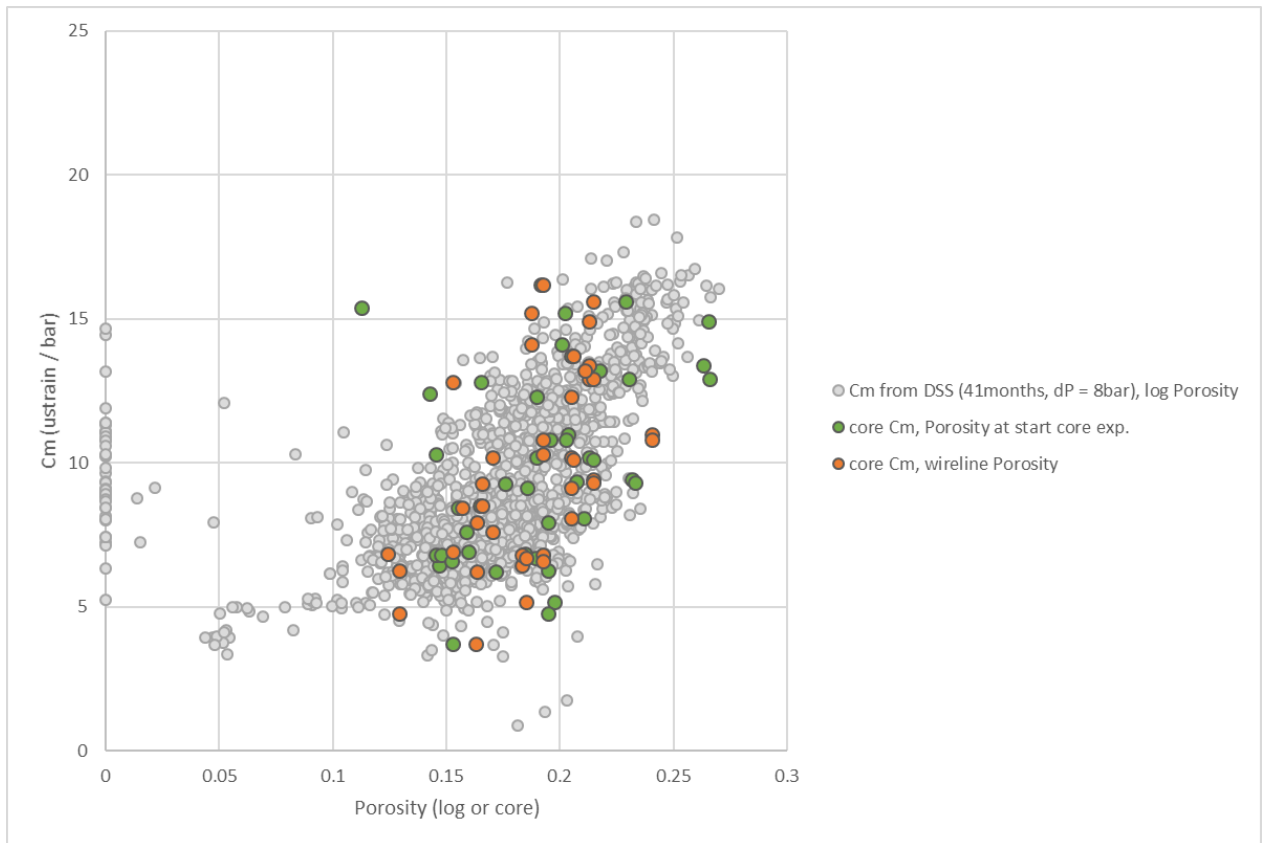
7 Correlation of strain with geophone data

The main objective of the Zeerijp-3A well was the installation of downhole geophones. These geophones were part of a wider downhole seismic monitoring project, where geophones were placed in five dedicated wells. The purpose of the monitoring was to gain a better assessment of the earthquake depths and magnitudes, and to help gain a better understanding of the geomechanical behaviour of the field during production. To further aid the understanding of the mechanical behaviour of the reservoir, the opportunity was taken to install the DSS fibres in one of these new geophone wells.

A schematic layout of the geophone installation into the Zeerijp wells is shown in Figure 48. The DSS system in Zeerijp-3 covers the same intervals over which the geophones have been installed. The distance between the individual geophones in the string ranges between 15-40m. Further details of the geophone survey design and findings can be found in [13].
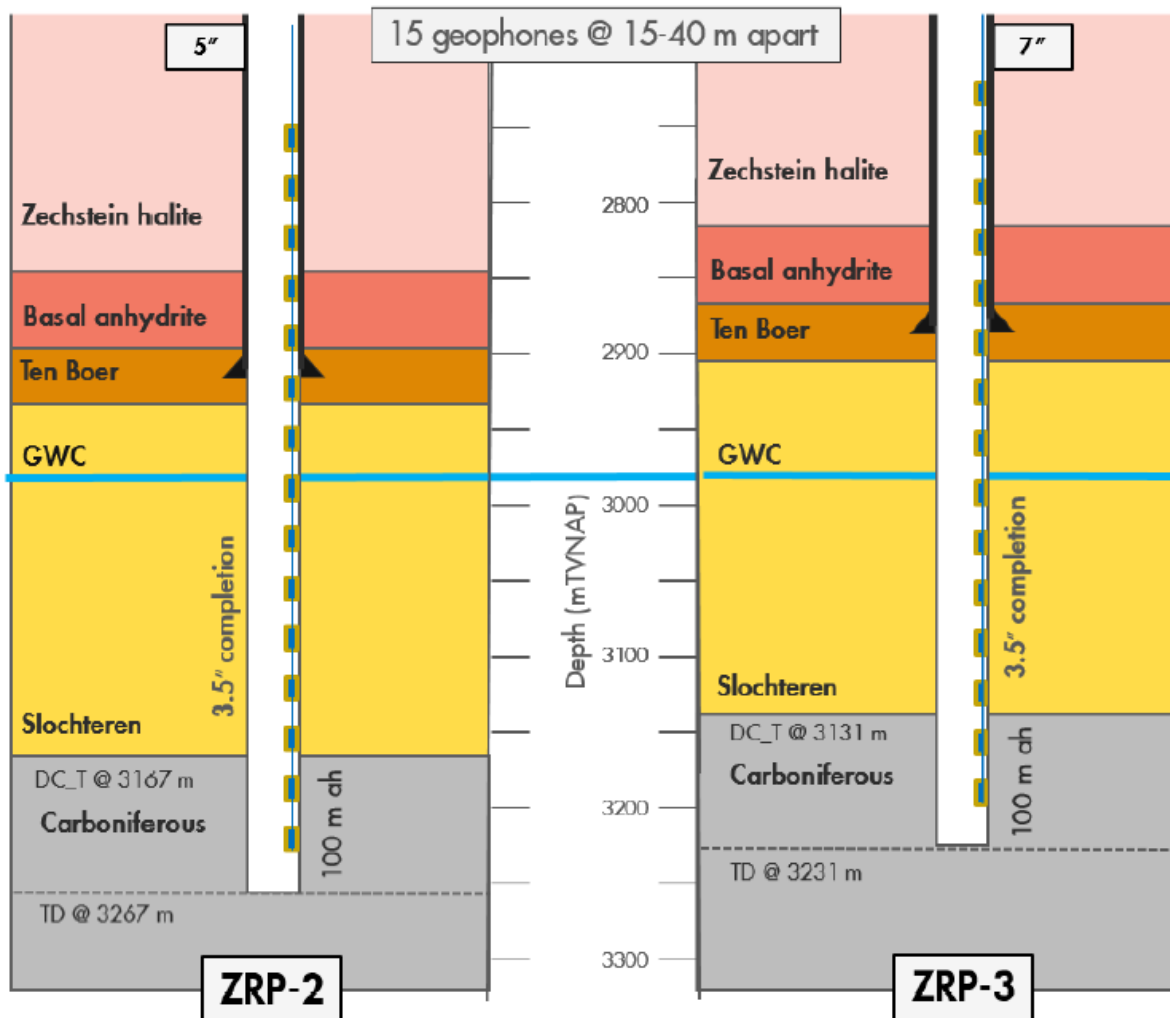

Figure 48: Schemetic layout of the geophone installation in Zeerijp-2 and Zeerijp-3 wells, taken from [13].
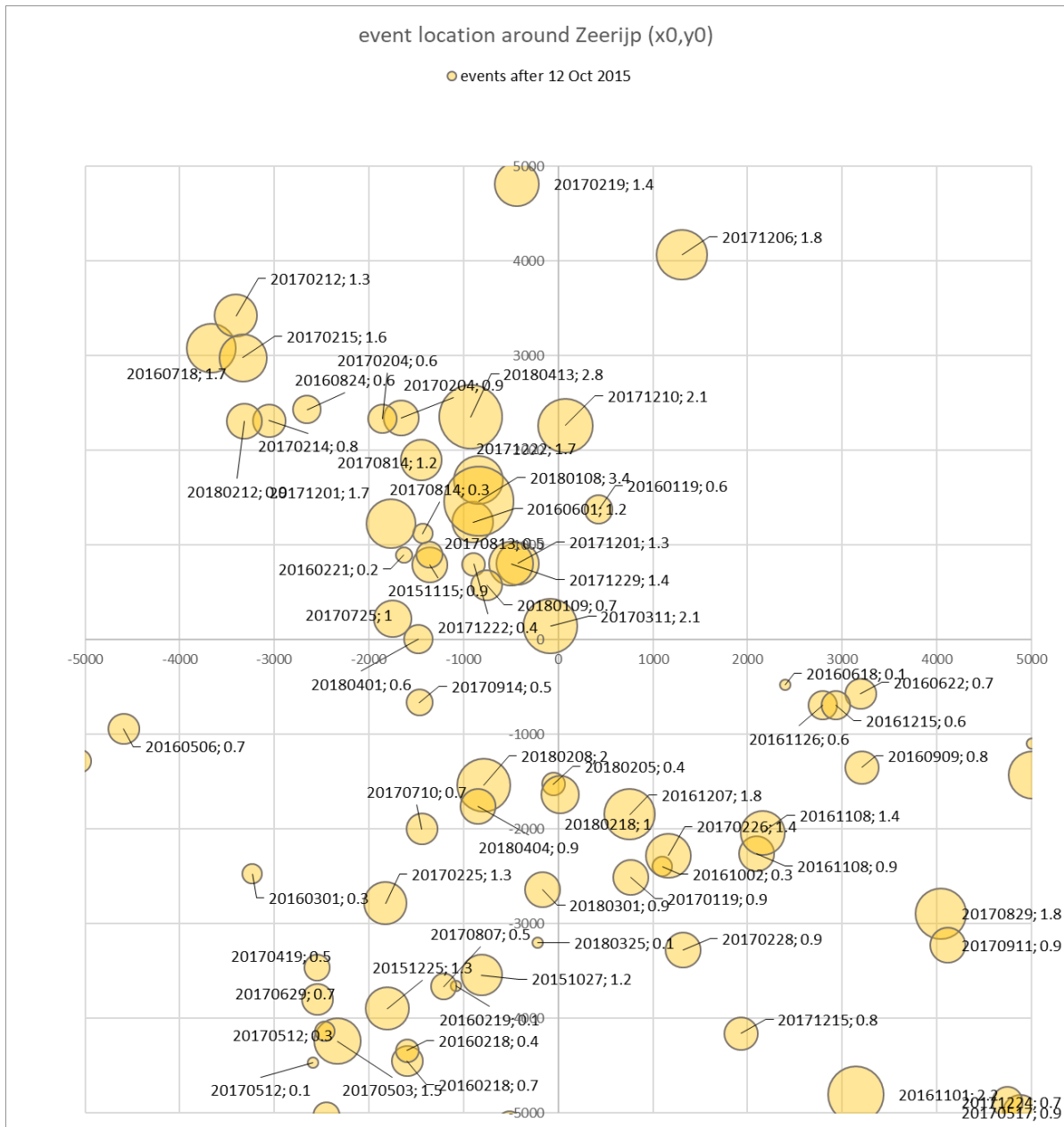
Figure 49: Locations of earthquakes detected by geophones, relative to the Zeerijp-3A well (which sits in the origin of the plot). The size represents the magnitude of the earthquake. Labels indicate the date of the event and magnidue. Only events that were recorded after the start of DSS monitoring are shown in the plot.

Besides the in-well strain data, Zeerijp-3A has provided a catalogue of hundreds of seismic events, ranging in magnitude from M-3.2 to M3.4. The events recorded by the geophones are plotted relative to the Zeerijp-3A well in Figure 49. Events that were recorded after the start of the DSS monitoring are shown. Their size represents the relative magnitude. As all these data were obtained in the same well, we use them to examine a relationship between compaction and seismicity. Similar studies have been done for earthquake generation in the mining industry [14], water injection fields [15], and gas extraction for full field scale [16]. The correlation between seismicity and compaction in [16] was based on a full field seismic catalogue measured by a network of surface stations and reservoir compaction inferred from surface subsidence over the entire Groningen field. In contrast, the available data in the present study provide a direct, local comparison of the downhole geophone recordings with high resolution in-well strain, with the aim to determine any relationship with the

cumulative slip on faults surrounding he wellbore and the total measured strain within the same volume of rock.

In order to compare the released seismic energy and the accumulated strain, we convert the magnitude of the recorded seismic events and the measured strain over the same time period to the seismic moment. For the recorded seismicity, this is done by the following equation:

$$M_{seis} = \sum_i 10^{a\,M_{w,i}+b}$$

The summing over magnitudes M_w of all events, i, recorded by the geophones. The parameters a = 1.5 and b = 9.1 are used [17].

The volume change is related to the moment related to compaction as:

$$M_{comp} = G\Delta V$$

The bulk modulus, G, here is derived from wireline logs from the Zeerijp well itself[2]. In order to convert the 1D strain to moment, it first needs to be converted to a volume. For the comparison here, we convert the strain to moment of compaction over a wide range of radii. The moment of released seismicity is then determined for all the events that occurred within the same radius. The situation is sketched in Figure 50.
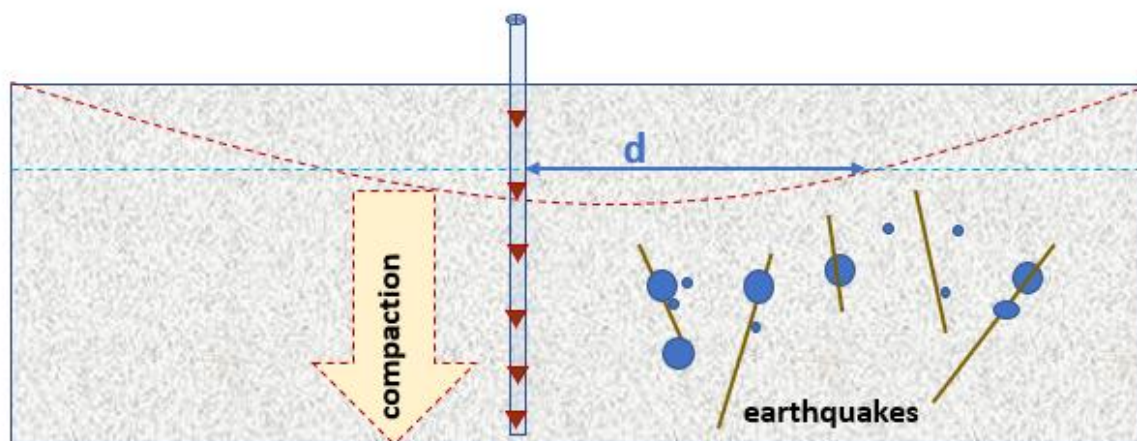

Figure 50: Schematic of the situation around the Zeerijp-3A well. The measured strain is converted to moment of compaction for a range of radii, d. The moment of released seismicity is based on all the events recorded by the geophones in the Zeerijp-3A well within the same radius, d.

An assumption had to be made for the volume over which uniform compaction measured by the DSS cable can be compared with the seismic moment is released. The volume assumption implies that all compaction occurring within the assumed radius is responsible for all the seismic moment released within the same radius. This is obviously an idealized, or "end-member" case. Other volume assumptions will have similar drawbacks, but what we are after is a simplistic, first-order-of-magnitude comparison of localized compaction with released seismic moment, and therefore we proceed with these assumptions as a first pass.

The comparison of compaction and seismic moments is plotted in Figure 51. The moment of compaction has been made for separate parts of the reservoir, and it becomes apparent here that,

---

[2] We use here the dynamic value and did not convert to static modulus as the order of magnitudes are important in the comparisons here, and a factor of 2-3 has no impact on the conclusions.

because of the range of values, the exact amount is not too important given the proximity of the moments of the reservoir only (Mcomp ROSL) and that of the full cable (Mcomp full cable). Making a conversion from dynamic to static moduli will have a similarly negligible effect on the figure.

The results show that, independent of the assumed radius of uniform compaction (we test the range of radii from a few hundred metres around the wellbore to covering the full Groningen field), the moment from compaction is always several orders of magnitude higher than the moment of released seismicity.
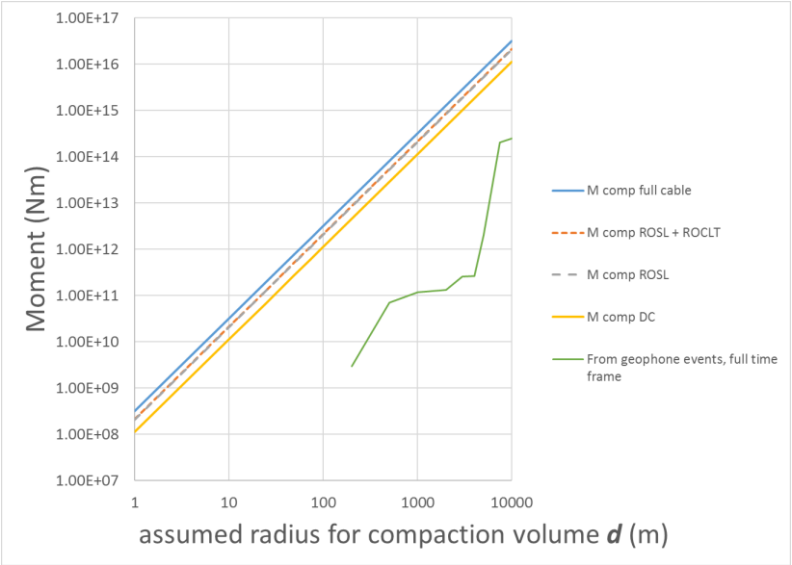

Figure 51: Moment from compaction, for a range of assumed radii, and released (measured) seismic moment.

While geophones can detect events of a magnitude as low as M=-3, they do have a distance-sensitivity threshold where the smallest detectable magnitude increases with distance (see Figure 52). That means that only larger events are recorded with increasing distance from the observation well implying that the moment of released seismicity for larger radii in Figure 51 are mainly composed of fewer, higher magnitude events.

To visualise the potential impact of areal sensitivity of the geophones, we made a similar comparison in Figure 53 but included also the moment of seismicity using the catalogue of the surface network. While the surface network is not able to reliably detect magnitudes of M<0, it does not exhibit a distance magnitude bias like the geophone string as its sensitivity is more or less equal across the Groningen field. The results are very comparable to those for the geophone network. The similarity of the two data sets imply that the sum of the released seismic moment is heavily dominated by larger events, and only a negligible amount is released by small events.
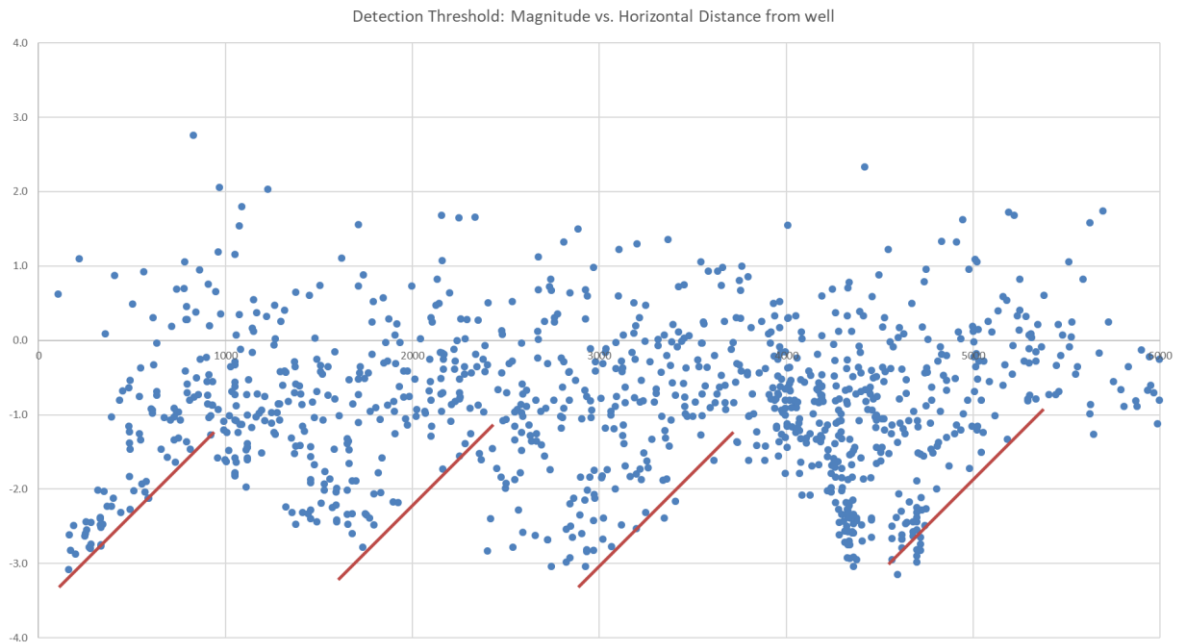
Figure 52: Detected earthquake magnitudes from the entire geophone network, plotted against the distance from the Zeerijp-3A well. The red line indicates the detection threshold. The presence of additinoal downhole geophones makes it possible to detect lower magnitude events further away from Zeerijp. A detection threshold is plotted for each of the geophone systems in red.

The results in Figure 53 show that the sensitivity mainly to the low magnitude events has negligible effect on the outcome: it is mainly the higher magnitude events that contribute to the figure, due to the logarithmic scale. The different time periods of recordings also do not seem to suggest vastly different patterns, and the moment from compaction is still always larger than the moment of released seismicity.

A future refinement of the comparison is a division of the data per depth. Both the strain and earth quake event data are recorded over a large depth interval, and the geophones can localise the events at a depth accuracy of a few tens of metres. The refinement in depth could reveal differences in the relation between compaction and released seismicity for different zones in the reservoir, and a link to properties such as porosity could also be made. This is, however, still work in progress.
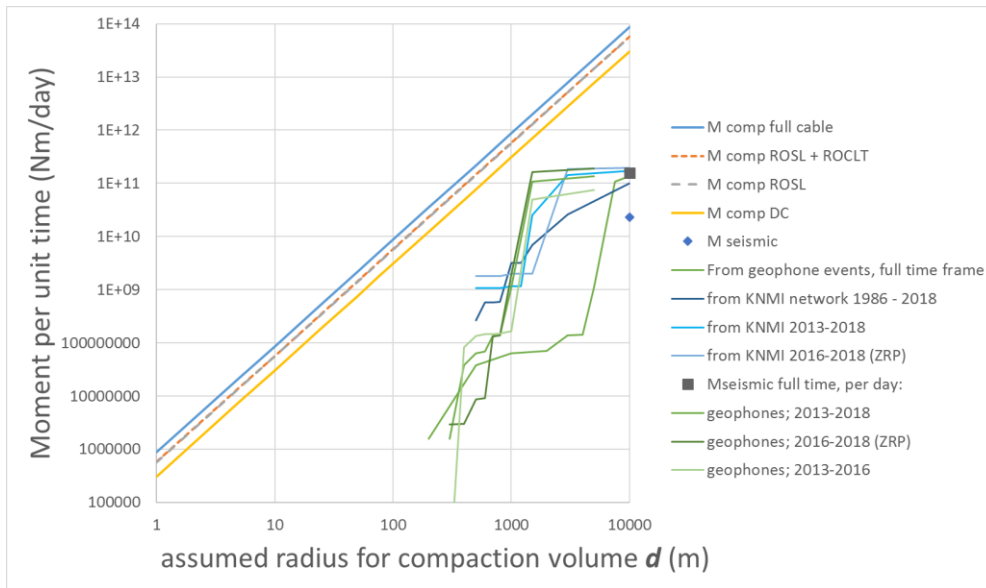
Figure 53: Moment of compaction as in Figure 51, and released seismic moment for different time preiods and using different measurement catalogues. All moments have now been normalised by observation time, to make fair comparison for datasets that span different time periods.

8   Summary and outlook

Observations and conclusions:

General observations in the measured strain:

- Average strain accumulated during the last four years of monitoring is around 100microstrain over the Upper Slochteren and 80microstrain over the Lower Slochteren.
- The Carboniferous is seen to compact, especially the intervals close to the Slochteren, to an average of around 30microstrain over the last four years. It is therefore likely that the Carboniferous is depleting.
- Part of the Ten Boer was seen to rapidly compact, shortly after completing the well. The rate of compaction has slowed down, and the area of compaction has spread out a little further throughout the Ten Boer. Average strain of the whole Ten Boer is 10microstrain over the last four years, while it is more than 200microstrain over the small interval that shows more compaction.
- The top of the Zechstein shows alternating areas of early compression and expansion. The total signal of the Zechstein, and especially the base of the Zechstein, starts to show compressive signals above the background noise.

Insights derived from Zeerijp fibre optics data:

- No permanent deformation was observed that can be associated with the M3.4 earthquake that occurred near Zeerijp on 8 January 2018.
- Comparison of the dynamic (log derived) and static (estimated from strain data) compressibility values for the Zeerijp well suggest a conversion factor of 3 between static and dynamic moduli.
- Data during CTCO operations suggest a thermal correction factor to the strain of about 5-8microstrain per $^{\circ}$C change in temperature. This is in line with previous findings in steam injection wells.
- The thermal disturbance from the CTCO operation on the strain data lasted only a few hours, indicating that well interventions such as wireline operations will have a negligible temporal effect on the measured strain.
- The temperatures recorded by the DTS system around the reservoir level show a standard deviation of 0.4 $^{\circ}$C. When using temperature correction on the strain data, the measurement noise of the DTS will add a correction noise to the strain of around 2 to 3 microstrain.
- The temperature uncertainty from DTS is much lower than from wireline logs. The latter can show significant differences between wireline passes, and more over the thermal gradient seems to be dominated by the well(fluids) rather than the thermal gradient of the formation.
- The noise levels on the measured strain are around 6microstrain for the beta-unit DSS interrogator, and have improved to 2microstrain in the production unit DSS interrogator.

Frequency analysis:

- Thermal fluctuations from the atmosphere penetrate down to only the first 10-15m, and do not affect the measurements at the reservoir level.
- No spatial frequencies are observed on the DTS data other than during geophone operations, where the temperature can locally increase by >3 $^{\circ}$C due to the heat radiated by the geophones.
- Spatial frequencies are observed on the strain signal during CTCO, but disappear rapidly after the operations. These suggest that there is better thermal coupling between the well and the

DSS cable at the locations of the clamps, but in thermally stable periods the strain measurement is not affected by the clamps or casing.

- No temporal frequencies are observed on the strain data, suggesting seasonal fluctuations (from production or tidal influences) are not present (at least not with an amplitude >1micro-strain).

Correlation of strain with well data:

- Strong correlation observed between the strain and several well logs, like the density, sonic velocity (both shear and compressional) and log-derived properties like porosity and dynamic compressibility.
- No obvious correlation found between the strain and well-related properties such as well inclination, well azimuth, or cement bond index.
- The strong correlation between rock properties and the strain, and a lack of correlation with well properties, provides strong evidence that the strain signals are related to the formation.
- Statistically the best correlation is observed between the strain and sonic slowness, which is marginally better than the correlation with density or porosity. Following from this, it is suggested to investigate the possibility of using the velocity model as a proxy for the compressibility instead of the reservoir porosity maps. Besides the slightly higher correlation with the strain, the velocity maps have the additional benefit of being closer to the raw data and less affected by interpretation steps.

Comparison of in-situ strain with core data:

- Using assumptions about the depletion allows for the strain to be converted to compressibility values along the well, which compare very well to the compressibility values measured in the laboratory on core plugs from the same well.

Correlation of strain with geophone data:

- Early comparisons of the moment from compaction (derived from Zeerijp DSS data) and moment of released seismicity (derived from Zeerijp geophones) show that the moment from compaction is always (over the monitored interval) more than an order of magnitude higher than the moment of released seismicity.
- Further work can focus on a subdivision of the comparison, for sub-reservoir zones or porosity classes.

References

[1] Matt Cannon and Pepijn Kole, The First Year of Distributed Strain Sensing (DSS) Monitoring in the Groningen Gas Field, SR.17.00934 (2017)

[2] L.L. Vos, Groningen Field RFT and FIT Data & Information on Limburg Connectivity, L.L. Vos, NAM200301000527 (2003)

[3] Pepijn Kole, Estimation of ranges for Cm in the Carboniferous, EP201809201820 (2018)

[4] Onno van der Wal, Usage of acoustic logs for Static Cm Calculation, NAM200401103360

[5] Internal Shell communications of unpublished laboratory results

[6] Mark Haugland, et. al., Subsurface Distributed Strain Sensing in the Belridge Field Diatomite Reservoir, SR.16.10124 (2016)

[7] Grattan and Meggitt, "Optical Fiber Sensor Technology: Advanced Applications – Bragg Gratings and Distributed Sensors", Kluwer Academic Publishers, The Netherlands, 2000, p. 115.

[8] Wenyuan Wang, et. al., "Measurements of thermo-optic coefficient of standard single mode fiber in large temperature range", Proceedings Volume 9620, 2015 International Conference on Optical Instruments and Technology: Optical Sensors and Applications; 96200Y (2015); doi: 10.1117/12.2193091

[9] Tao Wang, et. al., "Temperature and strain characterization of regenerated gratings", arXiv, 2012

[10] K. Langaas, et. al., Tidal Pressure Response and Surveillance of Water Encroachment, SPE 95763 (2005)

[11] Eric Chang and Abbas Firoozabadi, Gravitational Potential Variations of the Sun and Moon for Estimation of Reservoir Compressibility, SPE 67952 (2000)

[12] Sander Hol, et.al., Rock Physical Controls on Production-induced Compaction in the Groningen Field, Scientific Reports 8 (2018)

[13] Monitoring Local Seismicity with Deep Downhole Arrays, NAM report (2019)

[14] A. McGarr, Dependence of Magnitude Statistics on Strain Rate, Bulletin of the seismological society of America, 66, 1, 33-44 (1976)

[15] A. McGarr, Seismic Moments and Volume Changes, Journal of Geophysical Research, 81, 8, 1487-1494 (1976)

[16] S. J. Bourne, S. J. Oates, J. van Elk, and D. Doornhof, A seismological model for earthquakes induced by fluid extraction from a subsurface reservoir, J. Geophys. Res. Solid Earth, 119, 8991–9015 (2014)

[17] T. C. Hanks, and H. Kanamori, A Moment Magnitude Scale, Journal of Geophys. Research, 84: 2348-2350 (1979)